Mathematical Modelling of Mechanical Alloying

by John R. Harris, BSc.

Thesis submitted to The University of Nottingham for the degree of Doctor of Philosophy, September 2002

Abstract

This thesis applies Smoluchowski's coagulation-fragmentation equations to model the mechanical alloying process. Mechanisms operating during the milling process are reviewed. In the first instance, models are developed that predict the size distribution of a single milled powder while ignoring mixing phenomena. A methodology is developed that allows experimentally measured sieve-fractions to be converted into volumetric cluster size distributions. Model parameters describing the rate of aggregation and fragmentation are obtained by fitting the model's predicted average particle size data over time to that measured in experiments. Different size-dependent aggregation and fragmentation rates are tested in many milling scenarios and the most realistic size-dependence of rates is found.

In the second part of the thesis, the best size-dependent rates are generalised and used with a two-component version of Smoluchowski's system of equations. This model also includes binary mixing phenomena by considering clusters that have two types of component. The two-component models are applied to experimental situations using the methods developed for one-component models. Comparing these multi-component models to experimental measurements verifies the modelling method and gives reasonable agreement. An improved fragmentation rate is suggested to enhance the model's accuracy in the prediction of mixing rates.

Acknowledgements

I would like to thank my supervisor, Dr. Jonathan Wattis for his continued assistance, guidance and patience throughout my studies. I am also grateful for the advice of Prof. Graham McCartney and Prof. John Wood on the theory and practicalities of mechanical alloying, and for the funding provided by EPSRC.

My friends and colleagues in the Department of Theoretical Mechanics have provided much appreciated encouragement. Those in materials science have provided invaluable help with my experimental studies.

Finally, I would like to thank my family for their support, and Eleanor who has provided the most encouragement of all.

Contents

List of Figures

List of Tables

Chapter 1

Introduction

Alloy design is an ancient art. As early as 800 AD the Japanese were processing metals to hone the performance of their swords. Their meticulous attention to detail produced cutting blades that are widely regarded as the finest ever made. Today, with the advent of mass production and new applications for alloys, the importance of alloy design remains. Alloys are still an active area of research.

The sword makers of 800 AD sought favourable mechanical properties in their materials producing a strong, sharp blade. However, alloying can also affect the chemical, electrical, magnetic and thermal properties of material. Modern alloys are designed to provide a combination of different properties, balancing cost against performance. Turbine blades in power generators need to be strong, light weight and able to function at high temperatures without chemical decomposition. These properties make the generator more efficient, giving more power at lower cost and environmental expense.

Continued development in the alloy industry is driven by sensitive applications of this type, where an improvement in alloy performance provides a high financial saving. The expense of developing new materials is outweighed by the potential savings associated with success. To sustain development ad-

vances must be made on two fronts. Theoretical advances suggest methods for manufacturing new or better optimised materials, while advances in processing technology make more theoretical production techniques realisable.

In the past the industry has been limited by the technology at hand. The Japanese used simple furnaces, oil quenching and deformation techniques to process their steel. Production was very slow, and only a small amount of material was processed at one time. Modern processing relies on the same principles as these ancient techniques, using thermal and deformation processes. However, we have more powerful methods of heating, cooling and deforming material, and finer control. This modern technology allows us to produce comparatively exotic materials on a large scale.

Technology advance is complemented by a deeper understanding of the alloying process. While the Japanese knew that they could alter the properties of a material using heat treatments, we now know that these treatments adjust the structure of the alloy, changing the crystallinity and the intimacy with which the constituent chemicals are mixed. Quantitative theories allow prediction of the properties resulting from a particular treatment. This gives a high degree of control over the alloy product and speeds the design process. The theories also highlight absolute or practical limits of a particular processing technology, where a desired microstructure cannot be achieved.

The need to overcome these limitations has driven innovation towards new processing techniques including equal channel angular extrusion (ECAE), rapid solidification and various powder metallurgy processes. Arguably the most successful of these new techniques is Mechanical Alloying (MA), heralded as the "Alladin's lamp of powder metallurgy" by T. H. Courtney *et al.* [22]. Mechanically alloyed materials are already used for high return application in the defence and power industries and several types of apparatus have been developed to treat powder. Our technology is certainly capable of man-

ufacturing mechanical alloys and commercial interest has motivated studies into MA of many different alloy systems. However, the cost of developing MA materials remains high and prohibits their use in mainstream applications.

Current MA research hopes to lower these development costs through a better understanding of the process. At present the development cycle involves a series of experimental trials. The product is gradually refined, first in the laboratory and then at a production scale. A better understanding of the processing received by the powder would accelerate development and lower costs. The ultimate goal is to control this new process as accurately as the conventional techniques are controlled, allowing confident optimisation of alloy properties and economical production of materials on a large scale.

The majority of commercially funded MA research has concentrated on the production of a particular product. Several complex alloy systems have been studied, and many new phenomena have been observed. These studies have shown mechanical alloying to be a complex process. Many of the empirically developed theories of material behaviour in current use cannot be extrapolated to describe MA material. As a consequence, most current models describe just some of the changes that are achievable through MA. Examples include models that concentrate on chemical diffusion within powder particles [64] or microstructural changes and work hardening of the material [48]. Similarly, the models presented in the later chapters of this thesis examine just the size distribution and mixing characteristics of the milled powders, ignoring changes in microstructure and chemistry. Note, however, that the parameters in these models are determined empirically so they will, in some way, account for microstructural and chemical differences between different milling scenarios.

This introductory chapter looks at all aspects of mechanical alloying. The next section gives an overview of mechanical alloying, discussing relevant ma-

chinery and the changes observed within powder particles. Experiments and models concerned with the machinery and changes in powder properties during Mechanical Alloying are reviewed. Then, §1.2 introduces Smoluchowski's model, on which our models are based, and discusses the results of some useful studies conducted on the system.

The later chapters of this thesis are arranged in two parts. Part I deals with milling of just one metallic powder: Chapter 2 looks at the modelling theory, Chapter 3 describes a simple milling experiment conducted to verify the models, Chapter 4 details how the experimental data and models can be used together, giving results of the study, and Chapter 5 repeats this analysis with a wide range of experimental data obtained from the literature. Part II looks at how binary systems mix in the mill. Chapter 6 generalises the models from Chapter 2, and Chapter 7 applies these models to data taken from literature.

1.1 Introducing mechanical alloying

Mechanical alloying is a fundamentally different approach to alloy-manufacture because it relies on deformation processes to mix material. In contrast, traditional techniques use heat treatments and chemical reactions to combine alloy components. The properties of conventional alloys may be adjusted by applying deformation processes but the degree of deformation attainable is lower than that achieved through MA.

The extreme deformation experienced by milled material is an intrinsic part of the MA process. Treated powders are mixed by the balls in a ball milling machine, similar to that shown in figure 1.3 (§1.1.1 describes milling machinery in detail). As the balls collide, the powders are trapped causing them to deform and mix under a continued kneading action (figure 1.1). Although ball

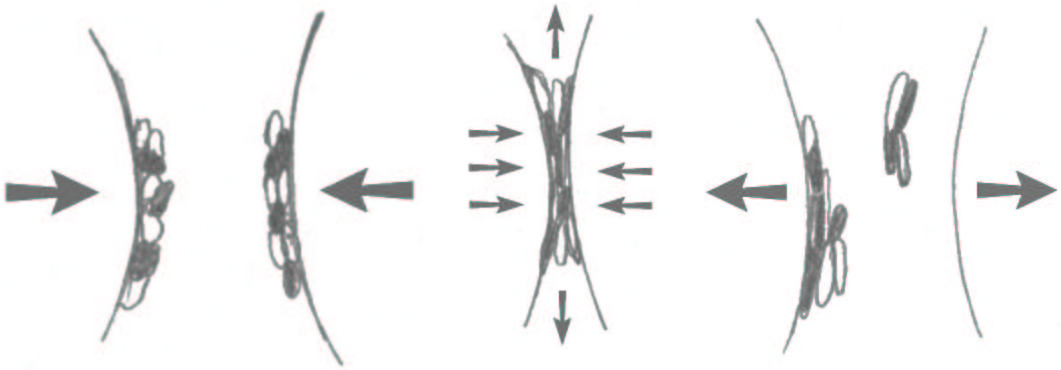

(a) Approach. (b) Impact. (c) Separation.

Figure 1.1: Powder is kneaded as milling media collide.

mills had previously been used by pyrotechnicians to mix metallic powders, Benjamin [7] was the first to specifically refine the structural properties of metallic material by ball milling. He created a nickel based superalloy using an attritor mill. The mill was originally designed to mix paints and inks but he used it to alloy a mix of pure and pre-alloyed metal powders and small sized ceramic dispersoids. He named the process "Mechanical Alloying."

Since then Mechanical Alloying has been applied to many different powder mixes. It has been found that different alloy systems react to milling in different ways depending on the mutual solubility and reactivity of the components, their mechanical properties and the type of milling equipment used. Despite these differences Benjamin and Volin [9] identify five progressive stages of alloying:

1. **Particle flattening**: the particles are flattened becoming flake-like.

2. **Welding predominance**: the flattened particles weld to form lamellar or layered composite particles.

3. **Equiaxed particle formation**: the lamellar particles are no longer

flake like, becoming thicker and rounded. The shape change is caused by the work hardening of the powders.

4. **Random welding orientation**: Fragments from the equiaxed particles start to weld in different orientations and the lamellar structure starts degrading.

5. **Steady state processing**: The structure of the material is gradually refined as fragments are taken from the particles that later weld with other fragments in different orientations.

Particles in each of the five stages are shown in Figure 1.2. It is commonly accepted that this five stage model accurately summarises the events observed in a typical alloying experiment, with some variation when powders with particularly unusual properties are milled. Most milling experiments are long enough to demonstrate stages 2 and 3, so our models focus on the earlier stages of milling.

As the MA process is complex it is convenient to look at just part of the processing when developing a model. Many models looking at changes in the milled powder can only be applied to a subset of these five milling stages. Further divisions have also been devised based on scale, with the following divisions commonly used:

- Mill scale: based on the dimensions of the mill chamber and milling media. At this scale the powder charge may be modelled as a continuum.

- Powder scale: based on the dimensions of a powder particle. Here only 2 mill balls need be considered to study the effects of a collision on the powder.

- Micro-scale: based on dimensions orders of magnitude smaller than a

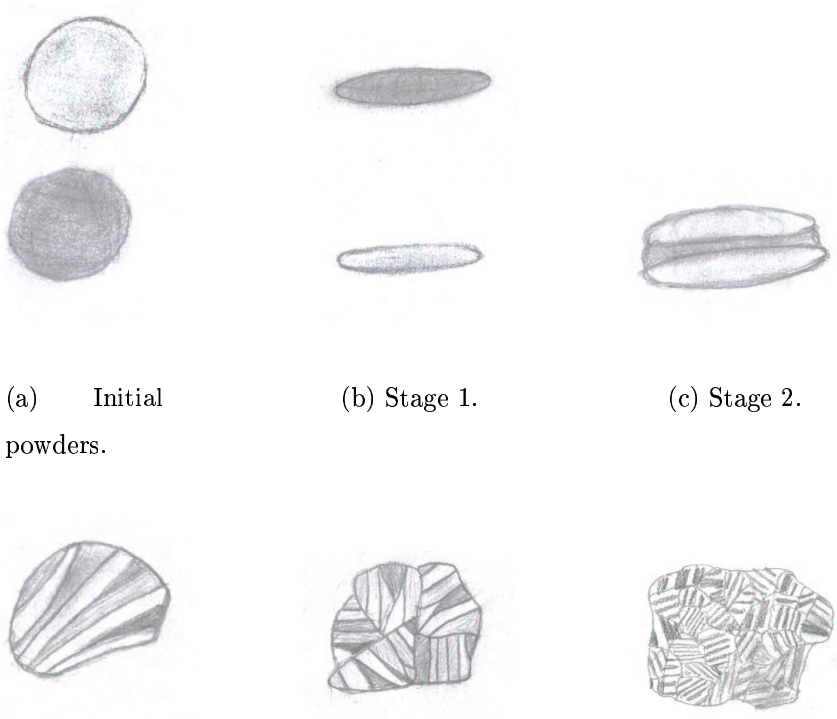

(a) Initial powders.

(b) Stage 1.

(c) Stage 2.

(d) Stage 3.

(e) Stage 4.

(f) Stage 5.

Figure 1.2: The five stages of Mechanical Alloying described by Benjamin and Volin [9]. Illustration after Maurice and Courtney [50].

powder particle (the dimensions of a lattice dislocation). Only the loading regime of the particle need be considered.

It is possible to develop a modelling approach that passes pertinent information between models at different scales. Maurice and Courtney [48, 50, 51] have used this approach to good effect. First they characterise the media collisions in a particular type of mill (mill scale modelling). This information is passed to a smaller powder scale model to look at the affect of the collisions on the powder charge. Other authors use energetics to bridge physical scales. For example Lü *et al.* [45] calculate typical impact energies in a tumbling mill and suggest that a minimum value is required for particle welding to occur.

One particular advantage of treating the problem at different scales is that the behaviour of the milling machinery can be examined without considering the powder charge, and *vice versa*. Studies have been made to this end, characterising different types of milling machinery, and different aspects of the powder morphology. The next section starts by looking at the mill scale, describing categories of machine and reviewing the modelling techniques that have been applied to each category. Further sections look at progressively smaller scales.

1.1.1 Modelling milling machinery

Characterising the motion of milling media is commercially important. For convenience, products are developed by milling small quantities of powder in a laboratory scale mill. The qualities of the powder product depend on the treatment imparted by the media, so milling parameters are adjusted in the laboratory to optimise the product. Once a product is finalised it will be manufactured in a larger production scale mill. The problem of tuning the production milling parameters to reflect the laboratory process is non-trivial.

Materials scientists have employed different mill designs to obtain a wide

range of milling conditions. All these designs trap powder using moving media but various methods can be employed to set the media in motion. Ball mills are usually classified using their drive mechanism and common mills fit into these four categories:

- Conventional tumbling ball mills
- Planetary ball mills
- Shaker or vibratory ball mills
- Attritors

The treatment imparted by each type of machine can be characterised using the distribution of collision frequency, angle and velocity within.

Models of milling machinery allow a laboratory optimised processing regime to be scaled up for production. Matching the media motion in the production mill to that in the laboratory mill expedites the process. Many researchers have suggested suitable characterisation techniques for this purpose, with some degree of success. The following sections introduce each category of mill, discussing associated milling characteristics and relevant modelling work.

Conventional Tumbling Ball Mills

Figure 1.3 shows a cross section through a conventional horizontal tumbling ball mill. The milling media are set in motion by rotating the chamber either on rollers (as shown) or using a shaft mechanism.

The simplicity of this design allows it to be scaled considerably, from small bench top mills with a diameters of 10–20 cm to industrial ball mills with chamber diameters of several metres. Larger diameter chambers produce a much higher collision intensity. Lü *et al.* [45] have analysed the motion of milling media in a tumbling mill using Newtonian mechanics and they state

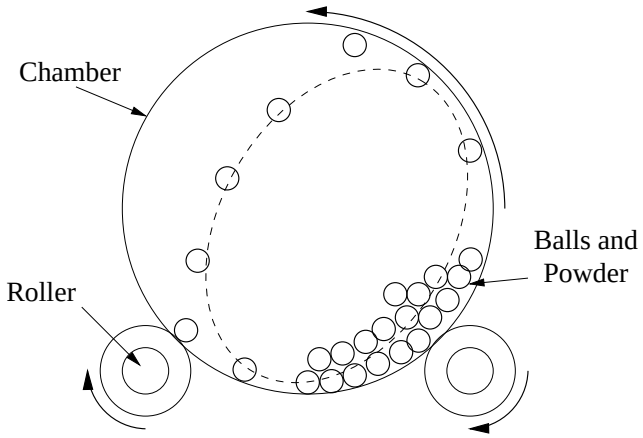

Figure 1.3: Schematic of a conventional or horizontal ball mill (end view).

that powders will not weld in small mill chambers where the collision intensity is too low, preventing alloying. Lü and Lai [43] suggest that the chamber of such mills should be at least 1 metre in diameter for efficient alloying to occur.

Watanabe *et al.* [69] have modelled tumbling mills (and many other types of mill) using a discrete element method. They track the motion of each mill ball under the forces of gravity and friction (for ball-ball contact and ball-wall contact). When collisions occur they account for elastic and plastic components of the collision by using Hertzian collision theory and a dashpot damper, respectively. The behaviour of the dashpot damper must accurately represent the energy absorbed by plastic deformation of the trapped powder. The necessary constants are obtained from Hashimoto *et al.* [29] who have measured the coefficient of restitution when a mill ball is dropped onto a powder layer of known thickness. Similar restitution experiments have been conducted by Huang *et al.* [32], who describe slight alterations to the spring and dashpot behaviour.

The simplicity of this mill design has many advantages, making it very practical at production scales. However, at small scales, gravity alone cannot provide the necessary milling intensity. Alterations have been made to the

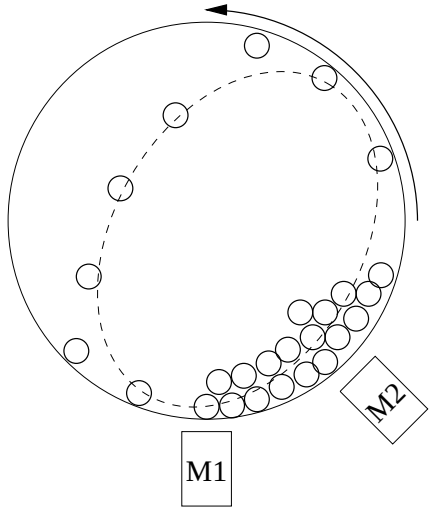

Figure 1.4: Schematic of a magnetically controlled horizontal ball mill (end view).

design to generate higher intensity collisions by applying additional forces to the media.

One variant adds magnets to the design as shown in Figure 1.4. The magnets attract the steel mill balls and increase their effective mass up to a maximum of 80 times. Magnet M1 increases the speed of cascading balls and magnifies attrition and abrasion effects. M2 accelerates the balls around the chamber, aiding the rotational attrition in the well of media near the bottom of the mill. Milling conditions can be varied by adjusting the magnets' position and strength.

The small size and mechanical simplicity of these designs allow extra controls to be added. Using a suitably sealed milling chamber it is possible to control atmospheric conditions and alter the pressure from vacuum to 500kPa overpressure. It is also possible to heat the chamber to around 450K by adding heating elements. These measures make tumbling mills very flexible.

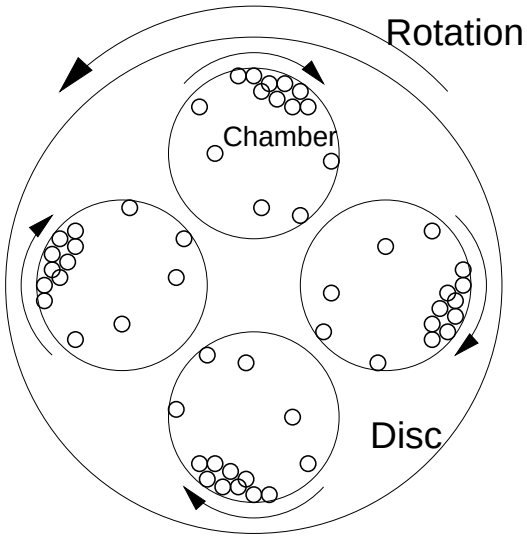

Figure 1.5: Schematic of a planetary mill (top view).

Planetary Ball Mills

Planetary mills use a centrifuge to boost their milling intensity. They frequently have more than one chamber as shown in Figure 1.5, but each chamber functions similarly to the horizontal mill. The mill chambers are mounted on a large rotating disc, forcing the milling media away from the centre of the disc to the outer-most part of the chamber wall. The chambers rotate in the opposite sense to the disc, causing the milling media to cascade in a manner similar to that observed in a horizontal mill, but with far greater intensity.

This type of mill is ideally suited to laboratory use as it has a sample sized capacity and can process several samples at once. The Pulverisette 5 made by Fritsch can use the following combinations of chamber number and capacity: 4×225ml, 4×125ml or 8×30ml. It offers a range of milling intensities obtained by varying the speed at which the components rotate.

Planetary mills have been modelled by Watanabe *et al.* [69] and by Dallimore and McCormick [13]. McCormick *et al.* [54] have filmed the media motion using a vial with a clear lid. They have processed their footage us-

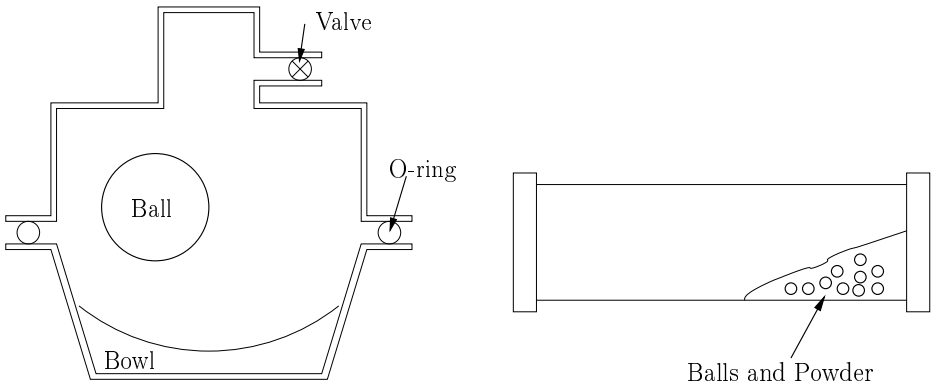

(a) Schematic of the chamber of a SPEX type mill.

(b) A cylindrical chamber employed on some vibratory mills.

Figure 1.6: Different chamber types used for vibratory milling.

ing image capture and processing software to provide quantitative analysis of media collisions that has been compared with models.

Shaker or Vibratory Mills

This type of mill provides extremely high milling intensities. The oscillating movements of the mill chamber cause more direct (head on) impacts than can be obtained using a rotary mill.

Figure 1.6(a) shows the features of the mill chamber used on the SPEX8000 mill manufactured by SPEX CertiPrep. The chamber is moved in an oscillatory fashion at frequencies of 50 or 60 Hz, causing the large mill ball to crush the powder against the chamber walls. The motor used has a power output close to 250 W.

Figure 1.6(b) shows a cylindrical mill chamber that uses a larger number of milling media. This type of chamber is used by the Megamill-5 from Dymatron Inc. The chamber vibrates at 60 Hz with an amplitude up to 2mm. The

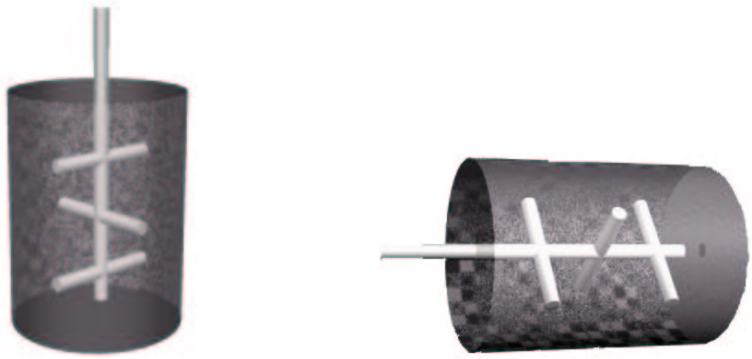

(a) Vertical. (b) Horizontal.

Figure 1.7: Schematic of attritor designs.

amplitude may be adjusted to alter the the milling intensity.

These vibratory mills are commonly used in laboratories, and can process material much faster than rotary style mills. The high energy collisions can complete powder reactions that are not observed in rotary mills. Unfortunately, the high energy requirements of these mills and the fierceness of their operation means they are not available on a production scale.

Models describing vibratory mills have been developed. Maurice and Courtney [52] consider the energy dissipation in a SPEX 8000 mill, basing their ideas on measurements made by Davis *et al.* [17]. Davis *et al.* videotaped the mill chamber and analysed the footage with computer software to determine the characteristics of collision events. Watanabe *et al.* [69] have extended their study to include vibratory mills similar to that made by Dymatron (figure 1.6(b)). Finally, McCormick *et al.* [54] have studied a vertical vibratory mill.

Attritors

The final mill type, attritors, are stirred ball mills. They have a cylindrical chamber filled with media. The media is driven by a rotating impeller. Figure 1.7 shows the two types of attritor, vertical and horizontal. Although the two designs are conceptually similar, changing the orientation of the mill chamber alters the milling regime significantly. The media will cascade in a horizontal attritor under the action of gravity [72]. In a vertical attritor the media form a close packed array. Rydin *et al.* [62] have studied the dynamics of the media in an vertical attritor, identifying packing arrays and measuring ball velocities at a variety of impeller speeds.

Attritors are flexible because of their simple construction. The chamber may be heated or cooled by passing liquid through a jacket layer. The impeller speed may be adjusted to control the milling intensity, and the atmosphere in the chamber can be altered if an adequate seal is made. The design can be scaled to suit laboratory work or production. However, even at the highest impeller speeds, the milling intensity is significantly lower than that obtained by vibratory ball mills.

1.1.2 Modelling particle geometry and mechanical mixing

The different mill types described in §1.1.1 all treat powders in a similar way. Deformation of the powder charge leads to the five identifiable stages of milling shown in Figure 1.2. This section reviews some studies that verify these alloying stages, looking at how particles weld, fragment and how these processes cause mixing. These changes occur at scales comparable to the size of a particle. The mixing that occurs within particles occurs at ever smaller scales as milling progresses, and links these effects with the detailed microstructural

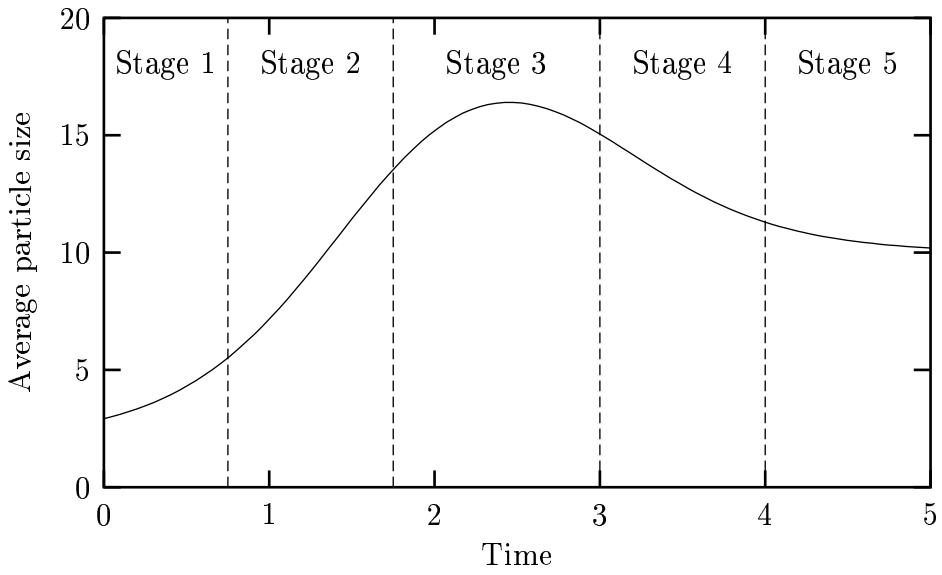

Figure 1.8: Idealisation of how average particle size changes during milling. Benjamin and Volin's five stages of alloying (see figure 1.2) are labelled. To summarise, in stage 1 particles are flattened, in stage 2 lamellar welding occurs, stage 3 forms equiaxed (lamellar) particles, stage 4 introduces random welding orientation and stage 5 refines particle structure.

changes that are discussed in the next section.

The illustration of Benjamin and Volin's five stage model in Figure 1.2 concentrates on the shape and structure of the particles, but the observations include implicit particle size variation. Typically, a milled powder will go through a stage of welding predominance (stage 2) during which the average particle size increases quite dramatically. Later in the milling process welding will be less common, and fragmentation may become prevalent before stage 5, where the two processes reach equilibrium. Figure 1.8 shows an idealised plot of average particle size evolving as milling progresses.

The changing balance between welding and fragmentation has been attributed to work hardening and surface effects [48]. Initial milling will deform

particles and spread any surface layer, exposing pure metal surfaces that easily cold-weld. As deformation continues the particles harden, becoming less likely to deform further and more prone to fracture.

Many authors have conducted experiments that study changes in powder size and shape during milling. Different alloy systems and mill types have been studied; examples are given in Table 1.1. Often these studies accompany the assessment of other powder properties, or are part of an experiment designed to test a particular hypothesis. For example, Rocha *et al.* [61] study the effect of adding a wax process control agent to the mill. The wax hinders particle welding and they find that alloying is delayed.

Population balance models have been used to follow the change in particle size observed in milled powders. Population balance models track welding and fragmentation events, calculating changes in the particle size distribution of the powder. They are based on classical reaction kinetics. The models presented later in this thesis, and introduced in §1.2, use population balance ideas so previous work in this area is particularly relevant.

Aikin *et al.* [3] and Aikin and Courtney [2, 1] have modelled both the size distribution and mixing characteristics of Cu, Cr, and Nb powders. Their models are based on the continuous coagulation-fragmentation equation [30, 41], but they later discretise the system. Aikin and Courtney's models differ from ours since they assume the frequency of welding and fracture events is independent of particle size and composition.

Population balance techniques have also been applied extensively to model the comminution of minerals [5]. Minerals are typically brittle and welding events are negligible and not considered. Kheifets and Lin [35] have used modified population balance models. They substitute the amount of energy supplied to the milling equipment where normally time would appear, and replace the temperature dependent reaction rate with a rate dependent on

Authors	Material	Milling Machinery
Aikin & Courtney [1]	Cu–15vol%Cr Cu–15vol%Nb	Vertical Attritor
Aikin & Courtney [2]	Cu Nb Cr	Vertical Attritor
Moshksar & Zebarjad [55]	Al	Tumbling Mill, $\emptyset$=10cm & $\emptyset$=13.5cm
Rocha *et al.* [61]	Cu–50wt%Ni	Horizontal Attritor (Netszche Molinex impeller design)
Guerrero-Paz & Jaramillo-Vigueras [27]	Cu-15wt%Al	Tumbling Mill, $\emptyset$=12.5cm
Huard *et al.* [33]	Mg–10vol%SiC_p Mg–20vol%SiC_p Mg–30vol%SiC_p	Tumbling Mill, $\emptyset$=29cm
Lu *et al.* [44]	Al–4.5wt%Cu/15wt%SiC	Tumbling mill.

Table 1.1: Some experimental powder size studies. The symbol $\emptyset$ denotes the internal diameter of the mill chamber, an important parameter affecting the impact velocity in tumbling mills.

milling intensity.

A more in depth modelling approach is adopted by Maurice and Courtney [48, 49, 50]. They develop a detailed model describing how a single collision affects an element of the milled powder. To do this they use empirical materials science relations and classical mechanics. A computer is used to repeatedly apply the model, subjecting the modelled powder to repeated collisions. Characteristics of the collisions occurring in certain types of milling machinery [62, 52, 53] are employed for this step. This method provides reasonable predictions of powder size, particle aspect ratio, the lamellar thickness within particles and material hardness.

Maurice and Courtney's study is widely regarded as the most successful and complete model of mechanical alloying. However, as a consequence of its complexity the model contains many assumptions that may be broken by atypical milling conditions or material properties. Also, it is difficult to identify exactly how changes in a particular parameter will change the model's predictions.

Some of the problems addressed by Maurice and Courtney have also been examined elsewhere in the literature. Huang *et al.* [32] measure the loading experienced by powder during a ball-vial collision using a free falling experiment. This confirms that a modified Kelvin model, previously used in computer simulations [13], best describes this type of collision. Lü *et al.* [45] discuss welding of powder particles, drawing analogies with the welding of two plates under pressure. Magini and Iasonna [47] have quantified the energy transferred to powder by a collision in a planetary ball mill. Finally, Podoprigora *et al.* [59] look at the loading experienced by particles in a vertical attritor.

Models at this scale are useful industrially. As well as modelling particle size effects, they are applicable to one of the most commercially viable applications of mechanical alloying: the production of dispersion strengthened

superalloys. Benjamin [7] and Fleetwood [20] develop such alloys based on the Ni–Al system. These alloys maintain high strength at high temperatures by combining two forms of hardening: dispersion hardening and γ' hardening. Both mechanisms inhibit the ability of the alloy to deform plastically by introducing hard inclusions that oppose internal flow. Dispersion hardening introduces inclusions by adding small particles of refractory oxide, nitride or carbide [20] to the alloy mix. γ' hardening is a more subtle process relying on properties of the Ni–Al alloy mixture. The mixture is chosen so that a hard γ' intermetallic phase is precipitated throughout the alloy. Mechanisms that cause chemical mixing to occur during mechanical alloying are discussed in the next section.

The dispersion hardening achieved during mechanical alloying is particularly useful. Conventional casting methods often fail because the dispersoids interact with the solidification front, driving them to the crystal boundaries. Mechanical alloying encapsulates the dispersoids in the powder particles at the welding interfaces. As mixing continues and more interfaces develop the dispersoids become evenly and intimately mixed. Gupta and Lavernia [28] study how successful this process can be under different milling conditions. Many people have studied mechanical alloying of Ni–Al alloys [26, 12, 11, 60, 45, 19, 56], following the commercial success of the alloys produced by INCO [20]. Powder scale models encompass all the processes necessary for prediction of dispersoid mixing. Maurice and Courtney's model is particularly successful in this respect.

The interplay between mechanical and chemical mixing of constituent powders has proved a particular asset of MA. Benjamin [8] reported that mechanical processing will generate an ever finer lamellar structure within particles until, eventually, the powders chemically combine to form a true alloy. This was demonstrated by milling magnetic Ni powder with Cr. Cr is not mag-

netic, nor is its alloy with Ni. After sufficient processing the milled product was shown to be non-magnetic, verifying that the powders were truly alloyed. Models and mechanisms for this alloying process take place at the atomic scale within powder particles. Such processes are discussed in the next section.

1.1.3 Modelling dislocations, diffusion and reaction processes

Mechanical Alloying allows the previously discrete alloying process (where material was either alloyed or composite) to be treated in a more continuous way. As milling progresses, powders combine chemically in new and interesting ways. The product may or may not resemble the equivalent alloy manufactured by conventional means.

The continuous nature of the alloying process can be exploited for gain. A new consolidation process, called self-propagating high-temperature synthesis (SHS) [42] has been developed in which powders are partially mechanically alloyed, then cold compacted into a mould, and ignited. The powder mixture must be chosen carefully so that a self propagating reaction is set up in the compacted powder. The reaction generates heat, softening the powder and possibly causing expansion (since the product of the reaction may occupy more volume than the reactants). A consolidated component is obtained that has very little porosity. Mechanical alloying allows the degree of mixing and reactivity of the precursor powder to be adjusted to optimise the SHS reaction. A related processes is reactive milling [66] where milled material will spontaneously react inside the mill once it is sufficiently well mixed.

As has been stated many times before, the source of novel properties in mechanically alloyed powders is the deformation process. This generates a highly disordered structure within the processed particles. Plastic deformation of metals requires the movement of dislocations within the crystal structure (see

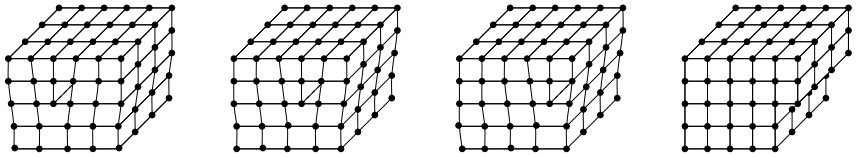

(a) Edge dislocation.

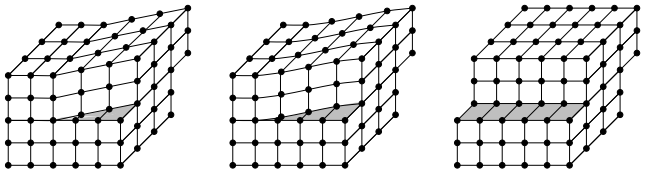

(b) Screw dislocation.

Figure 1.9: Metallic crystals deform plastically as lattice defects migrate within the crystal.

Figure 1.9). Movement of dislocations can be inhibited by many factors, for example foreign solute atoms in the crystal lattice, hard inclusions of foreign material or, importantly, the presence of other dislocations. Pinned dislocations can form an emitting dislocation source, for example by forming a Frank-Read source (see figure 1.10). As dislocations become entangled work hardening occurs. The material becomes more difficult to deform as dislocations snag and pile up. The crystal structure becomes more disjointed and disordered.

Work hardening of metals [10] is a complex phenomenon under ongoing investigation (for example, see [38, 4, 39, 31, 40, 57, 36]). It has been noted that initial work hardening can be related to the strain experienced by the material. After considerable deformation the crystal grain size within the material is reduced as dislocations collect, forming new grain boundaries. Once this process begins the Petch relation is used to relate yield strength, S, and

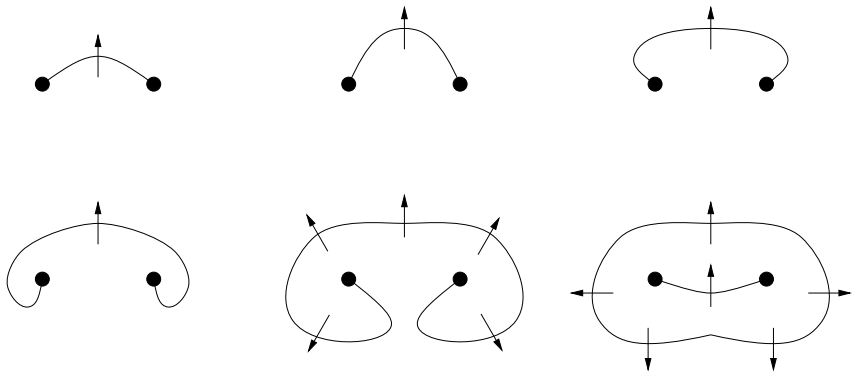

Figure 1.10: When a dislocation becomes pinned at two points an emitting dislocation source may be created. The lines represent the advancing crystal defect which moves in the direction indicated by the arrows. Locally, the material is experiencing a shear stress on a plane parallel to the paper, oriented vertically.

grain size d, such that $S = S_0 + kd^{-1/2}$, where S_0 and k are empirical material constants [21]. The material hardness then can be calculated using the common approximation $S = 3H_v$, where H_v is the Vickers hardness of the material. No universally applicable model of hardening has been found, which complicates modelling of hardness changes in milled powders.

Refinement of grain size is a topic of study in its own right. The highly disordered structures formed during the deformation process are metastable. The associated energy can be measured with calorimetric analyses [65]. Amorphous structures can be produced, similar to those formed by liquid quenching and proton irradiation [68]. Structures with small or no grain structure can be recrystallised with controlled heating (annealing). By aligning the growing crystals within a component it is possible to create beneficial anisotropic properties. Small grain size is also required for the new super-plastic forming process. Here, specially prepared metal sheets are vacuum formed, a forming method more commonly connected with plastics. Godfrey *et al.* [24, 25]

have studied Ti–6wt%Al–4wt%V alloys with boron additives suitable for this purpose.

Structural deformation of the material and chemical alloying phenomena are closely linked. Jiang *et al.* [34] have milled Fe and Cu, noting that while Fe crystals are naturally body-centred cubic (see figure 1.11(a)), milling causes the material to form a face-centred cubic structure (figure 1.11(b)). The Fe then dissolves in the face-centred cubic Cu lattice. The formation of supersaturated solid solutions [23] and intermetallic phases [46] has been studied and modelled. Ma and Atzmon [46] have found that mechanical alloying can produce metastable phases that cannot be manufactured using other methods. Pabi [58] model diffusive intermixing and propose an effective temperature for diffusion in mechanically alloyed particles that is unrelated to the local temperature increase during collision, but may be related to the liquidus temperature of the material. Badmos and Bhadeshia [6] apply thermodynamic arguments to model the formation of solid solutions as a consequence of continued mixing, predicting energy barriers within certain systems that will prevent mechanical alloying. Schwarz [64] suggests that dislocations at the interface between lamellae allow accelerated localised interdiffusion. Future deformation will move the dislocations to new sites, leaving high concentrations of solutes behind. Diffusion is accelerated at the dislocations' new place of rest, so dislocations act as mobile solute-pumping stations. Khina [37] reviews many models that look at reaction phenomena and phase formation.

The complex interplay between chemical and deformation processes makes models at this scale extremely complex. It is clear that changes in the powder's chemistry and structure will affect models at larger scales: if the macroscopic properties of the powder are changed by variations in structure and composition then the powder's propensity to weld or fragment will change also. This area of modelling is the most complex as different alloy systems behave in

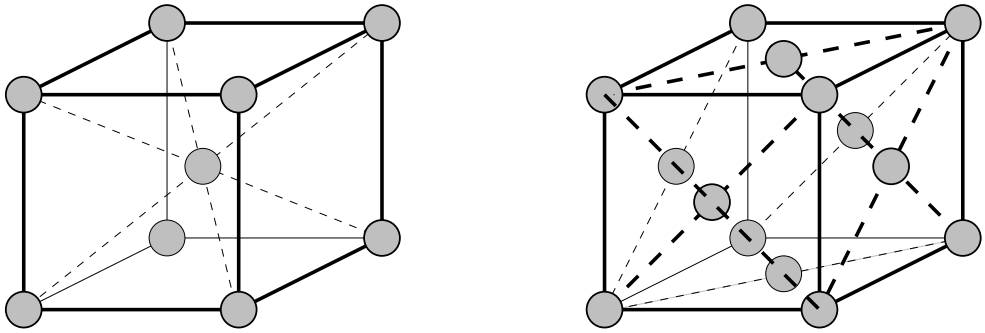

(a) Body centre cubic

(b) Face centre cubic

Figure 1.11: Crystal structures.

different ways, and there is ongoing discussion over which are the pertinent alloying and work hardening mechanisms.

Our models work on the larger powder scale and are concerned with welding and fragmentation events. The next section introduces the models used, explaining that the microscale effects described in this section are, for the most part, averaged and treated as constant. This is a necessary approximation at this juncture, as the small scale modelling is too complex to incorporate in a model such as ours at the moment.

1.2 The coagulation-fragmentation model

There are many systems, like the mechanical alloying process that evolve solely by some combination of aggregation and fragmentation processes. Mechanical alloying is one example, but others include liquid phase sintering, aerosol agglomeration [18] and the aggregation of alumina powder in $n-$heptane or water [63]. These systems are of interest and are often of industrial importance, so attempts have been made to model them. Many different models have been suggested for slightly different situations. The model applied here

was first proposed by von Smoluchowski in 1917 [67].

Smoluchowski's model uses clusters of discrete size. The smallest particle that can be represented is of size 1 and has volume V. These size 1 particles are referred to as monomers. The next largest particle is of size 2 and has a volume $2V$. Each particle can be viewed as a cluster of monomer particles. In the following discussion an r-sized cluster is represented by C_r, and the concentration of C_r clusters (sometimes written $[C_r]$ by chemists) is written c_r or $c_r(t)$, as the model is concerned with how the cluster size distribution changes over time. The concentration, c_r, is the number of r-sized clusters per unit mill volume.

The concentrations will change as particles weld and fragment. We can model the welding and fragmentation processes as though they were chemical reactions between different clusters. For example, a welding event may involve a cluster of size 5 and one of size 3. The product would be a cluster of size 8. In the notation of chemical reactions we write

$$C_5 + C_3 \xrightarrow{a_{5,3}} C_8. \tag{1.1}$$

Here $a_{5,3}$ is the rate at which clusters of size 5 and clusters of size 3 weld. More generally we can write

$$C_r + C_s \xrightarrow{a_{r,s}} C_{r+s}, \tag{1.2}$$

which describes all possible welding events. Fragmentation events provide the reverse reaction

$$C_{r+s} \xrightarrow{b_{r,s}} C_r + C_s. \tag{1.3}$$

The rate $b_{r,s}$ is the rate at which particles of size $r+s$ fragment to particles of size r and s; this is distinct from the total rate of fragmentation of particles of size $r+s$.

Now, consider one particular particle size, r, say. The change in the concentration of r-clusters due to all the associated welding and fracture events

can be calculated. There are four categories of event

- gain by welding (two smaller particles weld to give one of size r)

$$C_{r-s} + C_s \xrightarrow{a_{r-s,s}} C_r, \tag{1.4}$$

- loss by fragmentation (the reverse reaction)

$$C_r \xrightarrow{b_{r-s,s}} C_{r-s} + C_s, \tag{1.5}$$

- loss by welding (a particle of size r welds with another to form a larger particle)

$$C_r + C_s \xrightarrow{a_{r,s}} C_{r+s}, \tag{1.6}$$

- gain by fragmentation (a larger particle breaks giving an r-sized fragment)

$$C_{r+s} \xrightarrow{b_{r,s}} C_r + C_s. \tag{1.7}$$

The effect each category has on the concentration of r particles, c_r, can be calculated in turn. Consequently the time rate of change of concentration, $\dot{c}_r$ can be calculated.

In order for a particular process to take place the reactants must be present. The likelihood of a particular reaction occurring is therefore proportional to the concentration of the reactants, for example, the reaction (1.4) will happen at a rate proportional to $c_{r-s}c_s$. The constant of proportionality is the reaction rate $a_{r-s,s}$. The rate at which the concentration of r particles rises as a result of smaller particles welding can be expressed by summing the contributions given by each valid value of s,

$$\frac{1}{2}\sum_{s=1}^{r-1} a_{r-s,s}c_{r-s}c_s. \tag{1.8}$$

The factor $1/2$ appears because each combination of sizes is counted twice by the convolution-like term (c_1 and c_{r-1} appear in the term with $s = 1$ and the term with $s = r - 1$).

The other three contributions can be calculated in a similar way. The rate at which particles of size r are lost by fragmentation to all fragment combinations is

$$\frac{1}{2}\sum_{s=1}^{r-1} b_{r-s,s}c_r. \tag{1.9}$$

Calculating the other two terms gives the following system of differential equations

$$\dot{c}_r = \frac{1}{2}\sum_{s=1}^{r-1}\left(a_{r-s,s}c_{r-s}c_s - b_{r-s,s}c_r\right) - \sum_{s=1}^{\infty}\left(a_{r,s}c_r c_s - b_{r,s}c_{r+s}\right) \tag{1.10}$$

This is the equation system proposed by Smoluchowski. It is commonly used to model particle aggregation and fragmentation phenomena and forms the basis of the modelling to follow. The aggregation rates $a_{r,s}$ and $b_{r,s}$ have to be specified before the model can be used. This topic is addressed in Chapter 2.

Full solutions to Smoluchowski's model are calculated, when required, using numerical techniques. However, for particular choices of $a_{r,s}$ and $b_{r,s}$ some characteristics of the cluster size distribution can be determined analytically. This fact is used later, in Chapter 2, and is discussed in more detail there. For now, it is convenient to define the p^{th} moment of the distribution by

$$M_p(t) = \sum_{r=1}^{\infty} r^p c_r(t), \tag{1.11}$$

and note that M_0 is the total number of particles in the system and $M_1 = \rho$ is the fraction of the system's volume occupied by particles. The particles are assumed incompressible, so ρ is constant. Higher moments could be used to calculate other quantities like the polydispersity of the size distribution, $M_0 M_2/M_1^2$, a quantity analogous to the variance about a mean in statistics.

When solving the full system given in equation (1.10), numerical techniques are employed. To make this possible the system must be truncated. There are two commonly applied truncation schemes. In both schemes, the first summation term is not altered, as it deals exclusively with clusters whose size

is less than or equal to r. The first scheme,

$$\dot{c}_r = \frac{1}{2}\sum_{s=1}^{r-1}\left(a_{r-s,s}c_{r-s}c_s - b_{r-s,s}c_r\right) - \sum_{s=1}^{N-r}\left(a_{r,s}c_r c_s - b_{r,s}c_{r+s}\right), \tag{1.12}$$

reduces the upper limit of the second summation term so that interactions with clusters outside the truncated model are prevented. Mass is conserved as clusters with size greater than N cannot be formed. Particles of size r may only weld with particles of size up to $N - r$. Particles with size approaching N will experience almost no welding events at all. Thus mass, $M_1 = \rho$, is conserved. The significance of this depends on the forms chosen for $a_{r,s}$ and $b_{r,s}$.

The second truncation scheme does not conserve mass in the same way:

$$\dot{c}_r = \frac{1}{2}\sum_{s=1}^{r-1}\left(a_{r-s,s}c_{r-s}c_s - b_{r-s,s}c_r\right) - \left(\sum_{s=1}^{N} a_{r,s}c_r c_s - \sum_{s=1}^{N-r} b_{r,s}c_{r+s}\right). \tag{1.13}$$

Welding is not restricted and material can aggregate to form clusters larger than N that are not fragmented back into the system. The significance of these effects depends on the forms of $a_{r,s}$ and $b_{r,s}$ chosen. For these truncated systems it makes sense to use a truncated expression for the moments of the size distribution M_p.

$$M_p = \sum_{r=1}^{N} r^p c_r(t). \tag{1.14}$$

Then, the mass conserving case given in equation (1.12) has $\dot{M}_1 = 0$ and the rate at which material is lost from form the system when using equation (1.13) is

$$\dot{M}_1 = -\sum_{r=1}^{N} r c_r \sum_{s=N-r+1}^{N} a_{r,s}c_s. \tag{1.15}$$

If most of the material remains at the small end of the size domain then the truncation error with either scheme will not be important. Otherwise, the relative errors must be assessed. The scheme applied in later chapters is the first, mass conserving case. Experimental reports suggest almost all of the

material put into a mill is recovered at the end of milling, so this seems the most appropriate scheme to apply. Ideally N is chosen large enough that the difference between the two schemes is negligible, but if N is small (due to computational constraints) then differences can be relevant.

Part I

One Component Systems

Chapter 2

Modelling Theory

In the course of the previous chapter (§1.2) Smoluchowski's coagulation-fragmentation equations were introduced. Here we discuss a method of using these equations to model milling experiments involving a single powder material. Part II of the thesis looks at models that involve two powder types.

Smoluchowski's equations, given in Equation (1.10), require a form to be specified for the aggregation and fragmentation rates $a_{r,s}$ and $b_{r,s}$. This chapter presents some possible choices of $a_{r,s}$ and $b_{r,s}$ that are suitable for modelling ball milling. These welding and fragmentation rates are used in different combinations to form five distinct models. To illustrate the different behaviour induced by using different rates, two of the models are directly compared.

Each of the proposed rates includes two factors. The first is a kernel: a function of r and s specifying a particular dependence on particle size. The second is a constant rate-parameter that adjusts the propensity for welding or fragmentation in the model for particles of all sizes. These rate-parameters allow each model to be matched to experimental results by balancing the tendency of particles to weld and fragment. The quality of the predictions made by each model will be assessed in later chapters by applying the models to experimental data.

The kernels have been chosen so that $M_0(t)$ can be determined or approximated analytically. This is key in later chapters that make comparisons between the model and experimental results; comparisons require a simple solution for $M_0(t)$. The rate-parameters appear in the solution for $M_0(t)$ and can be determined by fitting the solution to experimental measurements. The analysis used to determine $M_0(t)$ for each model is presented in §2.2. Experimental measurements of $M_0(t)$ are made in two stages. The next chapter presents a experimental procedure that measures the size distribution of milled material. The subsequent chapter discusses how M_0 may be estimated from experimentally measurable quantities before comparing these experimental distributions to those predicted by the models.

2.1 Size dependent kernels

The aggregation and fragmentation rates used take the form

$$a_{r,s} = a\, f(r,s), \tag{2.1}$$

$$b_{r,s} = b\, g(r,s). \tag{2.2}$$

To model aggregation, three kernel functions, $f(r,s)$, are considered: 1, $(r+s)$ and (rs). The first two of these three forms forms are also used for $g(r,s)$ (fragmentation). Kernels are combined to form five models, employing the combinations of aggregation and fragmentation rates given in Table 2.1. In order to be consistent with later definitions we refer to the constants of proportionality, a and b, as the aggregation rate parameter and the fragmentation rate parameter respectively. These terms are used to refer to the size independent part of the aggregation and fragmentation rates, which describes the material's overall or averaged tendency to weld or fracture.

The forms given in Equations (2.1)–(2.2) make the implicit assumption that aggregation and fragmentation rates, $a_{r,s}$ and $b_{r,s}$ depend only on the sizes of

Model	$a_{r,s}$	$b_{r,s}$
1	a	b
2	$a(r+s)$	b
3	$a(r+s)$	$b(r+s)$
4	$a(rs)$	$b(r+s)$
5	$a(rs)$	b

Table 2.1: Welding and fracture rates used in the various models. In each case, a and b are constant rate-parameters to be determined.

the particles involved, namely r and s. In reality, a number of factors will cause the rates will vary throughout the milling. For example work-hardening will cause the material to become more brittle, increasing the fragmentation rate as milling progresses. In a similar way the presence of surface impurities may reduce early aggregation rates and the heat generated during milling may increase aggregation rates at later times. Variation can affect both the size independent rate-parameter and the size-dependent kernel form, but it is assumed that all these effects are secondary to size dependent factors. The aggregation and fragmentation rates presented here are averaged over the duration of the milling process. A more refined model could consider time-dependence, though this would add considerable complexity to the model, with many more parameters to be determined.

In order for a particle to aggregate or fragment it must be involved in a collision between milling media. Particles will experience collisions at different frequencies depending on their size and this variation must be reflected in both aggregation or fragmentation rates. Given that a particle of a certain size is involved in a collision, the chances of it aggregating or fragmenting will also be size-dependent. Both contributions must be present in an accurate model.

Our first model is the simplest of all, having no size dependence. The

aggregation and fragmentation rates are constant, *i.e.* $a_{r,s} = a$ and $b_{r,s} = b$. This model is similar to that employed by Aikin and Courtney [2] and has been shown to provide a good first approximation to the observed behaviour. In this simple size independent case, the rates and rate-parameters are synonymous, but this is not true of the other models.

Models 2 and 5 generalise model 1, using aggregation rates that are size-dependent while maintaining a size-independent fragmentation rate. In model 2 the aggregation rate is proportional to the sum of the sizes of the aggregated particles or equivalently the size of the agglomerate formed. In model 5 the rate depends on the product of the sizes of the particles before combination. This shows a more pronounced size dependence: consider a system of sizes $r = 1 \ldots N$, where N is a large number; then in model 2 rates vary from $2a$ to $2Na$, whereas in model 5 they range from a to N^2a. To compensate for this, it is expected that model 5 will give a smaller value of a when both model 5 and model 2 are fitted to the same data.

Models 3 and 4 also use the same size-dependent aggregation rates as models 2 and 5 but introduce a size-dependent fragmentation rate as well. We consider a rate that depends linearly on the size of the particle before fragmentation, and is independent of the sizes of fragments produced. In this case the constant of proportionality is defined to be b, and reflects the average fracture characteristics of the material.

Previous mathematical analysis [15] has shown that the rate $a_{r,s} = ars$ represents a very strong aggregation effect. In the absence of any fragmentation process this effect is so strong that the model will lose powder through a process called gelation. After a certain time, t_g, the strong aggregation leads to a divergence in the system, where an "infinitely large" particle forms. The divergence is interpreted as the limit of a process in which larger clusters collide forming even larger clusters at an accelerating rate, to form a single

macroscopic entity. Such models may apply to experiments where significant amounts of powder are lost due to adhesion to the milling equipment. However, finding the parameters for these models is a difficult task as the solution for $M_0(t)$ is altered by the divergence. The time at which the divergence occurs is, in turn, determined by the rate parameters. The effect of gelation on the models is discussed further in §2.2.4.

It is possible to show that a particle's likelihood of experiencing collision is proportional to its size. This proportionality is incorporated in the aggregation rate $a_{r,s} = a(rs)$ (in models 4 and 5) and the fragmentation rate $b_{r,s} = b(r+s)$ (in models 3 and 4). These rates assume that when a large particle experiences a collision it is just as likely to fragment as a small particle experiencing the same collision. The other aggregation and fragmentation rates do not increase as quickly with size, as they incorporate a component that reduces the likelihood of an impacted particle aggregating or fragmenting as the particle's size increases.

Many factors which influence the likelihood of particles aggregating or fragmenting are not size-dependent, for example powder hardness and milling intensity. These contributions are averaged over time and incorporated in the model through aggregation and fragmentation rate parameters, a and b. The values of a and b are determined from experimental data using a matching technique, so the influence of each factor does not need to be found explicitly.

2.2 Solutions for $M_0(t)$

The previous section established size dependencies for the rates $a_{r,s}$ and $b_{r,s}$. This section provides one of the tools used to systematically determine the rate-parameters, a and b: an analytic solution for $M_0(t)$ is found for each model. The rate-parameters are found by fitting these solutions to experimen-

tal estimates of M_0 calculated in Chapter 4 from the measurements made in Chapter 3.

The analysis required to determine a solution for each model is presented in the following sections. Solutions can be calculated from Equation (1.10) by substituting for $a_{r,s}$ and $b_{r,s}$, then summing from $r = 1$ to $r = \infty$ using generating function techniques described in [15, 16]. The resulting differential equations are solved exactly or, if necessary, using asymptotic approximations based small fragmentation rate.

To avoid repetition it is convenient to re-order this process. Summing equation (1.10) first, then re-ordering the summations reduces the amount of analysis required after model specific substitutions are made. In general, the change in the p^{th} moment of the distribution with respect to time may be written

$$\dot{M}_p = \sum_{r=1}^{\infty} r^p \dot{c}_r. \tag{2.3}$$

Substituting for $\dot{c}_r$ from equation (1.10) gives

$$\dot{M}_p = \frac{1}{2} \sum_{r=2}^{\infty} \sum_{s=1}^{r-1} r^p w_{r-s,s} - \sum_{r=1}^{\infty} \sum_{s=1}^{\infty} r^p w_{r,s}, \tag{2.4}$$

where $w_{r,s} = a_{r,s} c_r c_s - b_{r,s} c_{r+s}$. Re-ordering the first summation gives

$$\dot{M}_p = \frac{1}{2} \sum_{s=1}^{\infty} \sum_{r=s+1}^{\infty} r^p w_{r-s,s} - \sum_{r=1}^{\infty} \sum_{s=1}^{\infty} r^p w_{r,s}. \tag{2.5}$$

Then re-scaling the first r summation using $r' = r - s$ yields

$$\dot{M}_p = \frac{1}{2} \sum_{s=1}^{\infty} \sum_{r'=1}^{\infty} (r' + s)^p w_{r',s} - \sum_{r=1}^{\infty} \sum_{s=1}^{\infty} r^p w_{r,s}, \tag{2.6}$$

which allows the sums to be combined

$$\dot{M}_p = \frac{1}{2} \sum_{r=1}^{\infty} \sum_{s=1}^{\infty} w_{r,s} \left\{ (r + s)^p - 2r^p \right\}.$$

Finally, substituting for $w_{i,j}$,

$$\dot{M}_p = \frac{1}{2}\sum_{r=1}^{\infty}\sum_{s=1}^{\infty} a_{r,s}c_r c_s \left\{(r+s)^p - 2r^p\right\} - \frac{1}{2}\sum_{r=1}^{\infty}\sum_{s=1}^{\infty} b_{r,s}c_{r+s} \left\{(r+s)^p - 2r^p\right\} \tag{2.7}$$

or,

$$\dot{M}_p = A_p - B_p \tag{2.8}$$

$$\text{where } A_p = \frac{1}{2}\sum_{r=1}^{\infty}\sum_{s=1}^{\infty} a_{r,s}c_r c_s \left\{(r+s)^p - 2r^p\right\} \tag{2.9}$$

$$\text{and } B_p = \frac{1}{2}\sum_{s=2}^{\infty} c_s \sum_{r=1}^{s-1} b_{r,s-r} \left\{s^p - 2r^p\right\}. \tag{2.10}$$

These relationships make it easy to determine differential equations for M_0. After setting $p = 0$, the forms for $a_{r,s}$ and $b_{r,s}$ given in Table 2.1 are substituted in equations (2.8)–(2.10) for each model in turn.

2.2.1 Model 1

In model 1, $a_{r,s} = a$ and $b_{r,s} = b$. From equation (2.9)

$$A_0 = -\frac{1}{2}a\sum_{r=1}^{\infty} c_r \sum_{s=1}^{\infty} c_s = -\frac{1}{2}a{M_0}^2 \tag{2.11}$$

and from equation (2.10)

$$B_0 = -\frac{1}{2}b\sum_{r=1}^{\infty} c_r(r-1) = -\frac{1}{2}b(\rho - M_0). \tag{2.12}$$

Hence (equation (2.8))

$$\dot{M}_0 = -\frac{1}{2}[aM_0^2 - b(\rho - M_0)], \tag{2.13}$$

which is a Ricatti equation solved exactly by

$$M_0(t) = \frac{2}{a}\left(\frac{p_1 + K_1 p_2 e^{(p_2 - p_1)t}}{1 + K_1 e^{(p_2 - p_1)t}}\right), \tag{2.14}$$

where

$$p_1 = \frac{-b - \sqrt{b^2 + 4ab\rho}}{4}, \qquad p_2 = \frac{-b + \sqrt{b^2 + 4ab\rho}}{4}, \tag{2.15}$$

so that

$$p_2 - p_1 = \sqrt{b(a\rho + b/4)} \tag{2.16}$$

From initial conditions,

$$K_1 = \frac{2p_1 - aM_0(0)}{aM_0(0) - 2p_2}, \tag{2.17}$$

which completely specifies the solution.

2.2.2 Model 2

Model 2 uses the same fragmentation kernel as model 1, so B_0 is given by equation (2.12). The aggregation rate, $a_{r,s} = a(r + s)$ gives

$$A_0 = -a\rho M_0 \tag{2.18}$$

so

$$\dot{M}_0 = -\frac{1}{2}[2a\rho M_0 - b(\rho - M_0)]. \tag{2.19}$$

This has solution

$$M_0(t) = \frac{b\rho}{2a\rho + b}(1 - e^{-(a\rho + b/2)t}) + M_0(0)e^{-(a\rho + b/2)t}. \tag{2.20}$$

2.2.3 Model 3

The fragmentation rate for model 3 is $b_{r,s} = b(r + s)$, but the aggregation rate is unchanged from model 2. Applying similar methods,

$$\dot{M}_0 = -\frac{1}{2}[2a\rho M_0 - b(M_2 - \rho)], \tag{2.21}$$

which includes the second moment M_2. M_2 is unknown, but determined by

$$\dot{M}_2 = 2aM_2\rho - \frac{b}{6}[M_4 - M_2]. \tag{2.22}$$

This equation (found using equations (2.8)–(2.10)) involves terms in M_4, again unknown. The equation for M_4 will contain terms with higher order moments, so some other method of solution must be found. We apply asymptotic methods to equations (2.21)–(2.22) assuming b to be a small parameter, giving a first order solution for systems with weak fragmentation: $M_2(t) \sim M_2(0)\exp(2atM_2(0))$ and hence

$$M_0(t) \sim M_0(0)e^{-a\rho t} + \frac{b}{6a}\left[3(1-e^{-a\rho t}) + \frac{M_2(0)}{\rho}\left(e^{2a\rho t} - e^{-a\rho t}\right)\right]. \quad (2.23)$$

The approximation cannot be valid if the leading order term is smaller than the first correction term, so the solution is valid for a finite time

$$t < t_{\max} = \frac{1}{3a\rho}\log\left(\frac{6a\rho M_0(0)}{bM_2(0)}\right). \quad (2.24)$$

The accuracy of the solution falls dramatically as t approaches $t_{\max}$. The consequences of this limitation are discussed later.

2.2.4 Model 4

Asymptotic methods are applied to model 4, where

$$\dot{M}_0 = -\frac{1}{2}[a\rho^2 - b(M_2 - \rho)], \quad (2.25)$$

and

$$\dot{M}_2 = aM_2^2 - \frac{b}{6}[M_2 - M_4], \quad (2.26)$$

giving an approximate solution $M_2 \sim M_2(0)/(1 - aM_2(0)t)$ and

$$M_0(t) \sim M_0(0) - \frac{1}{2}a\rho^2 t - \frac{1}{2}b\left(\rho t + \frac{1}{a}\log(1 - aM_2(0)t)\right), \quad (2.27)$$

for

$$t < t_{\max} = \frac{1 - e^{-2aM_0(0)/b}}{aM_2(0)}. \quad (2.28)$$

This model uses the last aggregation rate, $a_{r,s} = a(rs)$, which causes a phenomenon called gelation. Gelation has been studied by Davies *et al.* [15],

and is discussed in §2.1. Davies *et al.* study a purely aggregating system that can be obtained from equation (1.10) (with the appropriate rates) by setting $b = 0$. In this case $B_p = 0 \; \forall \; p$ and

$$A_p = \frac{1}{2} \sum_{r=1}^{\infty} \sum_{s=1}^{\infty} a(rs) c_r c_s \left\{ (r+s)^p - 2r^p \right\}. \tag{2.29}$$

When $p = 1$ this simplifies to

$$A_1 = \frac{1}{2} a(M_1 M_2 - M_1 M_2) = 0, \tag{2.30}$$

suggesting that M_1 is constant (by equation (2.8)). However, when $p = 2$, $A_2 = a{M_2}^2$ so

$$M_2(t) = \frac{M_2(0)}{1 - M_2(0)at} \tag{2.31}$$

which has a finite time singularity at $t = t_g = 1/aM_2(0)$. The divergence corresponds to the formation of a macroscopic particle or gel. Material aggregates from the system to the gel-particle and is effectively lost from $\{c_r(t)\}_{r=1}^{\infty}$, so the number of clusters will also be affected. Physically, the presence of weak fragmentation in the system should be of little significance but will slow the onset of gelation slightly. Consequently, we can safely say that the solution, equation (2.27), is valid provided the asymptotics hold and $t < t_g$. For times before gelation ($t < t_g$), $\dot{M}_1 = 0$ so we will be concerned with the interval $0 < t < t_g$ where $M_1(t) = M_1(0) = \rho$.

2.2.5 Model 5

Although model 5 uses the gelating aggregation kernel, the corresponding differential equation

$$\frac{\mathrm{d}M_0}{\mathrm{d}t} = -\frac{1}{2}[a\rho^2 - b(\rho - M_0)], \tag{2.32}$$

can be solved exactly by

$$M_0(t) = \frac{b\rho - a\rho^2}{b}(1 - e^{-bt/2}) + M_0(0)e^{-bt/2}. \tag{2.33}$$

The leading order expression for the gel-time, $t_g = 1/aM_2(0)$ is the same as for model 4.

Having found these solutions for $M_0(t)$ it is easy to illustrate how the different kernel forms affect the progress of the model. Solutions for models 2 and 5 have the same functional form (equation (2.20) and equation (2.33)). Values for the rate-parameters a and b can be devised such that $M_0^{(2)}(t) \equiv M_0^{(5)}(t)$ for all t, where $M_0^{(X)}(t)$ is $M_0(t)$ for model X. Size distributions can be calculated by numerically integrating Equation (1.12) to show how the different kernels produce different size distribution characteristics. Even though $M_0^{(2)}(t) \equiv M_0^{(5)}(t)$, the cluster size distributions functions will be different since they show more detailed information.

2.3 Idealised calculations

This section compares the size distributions generated by models 2 and 5 to illustrate the behavioural differences of the kernel forms used. Initial conditions are chosen that represent a hypothetical monodispersed powder, as shown in Figure 2.2(a). This makes it clear which particles have been formed through welding and which through fragmentation. Values of a and b have been chosen so that $M_0^{(2)}(t) \equiv M_0^{(5)}(t)$. The solution functions are equivalent if

$$a^{(2)} = \frac{a^{(5)}}{2}, \tag{2.34}$$

$$b^{(2)} = b^{(5)}\, a^{(5)}\, \rho, \tag{2.35}$$

so values of a and b are chosen to satisfy these conditions. Furthermore, to avoid problems with gelation in model 5 it is prudent to ensure that $a^{(5)} \ll 1/(M_2(0)t)$, for all values of t considered.

The parameter values given in Table 2.2 adhere to these relationships and avoid problems with gelation. The corresponding change in $M_0(t)$ is shown in Figure 2.1. Of course, the curves for model 2 and model 5 are identical. Note

Model	a	b
2	0.0005	0.0010
5	0.0010	0.0020

Table 2.2: Parameters used to illustrate the differences between models 2 and 5.

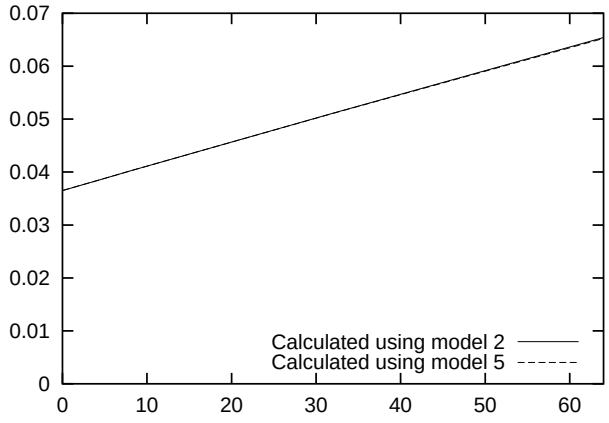

Figure 2.1: $M_0(t)$ for models 2 and 5 calculated using equations (2.20) and (2.33) and the values of a and b given in Table 2.2. The two curves are identical by design.

that an increase in M_0 (the concentration of particles in the mill) reflects a reduction in average particle size as the volume of the milled material remains constant.

Figure 2.2 illustrates how the monodispersed particles between $r = 25$ and $r = 30$ weld freely under these conditions, creating peaks around $r = 55$, $r = 82.5$, $r = 110$ etc. Particle fragments of all sizes are created more slowly, filling the gaps between the peaks. If no fragmentation occurred then particles of certain sizes would not be formed — there would be a peak where $25 \leq r \leq 30$ and one at $50 \leq 60$ with no material between $r = 30$ and $r = 50$.

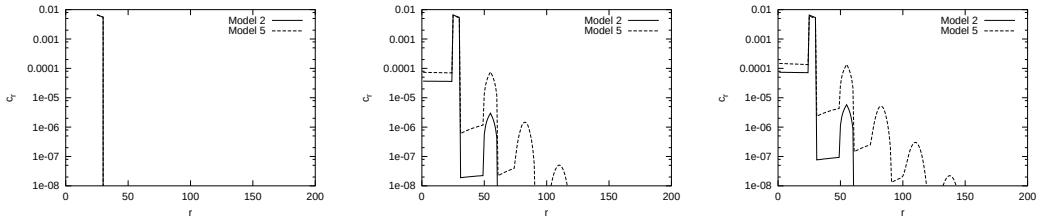

(a) Initial distribution. (b) 1 hour. (c) 2 hours.

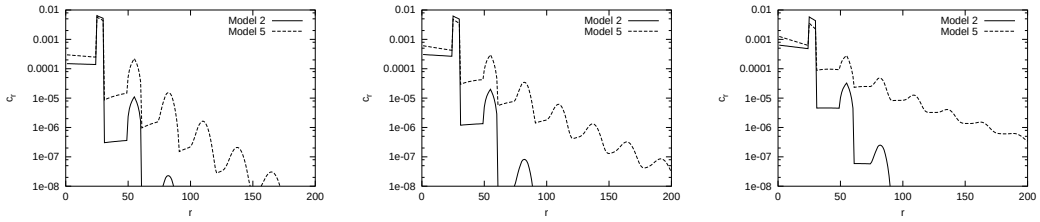

(d) 4 hours. (e) 8 hours. (f) 16 hours.

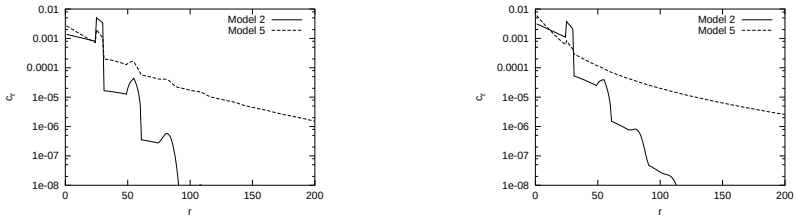

(g) 32 hours. (h) 64 hours.

Figure 2.2: Cluster size distributions calculated numerically from equation (1.12) using the parameter values in Table 2.2.

As time progresses the distributions become smoother as more fragments are generated and recombined, forming clusters of all sizes. The profile that develops is influenced by the choice of aggregation and fragmentation rates $a_{r,s}$ and $b_{r,s}$. Model 5 welds more rapidly than model 2, so the cluster distribution develops a shallower gradient (see figure 2.2(h)). The distribution in model 2 is progressing toward a smooth convex curve, while the distribution for model 5 will remain concave (however, note the logarithmic scales). This means that the particle size distribution in model 5 is more even — model 5 has a larger variation in particle size that model 2. The greater number of large particles is important, as it incurs a greater truncation error. As discussed in §2.2.4 and §2.2.5, the aggregation kernel used in model 5 is strong enough to generate particles of infinite size in finite time. When fragmentation is absent this occurs after time $t_g = 1/(aM_2)$. A similar phenomenon will occur in model 4.

These calculations have been made using an idealised initial distribution different from those used experimentally to highlight which particles have been formed by aggregation and which by fragmentation. The processes described here and and the qualitative differences between the models will be exhibited irrespective of the the initial conditions. Model 5 was shown to have higher concentrations of larger and smaller particles than model 2, despite both models having the same average particle size (the size variation is much larger in model 5). $M_0(t)$ solutions for the other models have slightly different functional forms but all (except that for model 4) are exponential in t and they can be closely matched.

The predicted size distributions are compared to experimental measurements to identify which model gives the most accurate predictions. For example, if an experiment gave a wide variation in particle size then model 5 would be more useful than model 2 and *vice versa*. By comparing the models to a wide variety of experimental situations it is possible to identify which model

is best overall. The next chapter describes a suitable milling experiment using ferro-silicon powder. The experimental data is analysed in Chapter 4. Further data sets obtained from the literature are analysed in Chapter 5.

Chapter 3

Experimental Method and Results

The previous chapter developed a procedure capable of predicting the size distribution of a milled metallic powder. This chapter describes experimental work used to test the procedure. Data from the experiments will be compared to predictions made by the models. The results of this comparison show which of the proposed aggregation and fragmentation rates mimic the mechanical alloying process most accurately. From this knowledge we infer some details of the processing received by the powder from the milling machinery. The comparison of models and experimental data is made in later chapters.

For the experimental study several samples of ferro-silicon powder were milled in a horizontal attritor. The size distribution of each sample was determined using a sieve stack mounted on an automated shaker machine (see Figure 3.3 for an illustration). Each sample was milled for a different length of time. It is assumed that each sample will be treated in the same way, so the samples milled for shorter times reflect a state surpassed by samples enduring longer milling times. Hence the results describe the size distribution of the milled powder at specific points in time. Two separate sets of experiments

were conducted using different milling speeds.

A successfully processed sample experiences three stages of preparation and then a final stage of analysis:

1. Sample preparation and standardisation.
2. Milling.
3. Sample division.
4. Size analysis (sieving) and other studies.

These processing stages are described in the sections that follow. The sample preparation and division stages serve only to ensure that the experimental results are accurate so the necessary actions are noted quite briefly. However the milling and analysis stages require more careful thought and involve many more parameters so they will be discussed at more length.

3.1 Sample preparation

A 10kg drum of ferro-silicon powder was obtained from Hogänäs. A kilogram of this powder was taken for each experiment and mixed thoroughly within itself using a Turbula mixer[1] before being carefully weighed into 100g samples. The mixing procedure ensures that each sample is representative, or statistically identical, notably having identical size distribution characteristics.

3.2 Sample processing

The samples were processed using a Zoz Simoloyer CM01[2]. This machine has a horizontal attritor design; a schematic is shown in Figure 3.1. The cham-

[1] type T2C, made by Willy A Bachofen ACT Maschinenfabrik, Basel, Switzerland.
[2] Zoz Maschinenbau GmbH

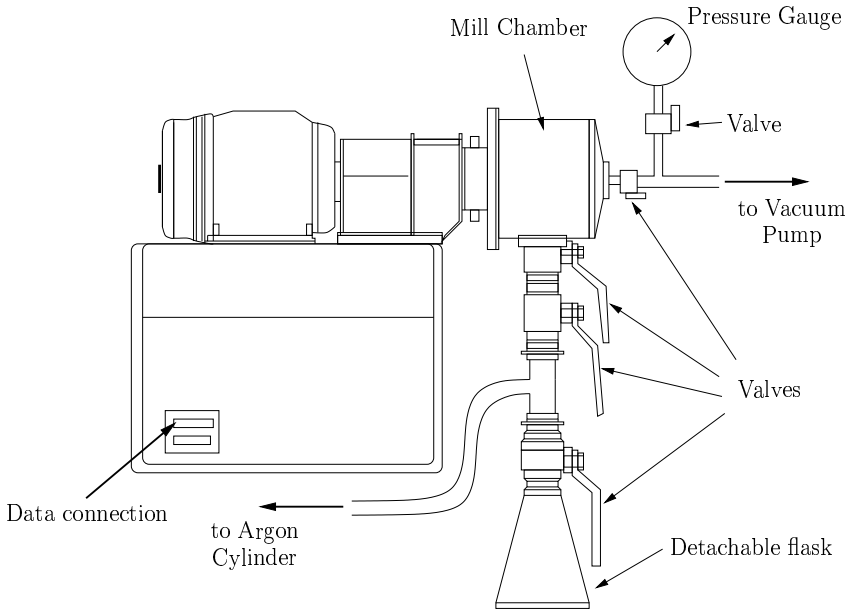

Figure 3.1: Schematic of experimental apparatus.

ber had been used previously to manufacture an aluminium-nickel alloy and to mill limestone so it was cleaned using sand blasting equipment. The first two milling experiments were discarded as they may have been affected by transient behaviour resulting from the cleaning process and by ferro-silicon adhering to the chamber walls. After a couple of batches have been processed a steady state develops. The amount of material adhering to the chamber wall will be approximately equal to the amount detaching from the wall, having been deposited from previous batches. Although our model does not explicitly account for these events, such mixing is inevitable in any batch milling technique. A useful model must work under these circumstances so no attempt was made to stop this "historical contamination". We expect the errors incurred to be small because only a small amount of material will be involved in the process, particularly when using a hard material like ferro-silicon.

The rotational speed of the Zoz milling machinery is computer controlled, allowing the operator to prescribe a sequence of milling speeds for the machine

to follow. A previous study conducted by Zoz *et al.* [71] has shown that the amount of material recovered after milling can be greatly improved (increased) by varying the milling speed in a cyclic way. This operation avoids what Zoz *et al.* term critical milling behaviour — the phenomenon where one area of the mill consistently experiences conditions that promote deposition of material onto the chamber wall. Cyclical operation moves such "dead" regions. By carefully selecting milling speeds it is possible to ensure material deposited during one speed regime is dislodged while the machine is running at a different speed or during transitional periods. In reference [71] a cycle in which the machine runs at 1300 rpm for 4 minutes and 900 rpm for 1 minute was used to manufacture a Ti-Al-Nb alloy in a machine identical to the one used here. The milling cycle was complemented by a discharged cycle in which the timings were reversed (*i.e.* 1300rpm for 1 minute, 900 rpm for 4 minutes).

Preliminary tests showed that almost all of our ferro-silicon powder was recovered using these cycles, so they were adopted for a full experiment. A second experiment was conducted in which all the milling speeds were reduced using a factor $1/\sqrt{2}$, giving 919 rpm instead of 1300 rpm and 636 rpm instead of 900 rpm. The idea behind this scaling was to reduce the velocity of the balls by a factor $1/\sqrt{2}$ and consequently reduce the kinetic energy dissipated at impact by a factor 1/2. The scaling ignores a lot of geometric factors and does not take account of the fact that the balls cascade in significantly different ways at different mill speeds [72], but this approximation provides an interesting way to choose a second set of milling conditions.

Milling was conducted under an inert argon atmosphere, allowing the powder to develop consistent characteristics after the dispersion of initially oxidised surface material. This makes the experiment more suitable for comparison with our model, which assumes constant aggregation and fracture rates for the powder. If the powder gradually accrued more oxidised material one would

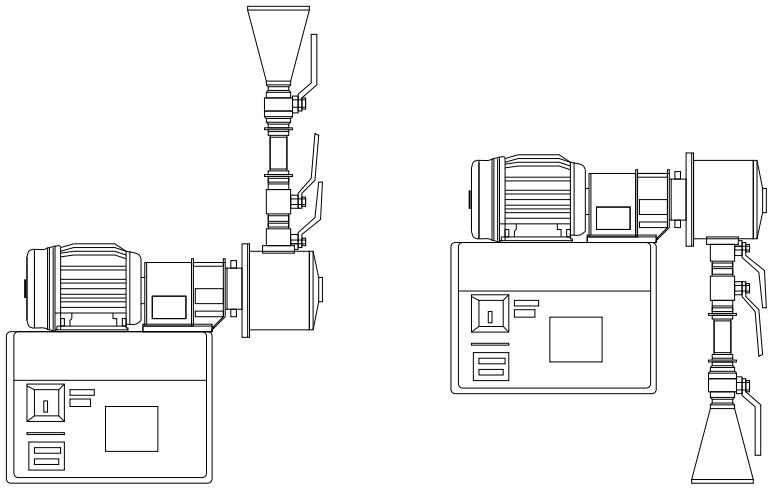

(a) Milling position.

(b) Discharging position.

Figure 3.2: Zoz Simoloyer CM01 with the chamber in two different modes.

expect it to become harder and more brittle after longer milling times, and so weld less and fracture more.

The selected milling times increase geometrically, reflecting our expectation that the process will exponentially tend to a limiting equilibrium. In the high power experiment that used rotational speeds of 1300rpm and 900rpm, samples were milled for times of 1, 2, 4 and 8 hours. For the half power experiment, these times were doubled, giving a range from 2 hours to 16 hours. After a sample has been treated for the prescribed milling period, the chamber was inverted to the discharging position (see Figure 3.2) and run for a further half hour under the dicharging cycle to ensure that all of the material from the mill was collected for analysis. This means that the collected powder may have been in the mill for up to half an hour longer than the specified time. This is not ideal, but we anticipate that the majority of the powder will be discharged from the mill early in the discharging period, and recognise that any error

incurred will be systematic.

3.3 Sample division

After milling, the samples were mixed in the Turbula mixer again, before being divided into a 50g sample used for sieve analysis, and a 15g sample saved for SEM and EDX work. The remaining material was saved for future unforeseen analyses.

3.4 Sample analysis

The size distribution of the samples have been examined by sieving. Some SEM work has been carried out to determine the shape of the particles before and during milling. The SEM study was not exhaustive but sufficient to determine the general characteristics of particle shape. EDX was used to check that contamination of the samples during milling was low. The techniques used for each study are described below. Results of the sieving and SEM work are also shown.

3.4.1 Sieving

Sieved data are usually presented using a bar chart. Powder is passed through a stack of sieves of decreasing mesh size. The passage of the powder through the sieves is aided by a standardised shaking method that ensures reproducibility. The percentage of the powder mass passing through each sieve mesh, but remaining on the mesh below is then plotted against the larger mesh size. Figure 3.3 shows a fictitious size distribution and the corresponding sieve stack, with the positions of the different size fractions labelled.

Our sieve analyses were conducted using a regular set of woven wire test

Sieve size (microns)
425
300
212
150
106
75
53
38

Table 3.1: Sieve sizes used for particle size analysis.

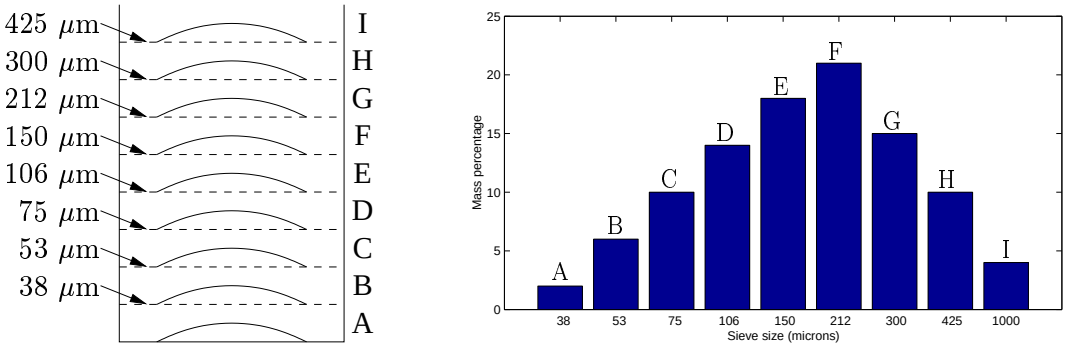

(a) Sieve stack

(b) Size distribution

Figure 3.3: Generating a size distribution bar chart from a sieving experiment. (a) shows a sieve stack, with the powder fractions labelled A–I. The corresponding bars are shown in (b). Note the labelling of the x-axis. The final bar, labelled 1000 microns represents all material that will not pass the 425 micron sieve. The figure 1000 has been chosen by examining the particles: all would pass through a 1 mm sieve mesh.

sieves manufactured by Endecotts and conforming to BS. 410: 1986. The range of sieve apertures used was not changed; a list of the apertures is presented in Table 3.1. The material was sieved while dry, using an Endecotts Octagon Digital sieve shaking machine. Initial tests showed no discernible difference in measurements made by sieving a test powder for 5, 10 and 20 minutes, so all the samples were sieved for 10 minutes to ensure completion.

The size distribution data presented in Figure 3.4 were obtained by following this procedure. When the mill was run at full power, the powder quickly aggregated forming relatively large particles in a bimodal distribution, as shown by Figure 3.4(a). At later times more intermediate-sized particles are formed from both the smallest and largest particle classes, smoothing the distribution profile over time. The half power experiment shows a discernibly different pattern. In this case the particle size gets progressively larger over time, as shown in Figure 3.4(b), indicating a trend of gentle aggregation.

As with any experimental measurements, these sieved size-distribution data are subject to error. Several possible sources of error have been eliminated. It was noted that more than 97% of the milled powder was recovered after every experiment, so losses of powder are not large. The small loss observed could be attributed to residues remaining in the filling column and receiving flask. It was also noted that small amounts of fine powder are inevitably lost when handling the powder, so it is thought that inaccuracies would be greater for the smaller size ranges.

There are also systematic errors associated with the use of sieving equipment. While the size of the apertures in a sieve mesh should be identical there will always be some variation, with some apertures being larger than others. This sort of error increases with the age of the sieve as the mesh deteriorates with use. Despite these errors, it is felt that the distributions give and reasonably accurate and reproducible representation of the particle size changes

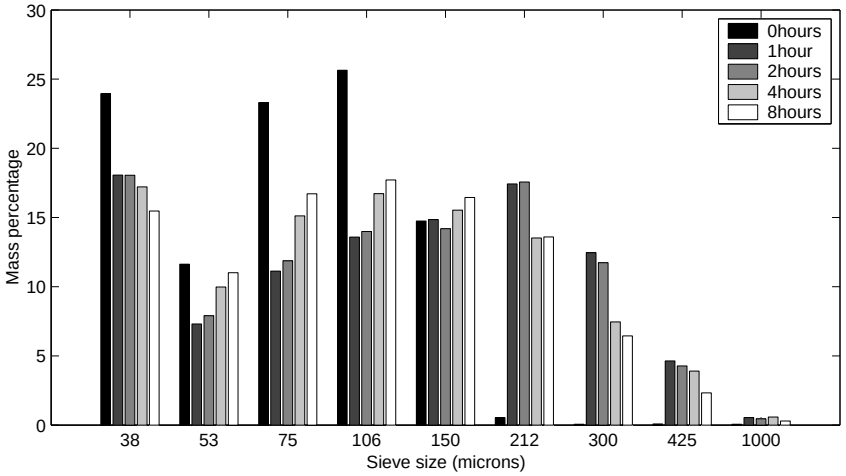

(a) Full power.

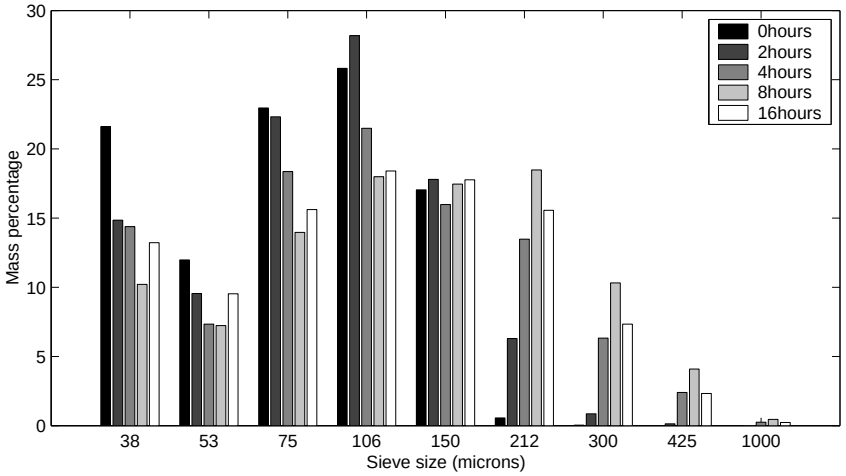

(b) Half power.

Figure 3.4: Temporal change in particle size distribution of ferro-silicon powder obtained using a Zoz Simoloyer at different speeds.

occuring within the powder.

3.4.2 SEM and EDX analyses

Brief SEM and EDX studies were conducted on the powders. SEM analyses looked at the shape and structure of the milled powder particles while the EDX study investigates the chemical composition to determine whether the samples were being contaminated by material from the mill wall.

Approximations of particle shape are used by our modelling procedure to convert sieved size analyses to volumetric particle size measurements. Confirming the shape of powder particles by SEM is therefore important. Our models assume that particles can be represented by disk shapes or short cylinders. This assumption is valid for the early stages of milling, during stages 1 and 2 of Benjamin and Volin's five stages description [9] (see figure 1.2). In stage 3 the particles become equiaxed so these assumptions are invalid.

Some of the powders from the full power ferro-silicon milling experiment have been examined using a Jeol WINSEM JSM-6400 scanning electron microscope. The investigation showed flake particles developing from the equiaxed (gas atomised) starting powders (see Figure 3.5). Samples taken after 2, 4 and 8 hours of milling were examined. It was subjectively noted that as milling time progresses, the number of flake-shaped particles increased. There were no signs of equiaxed particle formation (stage 3 in Figure 1.2). This suggests that our assumption of disk-like particle shape will be suitable for this experiment.

In addition to the SEM work, a cursory EDX analysis was made of the early samples to see if there was significant contamination of the material. No traces of contamination could be found when analysing 3 or 4 spots on each sample.

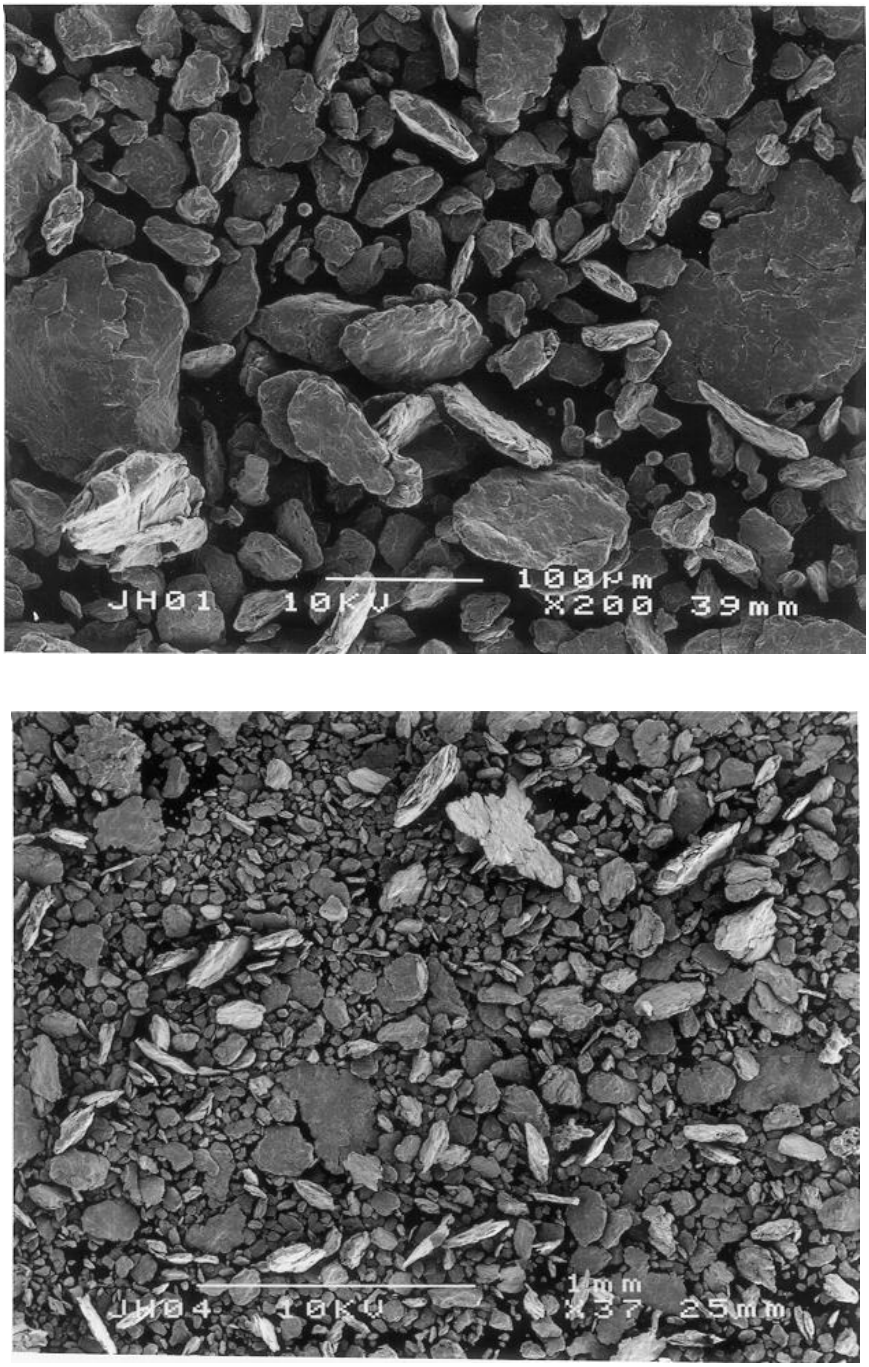

Figure 3.5: Micrographs of the milled ferro-silicon powders. Small, equiaxed particles are shown that have escaped heavy processing during their time in the mill. The larger flake-like particles become more common as milling progresses.

Chapter 4

Verifying The Models

The previous chapter describes the experimental procedure used to determine changes in the particle size distribution of ferro-silicon powder during milling. Results of the experimental study are summarised in Figure 3.4. In this chapter, the models presented in Chapter 2 will be used to calculate size distributions that are are compared with the experimental results, identifying which models are the most realistic.

Two technical issues must be resolved before making such comparisons. The first concerns the different methods of quantifying particle size used by experiments and the model. These differences are resolved using the technique presented in §4.1. The second issue concerns finding suitable aggregation and fragmentation rate-parameters for use with the model. A fitting technique suitable for this purpose is presented in §4.2.

Having resolved these issues, §4.3 makes the comparison between the model predictions and experimental results. The comparison is discussed at some length, noting reasons why some models succeed and others fail. Chapter 5 makes many similar comparisons, using experimental data taken from literature to cover a wide range of milling scenarios.

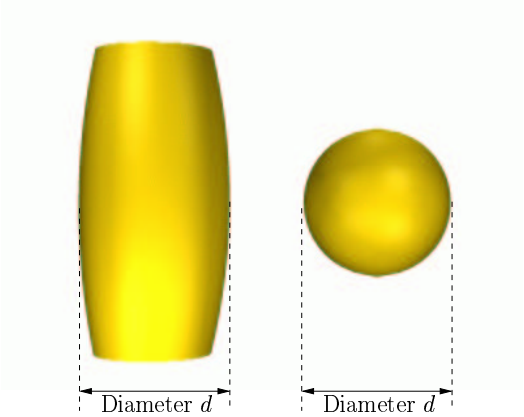

Figure 4.1: Particle geometry is important when interpreting size measurements obtained by sieving. Both the particles shown will pass through a sieve with aperture greater than d but the particle on the left has a much higher volume.

4.1 Converting size measures

There are many techniques available for measuring the size distribution of metallic powders but the most commonly used technique is sieving. This choice is economic, easy to understand and convenient to use. However, the measurements obtained are rather abstract and can be difficult to interpret. Sieving measures the second largest dimension of a particle, as shown in Figure 4.1. This is not the most useful or intuitive measure of particle size in the context of our models. The volume of a sieved particle will depend on the particle geometry. In addition, practical limits on the number of sieve meshes available allow only a relatively coarse discretisation of the size distribution.

The cluster models described in Chapter 2 provide a more detailed discretisation of the powder distribution, often employing thousands of different cluster sizes. However, these sizes are a measure of volume and *a priori* take no account of the aspect ratio of particles. An accurate conversion between the sieve measurements and volumetric size measurement relies on a resampling

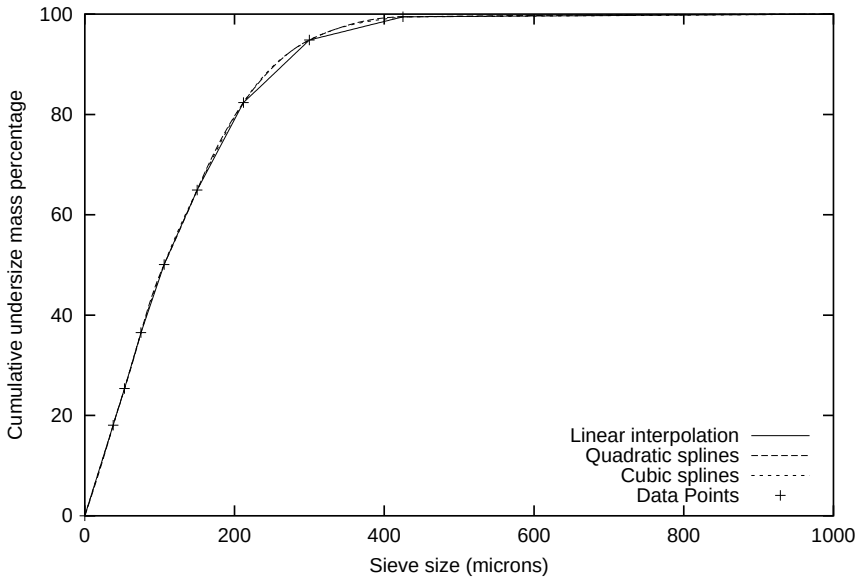

Figure 4.2: Interpolating a cumulative undersize size distribution. The data is taken from the initial powder used in the full power experiment. The data points are determined experimentally and the three near-identical lines are generated by different interpolation techniques.

of the size distribution using interpolation techniques. Accurate resampling is achieved by considering the cumulative size distribution of the powder. Figure 4.2 shows the cumulative distribution associated with the unmilled powder from the full power experiment. The data points in Figure 4.2 are determined experimentally while the distribution at intermediate sizes is readily interpolated using a number of techniques.

Three interpolation techniques were considered: cubic splines, quadratic splines and linear interpolation. Figure 4.2 shows that both cubic and quadratic spline fitting techniques produce a marginally smoother fit to the size distribution between 200 and 400 μm. Nonetheless, linear interpolation was selected for use with all data sets because it eliminates the possibility of generating a fitted function which has a locally negative gradient. Such a fitted function

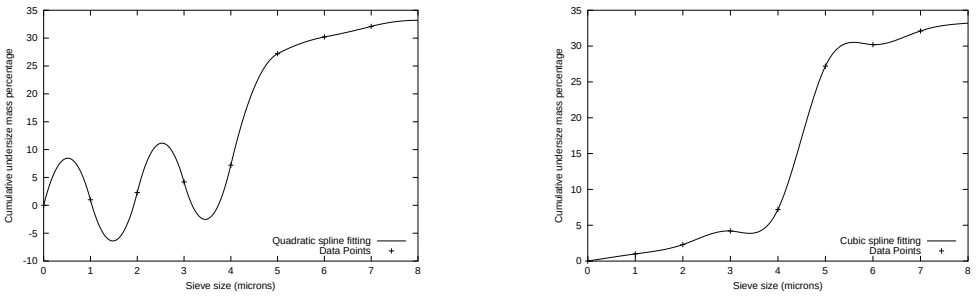

(a) Quadratic Splines.

(b) Cubic Splines.

Figure 4.3: Quadratic or cubic spline fitting may interpolate a monotonically increasing data set with regions of negative gradient.

would be a problem as a cumulative distribution must, by definition, be monotonically increasing. With quadratic and cubic splines the possibility exists for oscillations (regions of negative gradient) to develop, as illustrated in Figure 4.3. These oscillations occur when the gradient of the cumulative distribution changes abruptly.

Linear interpolation is used to construct a continuous approximation of the cumulative particle size distribution, measuring the particles' sizes in terms of sieve mesh sizes. A volumetric particle size distribution must be calculated from this data, but making the conversion requires knowledge of the particle geometry. The following work assumes that particle shape can be approximated by a disc, as shown in Figure 4.4. This assumption is typically valid for early milling times. Equiaxed particles begin to form at later times, as the material hardens (Figure 1.2). When assuming disc-like geometry it follows that the sieve mesh-size measures the disc's diameter directly, so the calculation required to convert sieve mesh sizes to a volumetric measure is not as problematic as Figure 4.1 suggests.

The proposed models allow the thickness of the disc to vary with diame-

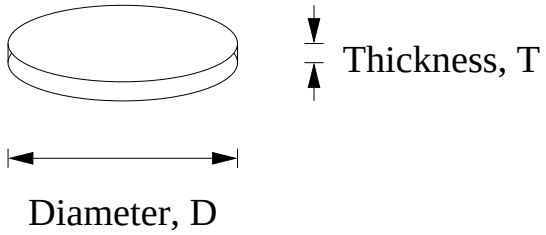

Figure 4.4: Geometry used to model a powder particle.

ter. A suitable relationship has not been determined from the experiments. Instead we have tried two *ad hoc* assumptions. SEM observations suggest that particle thickness may not vary significantly, so a constant particle thickness is assumed. This first approximation is called the "constant thickness disc approximation". A different approximation was found necessary for less malleable powders. A second case is proposed for these particles, where larger particles are thinner according to the relationship $T = k/\sqrt{D}$. This case is referred to as the "thinning disc approximation" of particle size. Both methods are applied to a set of data, and the more successful relationship is selected *a posteriori*.

This transformation represents a non-dimensionalisation of the size data. Sizes are now expressed in terms of an arbitrarily sized monomer. For each experiment, the disc diameter associated with a monomer is chosen so that the smallest particles measured experimentally can be represented by the model. This ensures that, at worst, the smallest sieve size is represented by $c_1(t)$, and the next sieve size by $c_2(t)$. Meeting this criteria will ensure that larger sieve sizes are represented by many different cluster sizes as the larger sieve sizes cover a wider range of particle volumes. The largest particle size present in the model is fixed by selecting a suitable point of truncation. The truncation size N (discussed in §1.2) is chosen so that the model can generate particles at least as large as those observed experimentally. Reducing the monomer

size and increasing N will increase the accuracy of the computed solution but it is important to balance these benefits against the assosciated increase in computational requirements. A typical compromise would be $N = 1000$.

It is not always possible to infer the largest size of particle present in the mill directly from sieving results. The largest sieve mesh will catch any particles too large to pass through, with no upper size limit. It is good practise to choose a sieve stack so that the largest sieve mesh allows all or nearly all of the material to pass through. Where this is not the case common sense must be applied. In the absence of any other indication it may be assumed that the next sieve size in the series would not catch much powder. In the case of systems with very strong aggregation it may be necessary to consider the size of the milling media as an upper limit to particle size. Often, though, some evidence of maximum size is present, for example SEM micrographs or commentary in the text.

These interpolation and transformation algorithms provide approximate volumetric cluster size distributions from the experimental data. The initial powder distribution for each experiment is converted to provide an initial condition for the models. Then distributions at later times are calculated by numerically integrating the Smoluchowski coagulation-fragmentation equations (equation (1.12)) from this initial state. Calculated distributions are compared to those measured experimentally. However, before it is possible to make such calculations, the rate parameters a and b must be fixed, using the following method.

4.2 Determination of rate parameters a and b

The rate parameters, a and b, impose a time scale and a balance between the welding and fracture events in each model. When choosing parameters the goal

is to make the model's behaviour closely mimic the experimental behaviour. Optimal values of a and b must be chosen to achieve this. Values are found by fitting the average particle size to that measured experimentally. Then each model is run using the same initial conditions. The different model systems evolve different particle size distributions over time because each uses a unique combination of kernels. The distributions can be compared with experimental measurements to see which model reflects the experiment most accurately and hence which combination of kernel forms is the most realistic.

The previous section discussed interpolation and transformation techniques that generate volumetric cluster size distributions from experimental measurements. It is trivial to calculate a value of M_0 (the total number of particles in the system) from such a distribution. Since experimental measurements are made at a range of times, data points can be obtained that chart changes in $M_0(t)$. The analytic functions for $M_0(t)$ obtained in §2.2 (equations (2.14), (2.20), (2.23), (2.27), (2.33)) are fitted to these data points to obtain best-fit values of a and b. For convenience, this is done with Gnuplot [70] which has a preprogrammed least-squares fitting function, using the Marquardt-Levenberg algorithm to iterate to a best fit solution. Figure 4.5 shows the fitting curves used when applying this methodology to data from the full power experiment, converting experimental size distributions to cluster size distributions using constant thickness particle geometry. The reason for omitting Model 4 from this fitting is discussed later. Table 4.1(a) shows the corresponding values for a and b. Figure 4.6 and Table 4.1(b) are obtained by treating the same data but use the thinning disc particle geometry.

The values of a and b in Table 4.1 are governed by many aspects of the experimental system. The most detailed models of welding and fracture events are provided by Maurice and Courtney [48]. They state that welding is restricted by the presence of impurities (*e.g.* oxide) on the particles' surface. To

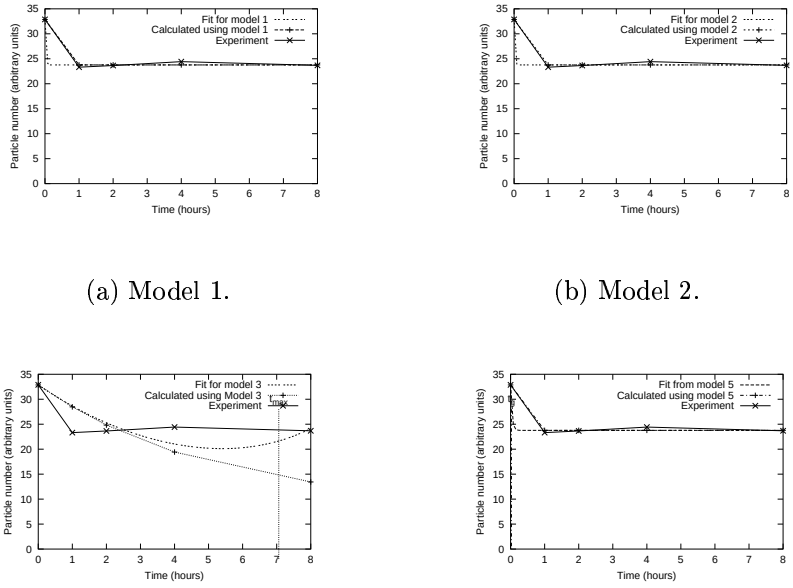

(a) Model 1.

(b) Model 2.

(c) Model 3.

(d) Model 5.

Figure 4.5: Fitting aggregation and fragmentation rate-parameters a and b to data from the full power ferro-silicon experiment. Constant thickness disc particle geometry is used.

Model	a	b
1	1.51×10^{0}	1.12×10^{1}
2	6.07×10^{-1}	3.79×10^{1}
3	1.60×10^{-3}	1.26×10^{-3}
4	8.19×10^{-4}	-1.46×10^{-2}
5	3.91×10^{-1}	5.13×10^{1}

(a) Constant thickness disc scaling.

Model	a	b
1	3.20×10^{-1}	3.40×10^{-1}
2	3.15×10^{-2}	6.84×10^{-1}
3	1.52×10^{-3}	1.80×10^{-4}
4	1.50×10^{-4}	-5.72×10^{-4}
5	6.30×10^{-2}	6.98×10^{0}

(b) Thinning disc scaling.

Table 4.1: Best fit values for a and b for each of the models 1–5 (see §2.1) as obtained by Gnuplot [70] for data from the full power experiment, presented in §3.4.1.

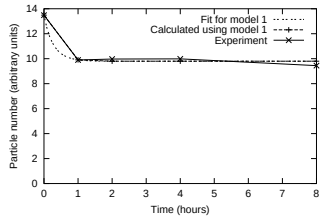

(a) Model 1, thinning disc scaling.

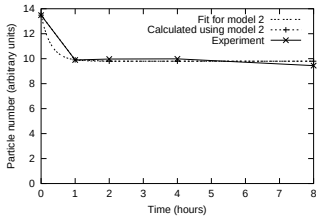

(b) Model 2, thinning disc scaling.

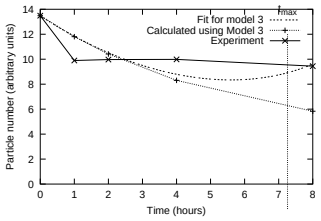

(c) Model 3, thinning disc scaling.

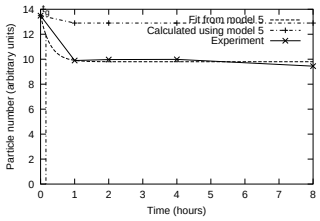

(d) Model 5, thinning disc scaling.

Figure 4.6: Fitting aggregation and fragmentation rate-parameters a and b to data from the full power ferro-silicon experiment. Thinning disc particle geometry is used.

account for this, they first calculate the amount of bare metal surface exposed through deformation as a powder particle experiences a collision. Metal-metal interfaces are assumed to bond by cold-welding. The strength of bonding at metal-to-metal contact regions is balanced against elastic recovery forces to give a welding criteria. Fracture criteria are determined similarly. The likely fracture mechanism is forging fracture, which Maurice and Courtney analyse, arriving at a fracture criteria governed by the amount of compression imparted to the powder layer during a collision (this compression is equivalent to the approach of the mill balls). These criteria relate only to one collision event, however, and are complex in themselves. The speed at which welding and fracture processes occur in the context of our model will depend on the geometry of the milling machinery, and the milling conditions (for example the kinetic energy carried by the balls in the mill).

These complex relationships make it difficult to infer welding and fracture rate-parameters directly from the experimental conditions. The fitting technique described above avoids the need to directly address this problem. Work-hardening of the powder, powder chemistry and collision geometry are accounted for without being explicitly or directly addressed. The rates we obtain are constant, so time-dependent factors, for example the hardness of the milled material, are implicitly averaged.

Model parameters, a and b, are not explicitly associated with milling parameters but it is still possible to determine how the rates are altered by changes in milling conditions. For example, the ferro-silicon experiments have been repeated with the milling velocities reduced by a factor $\sqrt{2}$. The intention was to reduce the milling intensity by a factor 2. The values of a and b obtained from this half power experiment might be expected, rather naïvely, to be one half of those for the full power experiment. Fitting the results from the half power experiment gives the values shown in Table 4.2. Corresponding

plots of experimental data and fitted curves are shown in Figure 4.11.

The comparison of these results is given later in the chapter, in §4.3. Size distributions are calculated and examined to see which model represents the experiments most accurately. The values of a and b given by that model are used to test the hypothesis that milling progresses at half the original speed when the impeller speed is reduced.

Figure 4.6 and Figure 4.5 raise some important issues with the fitting technique. Fits for model 4 are not shown because the model is not suitable for this data. The function $M_0(t)$, equation (2.27), has a leading-order finite-time singularity at $t = 1/aM_2(0)$, as discussed in §2.2.4. If the parameters are such that the singularity falls in the fitted time-range then fitting the model becomes difficult or impossible. Furthermore, if it is possible to fit model 4 to the experimental data, perhaps only using data at earlier times, the fragmentation rate parameter is negative, as shown in Table 4.1. In order to meet the fitting requirements, the model must employ "reverse-fragmentation", using a negative fragmentation rate to augment the aggregation process. The combination of kernels used by model 4 is not suitable for this application; the aggregation kernel is overwhelmed by the strong fragmentation. Since this is always found to be the case model 4 is not discussed further.

Models 3 and 5 are also difficult to fit because the solutions found for $M_0(t)$ have limited validity. Model 3 is solved using asymptotics based on small fragmentation rate, b. The solution obtained is only valid when b is small and for a finite time, $t < t_{\max}$, given by equation (2.24). If the fitted value of b is large enough that $t_{\max}$ falls inside the fitting interval then the asymptotic solution is invalid. It follows that the values of a and b obtained using this inaccurate function are invalid. Since the numerics accurately approximate the true solution to the system, they diverge from the inaccurate fitted function and the experimental results as they are calculated using inaccurate values of

a and b. A good example of this situation is shown in Figure 4.6(c), where $t_{\max}$ is clearly labelled at about 7 hours.

The aggregation kernel used in Model 5 allows gelation, as discussed in §2.2.4. The pre-gel solution, equation (2.33), is not valid after time $t_g = 1/aM_2(0)$. In both the full and half power experiments, t_g occurs very early on so the fitting is substantially affected. Figure 4.6(d) shows the numerical solution diverging significantly from the fitted solution. The effect of gelation may or may not be significant. Although the onset of the phenomena has been quantified, the strength or speed at which gelation occurs has not been considered. Figure 4.5(d) is not as badly affected by gelation, because it uses a different scaling to convert the experimental data. Different particle geometries alter the skew of the cluster distributions generated from the experimental data. The constant thickness disc scaling places less emphasis on the larger cluster sizes, as cluster size increases more quickly with sieve size, so material is spread among more cluster sizes and concentrations are lower. This reduces the aggregation rate required for the model to calculate equivalent distributions, slowing gelation. Comparing Figure 4.9 and Figure 4.10 illustrates this effect; Figure 4.10 uses the thinning disc geometry and has a higher concentration of larger particles throughout the calculation.

Finally it should be noted that the fits for the full power experiment presented in Figure 4.5 and Figure 4.6 are not as accurate as those for the half power experiment (Figure 4.11) and those in the next chapter. Our modelling technique is not ideally suited to data from the full power experiment, as changes in M_0 occur only at very early times. This reduces fitting accuracy, because the fitted curve is matched only to the initial gradient of the experimental M_0 data (which is inaccurate due to under sampling), and to the static level achieved. Measurements for shorter times would add detail to the transition region and increase fitting accuracy but such measurements are not

practical because of the 30 minute discharge cycle used during milling. Reducing the milling time significantly below 1 hour gives a sample in which some of the particles have been milled twice as long others. Later results suggest that such fitting difficulties are common to brittle powders, where most of the size change occurs early in the milling. Therefore our models may be most useful for ductile samples. This is not a severe restriction as milling is most commonly conducted with ductile metals. Our modelling efforts have been successful despite a somewhat inaccurate fit to this experiment, as the next section shows.

4.3 Calculating size distributions

A fitting process has been applied to data from the full power experiment in §3.4.1 and suitable values have been chosen for the model's rate-parameters, a and b (see Table 4.1). It is now possible to use the model to calculate full size distributions at arbitrary times. This requires the application of numerical methods. A NAG[1] routine was selected to solve the problem. It uses a variable-order, variable-step algorithm implementing the backward differentiation formulae. For the purpose of this discussion, in which the model predictions are compared to experimental measurements, the routine is configured to give output at times suitable for comparison with experimental measurements. However, the models can interpolate and extrapolate over time and provide a detailed sampling of the powder's particle size distribution.

Figure 4.7 compares measurements made during the full power ferro-silicon experiment with corresponding predictions made by the models. The calculations are made using constant thickness disc particle geometry, and use the

[1]Numerical Algorithms Group, Wilkinson House, Jordan Hill Road, Oxford, OX2 8DR, United Kingdom.

rates listed in Table 4.1(a), obtained from the fit lines in Figure 4.5. Figure 4.8 shows the equivalent data calculated using the thinning disc scaling. The data is displayed as a line plot for clarity and brevity. It is important to note, though, that only the points represent data, while the joining lines emphasise the position of the various points and provide a convenient shape that aids comparison of the models and the experiment.

First, examining figure 4.7 shows that model 5 has followed the experiment most closely over time, although it consistently over-estimates the amount of material found in the largest and smallest size fractions. Although problems with gelation were predicted, validity of the numerical solution for model 5 can be assessed by calculating values of $M_0(t)$ from the distributions produced. These values are plotted in figure 4.5, where they are labelled "Calculated using model x" with $x \in \{1, 2, 3, 5\}$. They indicate that the numerics provide a good approximation to the analytical solution. The absence of gelation can be explained by the presence of strong fragmentation in this calculation. Table 4.1(a) shows the fragmentation rate-parameter, b, is two orders of magnitude higher than a, the welding rate parameter. The gel-time calculations are leading order, assuming weak fragmentation ($b \ll 1$).

Still looking at figure 4.7, models 2 and 3 have also produced reasonably good matches to the experimental data. They consistently underestimate the amount of material in the largest and smallest size fractions, over estimating intermediate sizes. The size distribution calculated by model 3 at 8 hours is more inaccurate than the others, as the rate-parameters cannot be accurately determined for use over such long times; the limitations are imposed by the asymptotics used to calculate the leading order solution for $M_0(t)$ (see figure 4.5(c) and equation (2.23)). Model 1 is the least accurate model, showing the least correlation between predictions and experiment.

When using the thinning disc scaling to process the same data (figure 4.8)

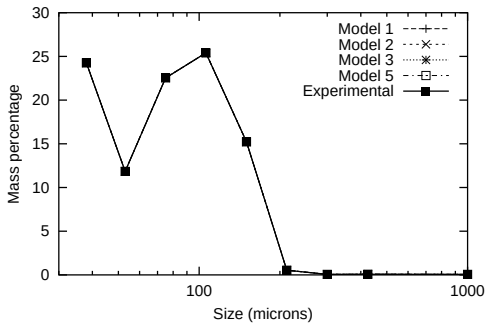

(a) Initial distribution.

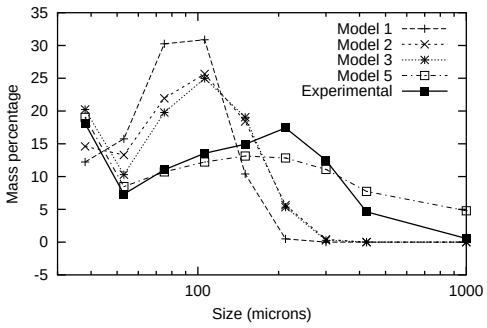

(b) 1 hour.

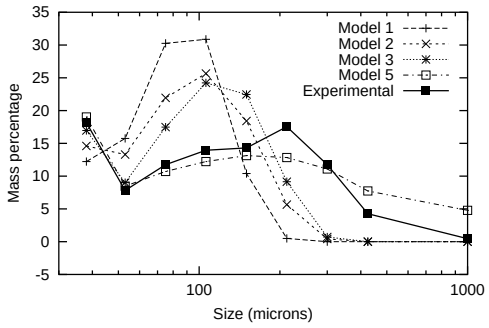

(c) 2 hours.

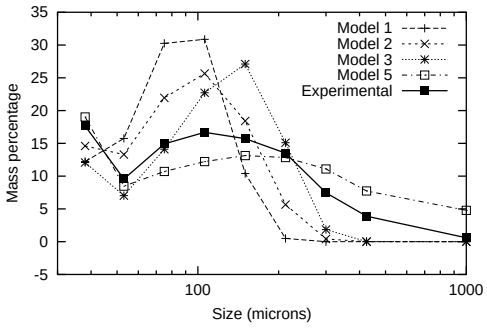

(d) 4 hours.

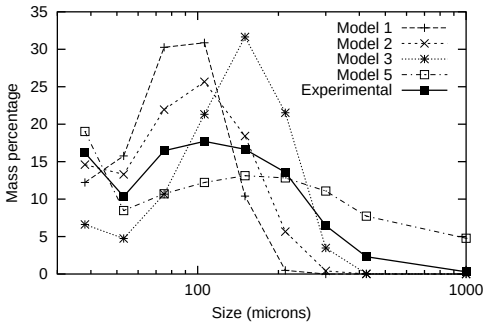

(e) 8 hours.

Figure 4.7: Sieved size distributions generated by applying the models to data from the full power experiment. Size conversions use the constant thickness disc scaling.

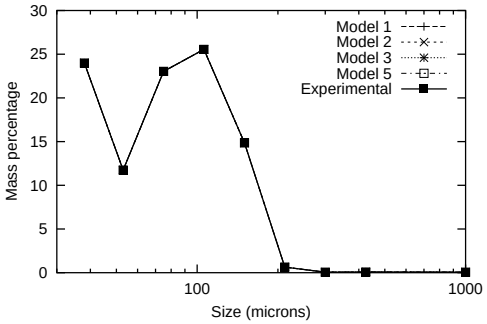

(a) Initial distribution.

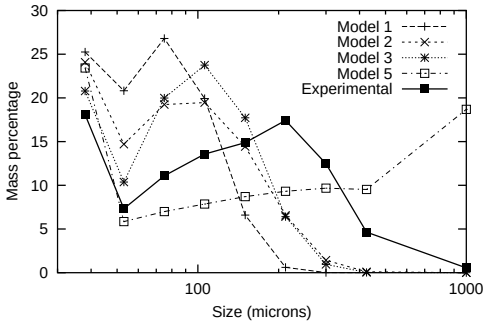

(b) 1 hour.

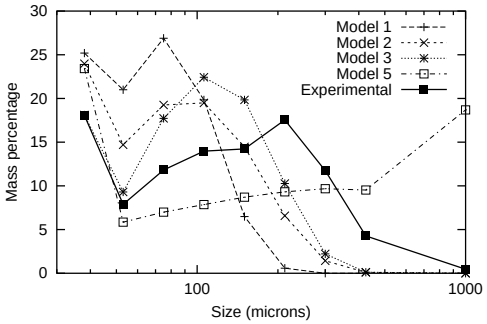

(c) 2 hours.

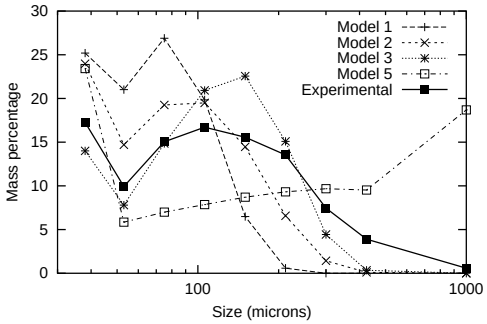

(d) 4 hours.

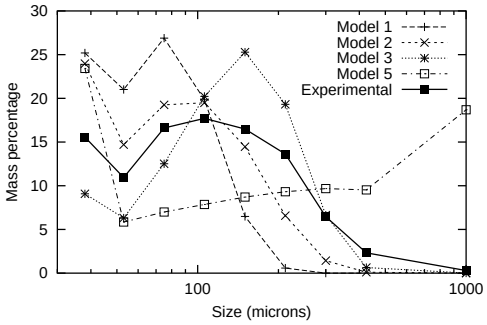

(e) 8 hours.

Figure 4.8: Sieved size distributions generated by applying the models to data from the full power experiment. Size conversions use the thinning disc scaling.

Model	a	b
1	4.97×10^{-2}	3.19×10^{-2}
2	4.23×10^{-3}	7.06×10^{-2}
3	1.02×10^{-3}	5.34×10^{-5}
4	1.22×10^{-4}	-5.26×10^{-4}
5	8.46×10^{-3}	9.26×10^{-1}

Table 4.2: Best fit values of a and b for each of the models 1–5 for the half power experiment data from §3.4.1. The thinning disc size scaling is used.

the models are, in general, better matched to the experiment. This suggests that this scaling is the better one to use. Model 5 now suffers the affects of gelation (figure 4.6(d)) as fragmentation is less prolific (Table 4.1(a)). This is a consequence of using the thinning disc scaling, as it places more emphasis on the larger cluster sizes (there are higher cluster concentrations there, see figure 4.9 and figure 4.10). In terms of accuracy, there is little to choose between models 2 and 3 at short times (2 hours and 4 hours), but model 2 is clearly better at longer times, when the asymptotics used to calculate $M_0(t)$ for model 3 become invalid. Again, model 1 is not very accurate, but it is better than model 5 in this case.

It is not clear from these plots that the models do, in fact, provide more detailed size distributions than obtained experimentally from sieved size measurements. To demonstrate this, the cluster size distributions calculated from the models are plotted in Figure 4.9 and Figure 4.10. These plots also illustrate the results of the size conversion procedure that uses experimental sieved size distributions to generate the cluster distributions shown. Finally, the figures show how the different models diverge over time.

Similar techniques have been applied to the half power experiments. It was found that the thinning disc size scaling is more appropriate, so only results

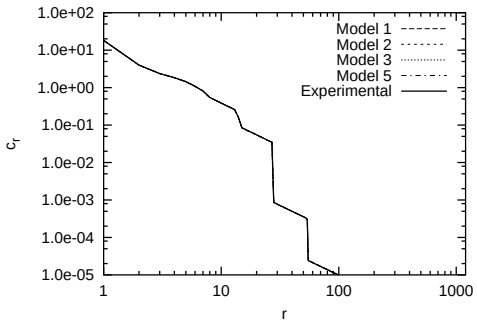

(a) Initial distribution.

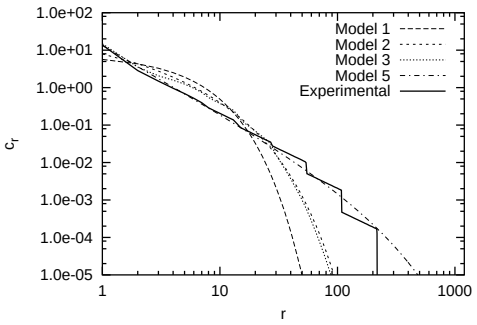

(b) 1 hour.

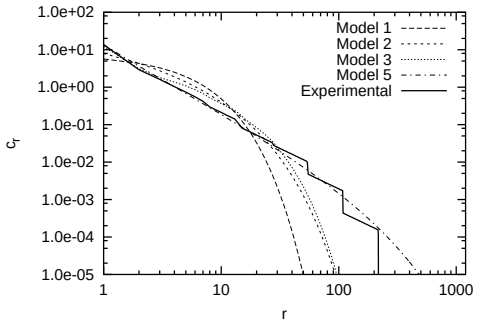

(c) 2 hours.

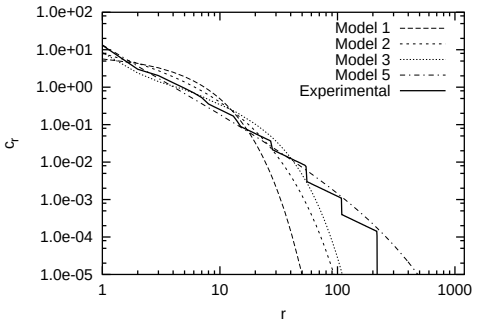

(d) 4 hours.

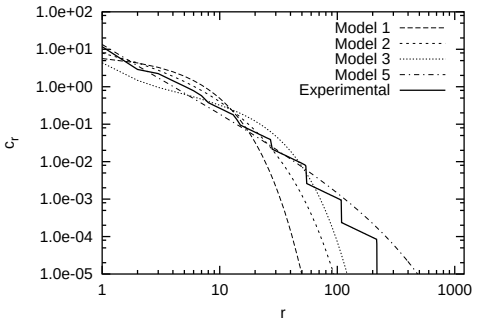

(e) 8 hours.

Figure 4.9: Cluster size distributions generated by applying the models to data from the full power experiment. Size conversions use the constant thickness disc scaling.

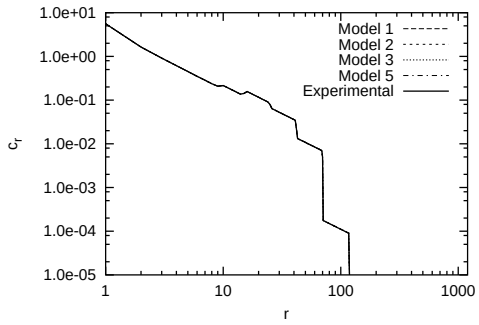

(a) Initial Distribution.

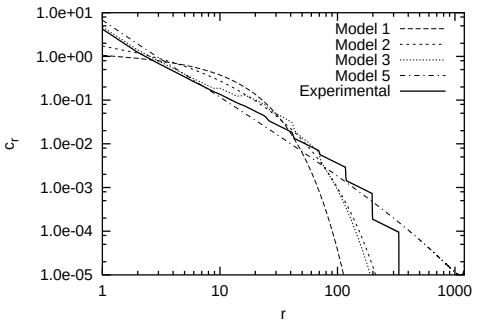

(b) 1 hour.

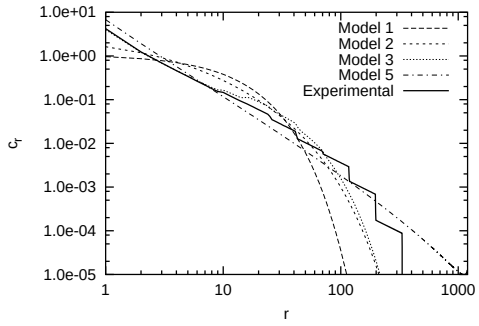

(c) 2 hours.

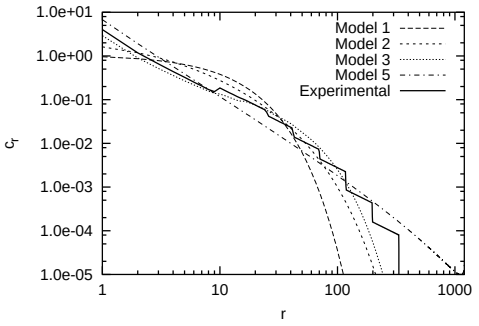

(d) 4 hours.

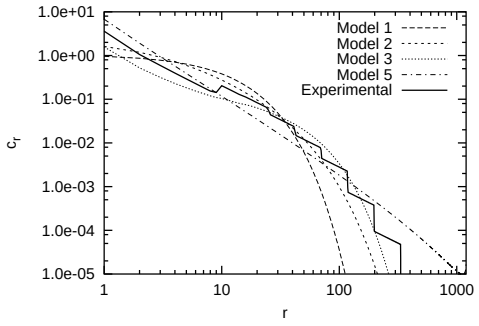

(e) 8 hours.

Figure 4.10: Cluster size distributions generated by applying the models to data from the full power experiment. Size conversions use the thinning disc scaling.

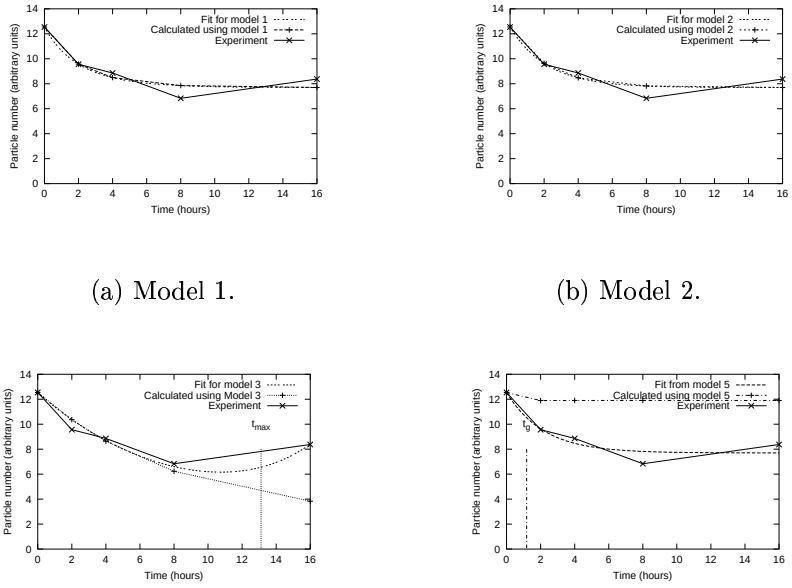

(a) Model 1.

(b) Model 2.

(c) Model 3.

(d) Model 5.

Figure 4.11: Fitting aggregation and fragmentation rate-parameters a and b to data from the half power ferro-silicon experiment. The thinning disc size scaling is used.

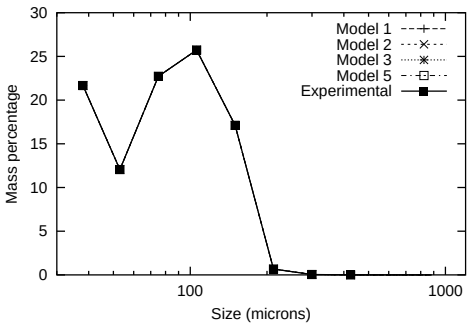

(a) Initial distribution.

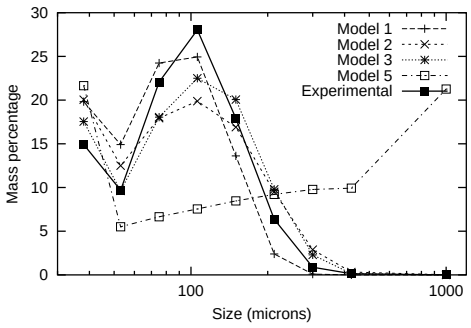

(b) 2 hours.

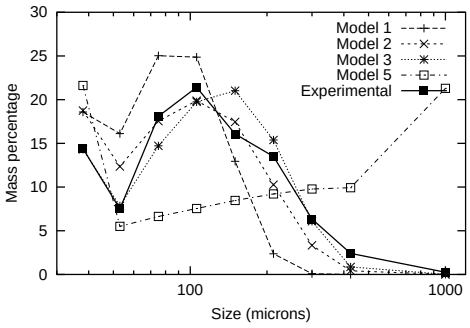

(c) 4 hours.

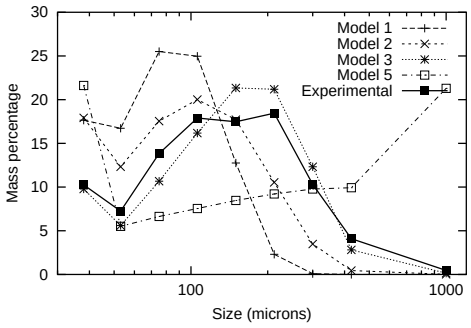

(d) 8 hours.

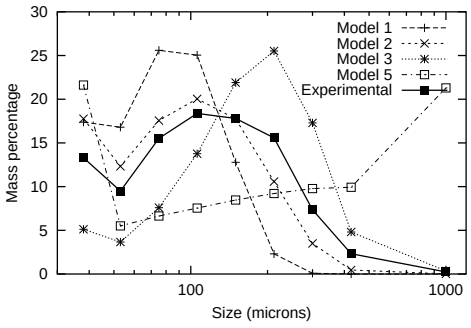

(e) 16 hours.

Figure 4.12: Sieved size distributions generated by applying the models to data from the half power experiment. Size conversions use the thinning disc scaling.

Experiment	a	b
Full power	3.15×10^{-2}	6.84×10^{-1}
Half power	4.23×10^{-3}	7.06×10^{-2}

Table 4.3: Comparing of values of a and b found for different milling speeds. The parameters are found using model 2 and the thinning disc particle geometry.

using this scaling are presented. Figure 4.11 shows the fitting procedure, giving the values of a and b shown in Table 4.2. These values have been used to generate sieved size distributions from the models, as shown in Figure 4.12. Here, models 2 and 3 are the most accurate, with model 2 probably being the most successful. Model 3 has been affected by asymptotic considerations, though. Model 5 has suffered the effects of gelation and Model 1, though well fitted, is not well suited to this data set. Overall, the results produced by model 2 closely match the experiment, as do those for model 3 in the interval $0 < t < 8$.

Since model 2 has modelled both the full and half power experiments reasonably accurately, the values of a and b found using the thinning disc scaling may be compared directly. The pertinent results from Table 4.1(b) and Table 4.2 are listed in Table 4.3 for easy comparison. These values show that aggregation progresses approximately 7.4 times faster in the full power experiment, and that fragmentation occurs nearly 9.7 times faster at the higher milling speed. This suggests the hypothesis that milling speed is proportional to the square of the mill impeller speed is false. In this case the induced change is much larger.

By applying the models to the full power and half power experiments this chapter has shown that the models are suitable for their intended purpose. Models 2 and 3 have proved the most useful in the current context, indicating

that the aggregation rate $a_{r,s} = a(r + s)$ is the most appropriate for Zoz milling ferro-silicon. The difficulty of fitting model parameters to data from the full power experiment was noted, as were more universal problems concerning models 3, 4 and 5. The half power experiment produced more easily fitted data, and the models have provided correspondingly more accurate results. Of course, all the results presented in this chapter only relate to one mill and one material. The next chapter briefly demonstrates how the models may be applied to several milling scenarios taken from the literature.

Chapter 5

Applying the Models

The outlined procedure has been used to match the models to experimental data taken from Lu *et al.* [44], Moshksar and Zebarjad [55], Huard *et al.* [33] and Aikin and Courtney [1]. In each case the experimental data is converted to volume size measure and values of a and b are determined using the fitting procedure. Size distributions are calculated and compared with those measured experimentally. Table 1.1 lists the materials and equipment used by the authors of each publication.

The models are tested against experimental results obtained using a variety of equipment and materials. Using different experimental scenarios shows that the models are widely applicable. In addition, Aikin and Courtney [1] present results obtained by treating different materials using identical milling conditions. Applying the models to each material in turn, and comparing the rate-parameters obtained demonstrates that more brittle materials have a higher fragmentation rate and lower aggregation rate than more ductile materials. Huard *et al.* [33] manufacture differently proportioned composites using identical milling conditions, and similar comparisons are made.

The following sections examine the data obtained from each of the four publications in turn. To begin with, single milling experiments are examined:

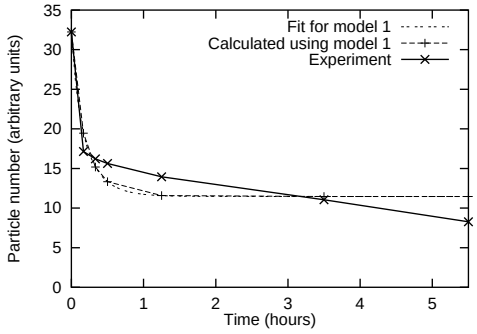

(a) Model 1.

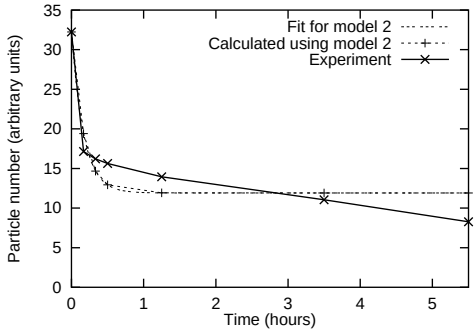

(b) Model 2.

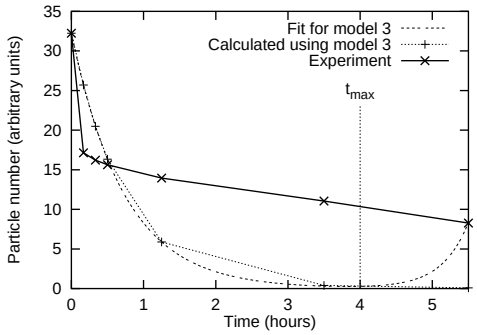

(c) Model 3.

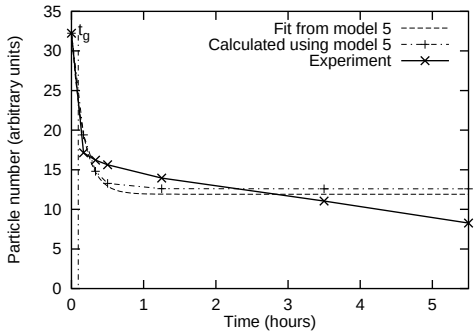

(d) Model 5.

Figure 5.1: Experimental, fitted and calculated particle totals for aluminium converted using the constant disc thickness approximation for particle shape.

data from the Al milling experiment conducted by Moshksar and Zebarjad [55] and the Al–Cu–SiC mix milled by Lu *et al.* [44] are used. Then the sets of milling experiments discussed above are examined, starting with Huard *et al.* [33] who treat Mg–SiC composites, then examining the results of Aikin and Courtney who treat elemental Cu, Ni and Cr powders.

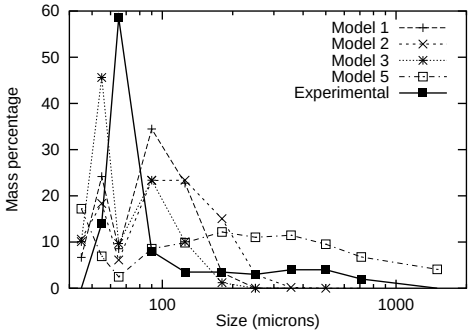

(a) 10 minutes.

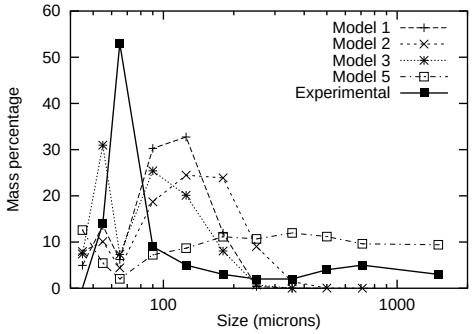

(b) 20 minutes.

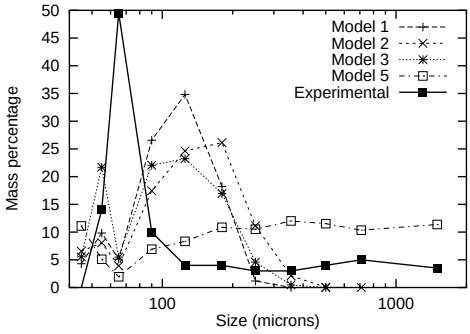

(c) 30 minutes.

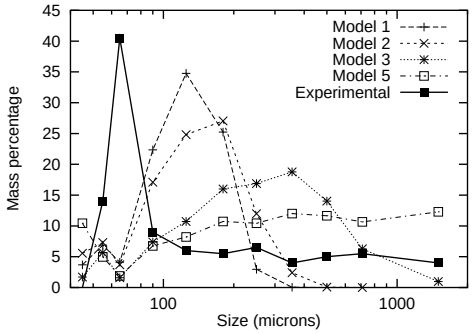

(d) 1 hour 15 minutes.

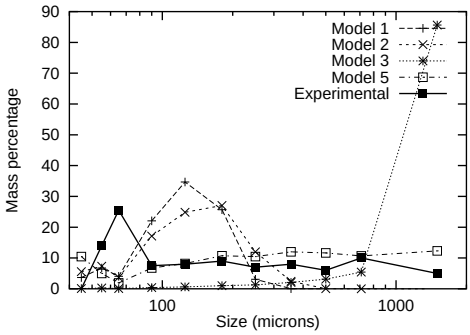

(e) 3 hours 30 minutes.

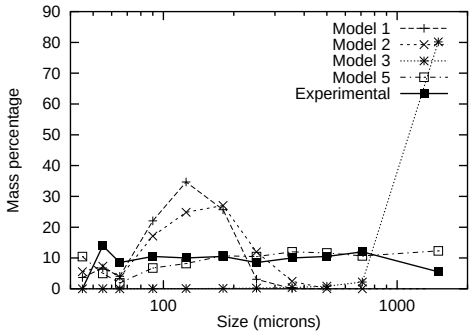

(f) 5 hours 30 minutes.

Figure 5.2: Mass distributions of aluminium calculated using the constant disc thickness approximation for particle shape.

5.1 Al in a horizontal ball mill

Moshksar and Zebarjad [55] have milled pure aluminium in a horizontal ball mill and studied how various mill parameters affect the powder evolution. They publish a detailed sieve analysis of the powder suitable for use with our models.

The parameters a and b are found as outlined in Chapter 4, using measures of particle number (average size). The lines of best fit found using the constant thickness disc scaling of particle size are shown in Figure 5.1. Models 1 and 2 show a good fit, but models 3 and 5 do not fit the data so well; the fragmentation rate for model 4 was negative. The asymptotic solution for model 3 is not valid after 4 hours, as shown in Figure 5.1(c). However, the fit routine assumes that the derived solution is accurate, and fits it through all the data points, causing large discrepancies between the average size in the model and in the experiment. Gelation has adversely affected model 5. After time t_g the truncated system of equations used to generate the numeric solution will artificially restrict the aggregation process. Although the average particle sizes match quite closely, the behaviour of the system is not representative of the underlying theory because of these restricted aggregation conditions.

The corresponding size distributions are presented as mass fractions on each experimental sieve, as shown in Figure 5.2. No model matches the data exceptionally closely. Model 3 provides a close match at early times but our approximation for M_0(t), equation (2.23), fails at large t so the resulting values for a and b are inaccurate and give poor results at later times. Model 5 does not match the data well at all. This data set highlights potential weaknesses in the fitting techniques rather than demonstrating which size dependent rates give solutions that are more accurate.

5.2 Al-Cu-SiC in a horizontal ball mill

Lu *et al.* [44] have made a dispersion strengthened composite by MA. They mill a powder mixture with nominal composition Al-4.5wt%Cu/15wt%SiC in a horizontal ball mill. The initial size distributions of their powders are not published; instead, they publish results after 1, 5, 10, 15 and 20 hours of milling. Since there is no explicit time dependence in our model the size distribution of powder milled for 1 hour has been used as an initial condition. The fit curves used to establish values of a and b together with corresponding values calculated from the numerics are shown in Figure 5.3. The constant thickness disc scaling has been used to convert particle sizes.

Figure 5.3 shows the effect of gelation on model 5 at very early times, so model 5 will be neglected. The accuracy of a and b values obtained for model 3 is restricted by the asymptotic solution. However, the calculated curve follows the experiment quite closely so inaccuracies are only expected to become significant around 15 hours. Figure 5.4 confirms this, showing the size distribution predicted by model 3 to be a reasonable fit before 15 hours. Model 2 provides a consistently good match at all times, and is therefore considered the most appropriate model for this data.

5.3 Mg with SiC particulate in low energy ball mill

Huard *et al.* [33] have milled three Mg powders, with additions of 10, 20 and 30 volume percent SiC particulates. The Mg powder had a mean diameter of 60 μm while the SiC particulates were 2 μm on average, with 90% of them smaller than 6 μm. Data for all three compositions have been analysed. Huard *et al.* [33] use a low energy horizontal ball mill similar to that used by Lu *et*

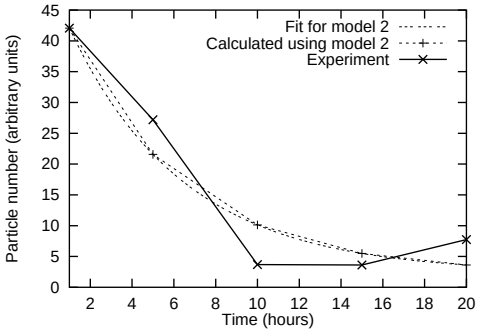

(a) Model 2.

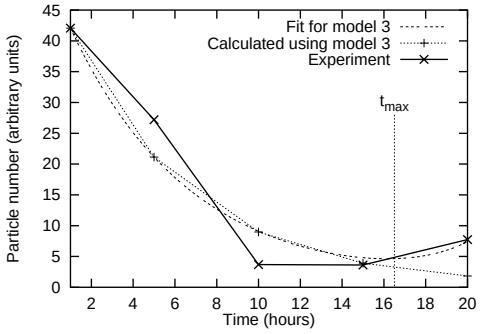

(b) Model 3.

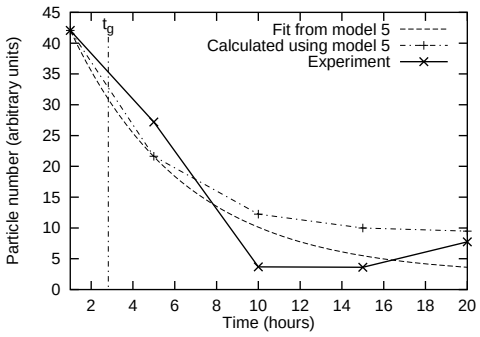

(c) Model 5.

Figure 5.3: Experimental, fitted and calculated particle totals for Al-4.5wt% Cu/15wt% SiC converted using the constant thickness disc approximation of particle shape.

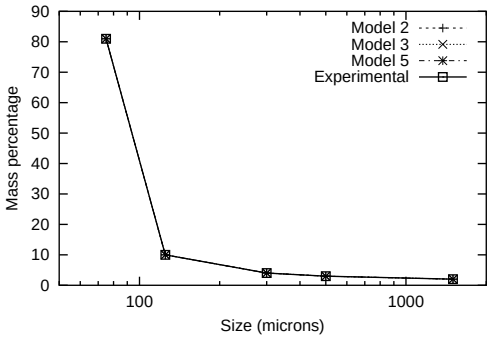

(a) 1 hour.

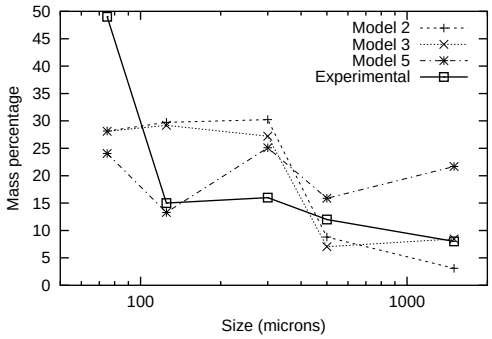

(b) 5 hours.

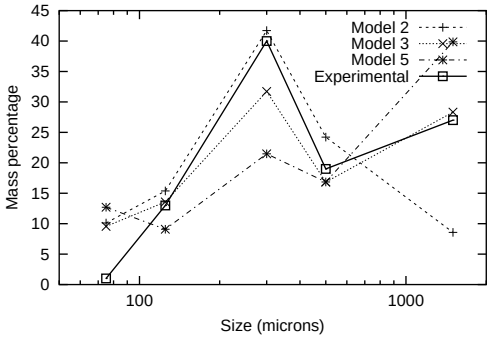

(c) 10 hours.

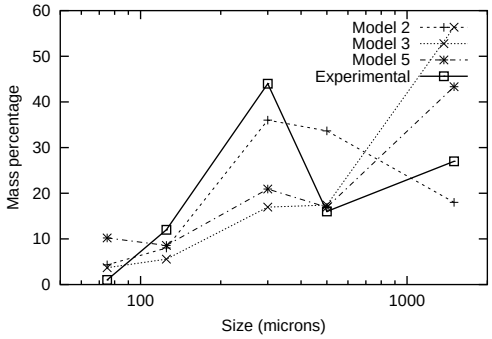

(d) 15 hours.

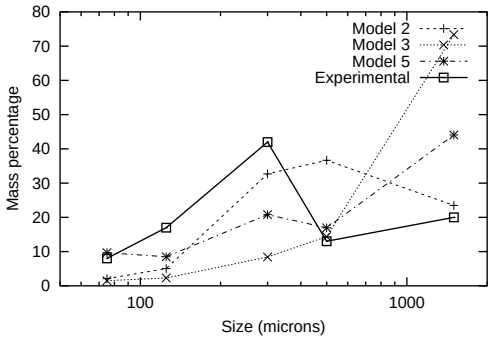

(e) 20 hours.

Figure 5.4: Mass distributions of Al-4.5wt% Cu/15wt% SiC calculated using constant thickness disc approximation of particle shape.

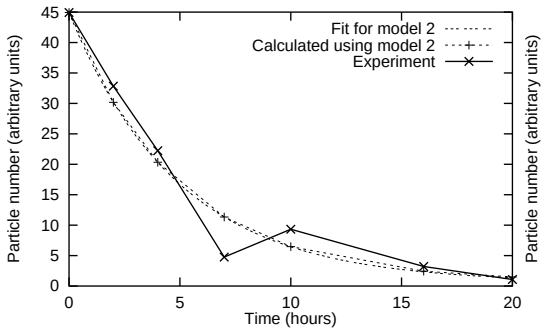

(a) Model 2.

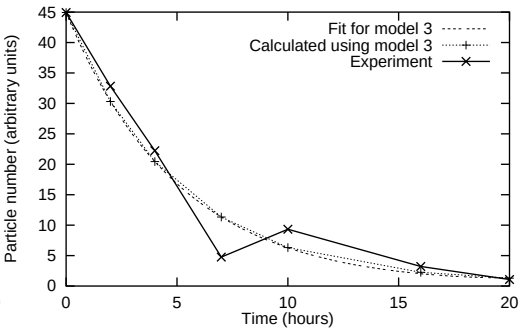

(b) Model 3.

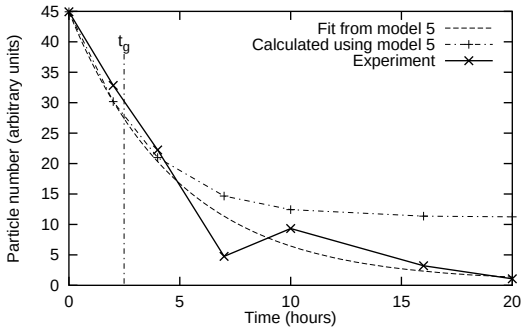

(c) Model 5.

Figure 5.5: Experimental, fitted and calculated particle totals for Mg with 20vol% SiC converted using thinning disc approximation of particle shape.

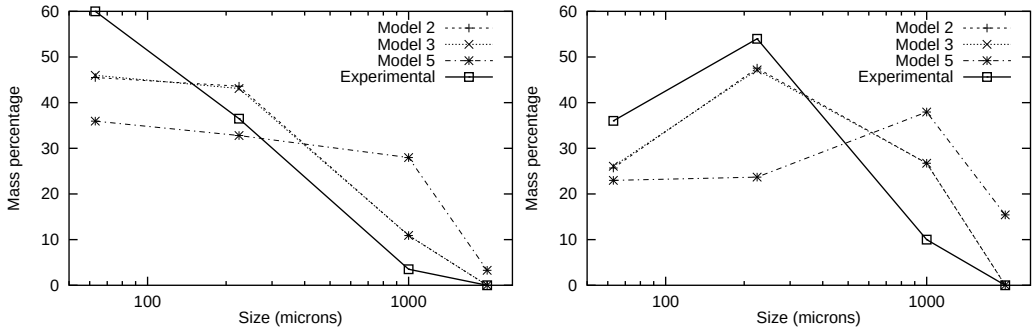

(a) 2 hours.

(b) 4 hours.

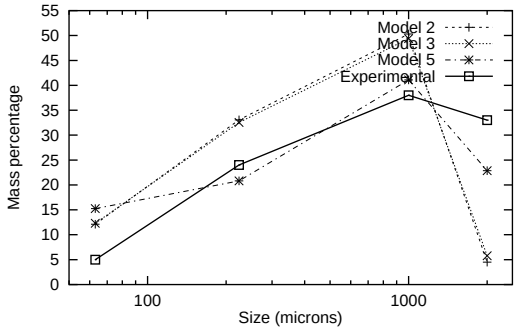

(c) 7 hours.

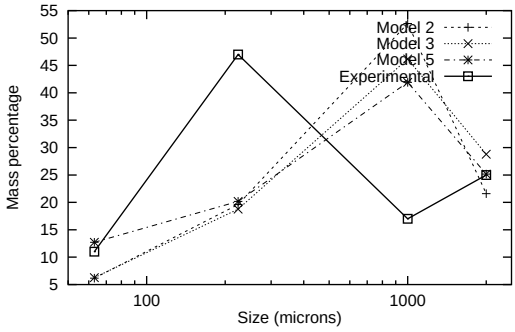

(d) 10 hours.

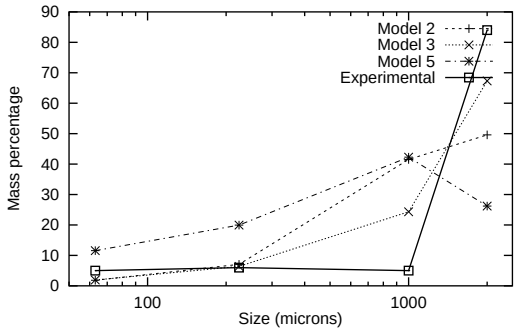

(e) 16 hours.

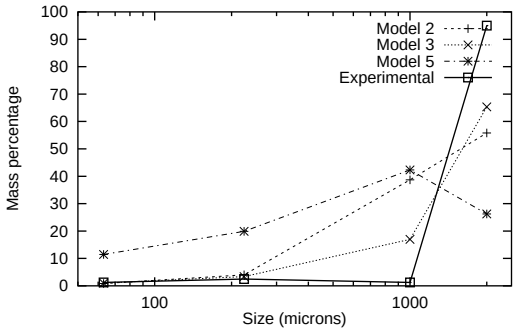

(f) 20 hours.

Figure 5.6: Mass distributions of Mg with 20vol% SiC using thinning disc approximation of particle shape.

vol%SiC	a	b
10	3.3895×10^{-3}	3.0852×10^{-9}
20	1.9673×10^{-3}	5.2343×10^{-7}
30	1.0720×10^{-3}	2.8059×10^{-4}

Table 5.1: Variation in aggregation tendency, a, and fracture tendency, b for Mg with different additions of SiC. The values have been found using model 3 with the thinning disc approximation of particle size.

al..

In our models, the material is assumed to be homogeneously mixed at the start of the experiment. The SiC particulates mix into the Mg matrix very early in the milling experiment so the errors introduced by this assumption are minimal. We have found that these approximations work well and our models can be applied to the data giving good results.

Experimental, best-fit and calculated particle number curves relating to a 20 vol% addition of SiC are shown in Figure 5.5. The corresponding particle size distributions in Figure 5.6 show that model 3 fits the data best. The other compositions have been treated similarly. The asymptotic approximation for M_0 has failed earlier with the 30 volume percent data because the fragmentation rate, b, is higher. The calculated value of M_0 increases a little too quickly, implying that the aggregation rate is too high and/or the fragmentation rate is too low. Consequently, small errors are incurred in this data set at later times.

Since model 3 fits the data most closely, values of a and b are presented in Table 5.1. Huard *et al.* do not alter their milling conditions, so the observed variations in aggregation rate parameter, a, and fragmentation rate parameter, b, are due to differences in the milled material.

Table 5.1 shows a gradual decrease in the aggregation rate parameter, a

with increasing SiC content. The cold welding process relies on clean metal-metal contact between powder particles. The concentration of SiC particulates caught between compressed metallic particles will be greater for the higher addition mixtures, reducing their tendency to weld or aggregate. Agglomerates are more likely to form in the higher addition mixtures rather than strong cold-welded particles. Subsequent fragmentation of agglomerates will be easier and more frequent, giving one explanation for the higher fragmentation rate parameter. Also, high particulate additions will pin dislocations, hardening the powder, reducing ductility, and making the particles more brittle. This is particularly true for the 30 vol% mixture, which will be almost saturated with SiC particles and will contain a semi-contiguous network of SiC additions bound by small isolated pockets of metallic material. The sharp increase in the fragmentation rate parameter, b, with SiC content may be attributed to these two mechanisms.

Huard *et al.* measure one particularly interesting quantity, a powder output ratio that indicates the amount of powder cold welded to the components of the mill. It is interesting to note that the gelation times found for model 5 correlate with times during the experimental procedure when significant amounts of material cold weld to the mill. The numerical calculations for model 5 are inaccurate because gelation affects are not correctly incorporated. Accurate values for a and b may be obtained before gelation occurs, but these values are not suitable for post gelation calculations. The obtained values are of the correct order, and development of more accurate matching techniques may allow model 5 to predict the loss of material stuck to the mill.

5.4 Analysis of data published by Aikin and Courtney

Aikin and Courtney have milled copper, niobium and chromium powders in a vertical attritor. The media collisions in this type of mill have higher energies than those in the horizontal mills used in the other experiments. The fitting procedure conducted on the copper data using the thinning disc approximation of particle size is shown in Figure 5.7.

For copper, model 3 will not predict the experimental size distribution measured after 16 hours of milling. Model 5 will not give a good match because of gelation affects, but may be able to predict the size distribution after 1 hour of milling, before t_g is reached.

Figure 5.8 shows the corresponding size distributions. If all the times shown are considered, model 2 provides the best match. However, model 3 provides a better match to the data collected up to 8 hours of milling. This is probably because the average size in model 3 is closer to that measured experimentally for early times (Figure 5.7(c)). Experimental and predicted size distributions for Cu are shown in Figure 5.8. Model 5 matches the results for 1 hour well, but calculations at further times are numerically inaccurate because of the truncation used. Models 2 and 3 show a close match at all times.

The matches for niobium are similar to those for copper shown. The chromium experiment is more difficult to model because the average size of the powder oscillates about a mean value (Figure 5.9). Models for this data do not show a large variation in particle size distribution over time, and should not be considered as accurate as those for niobium and copper.

Aikin and Courtney have used identical milling conditions for the three powders, so changes in the rate parameters a and b are caused by differences in the powder material. The three powders are very different in nature. Copper

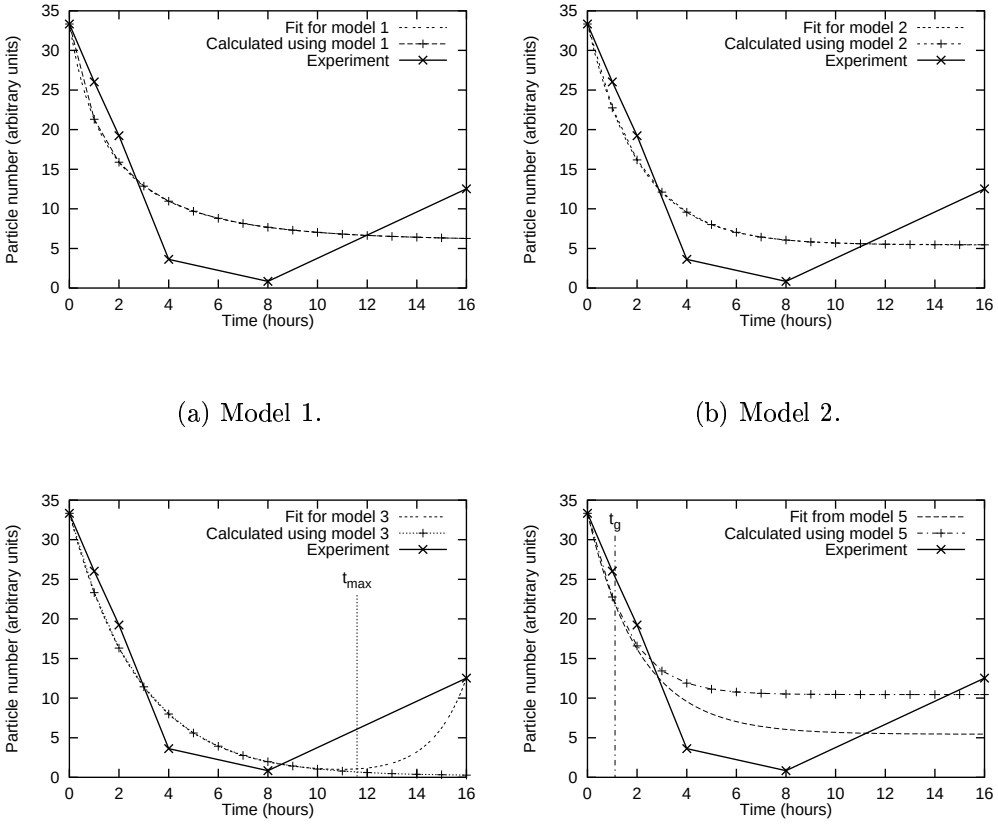

(a) Model 1.

(b) Model 2.

(c) Model 3.

(d) Model 5.

Figure 5.7: Experimental, fitted and calculated particle totals for copper converted using thinning disc approximation of particle shape.

Material	a	b
Copper	4.5095×10^{-3}	5.1878×10^{-2}
Niobium	1.9689×10^{-3}	1.1427×10^{-2}
Chromium	1.4427×10^{-1}	8.9882×10^{0}

Table 5.2: Variation in aggregation tendency, a, and fracture tendency, b for different materials. The values have been found using model 2 with the thinning disc approximation of particle size.

is soft and would be expected to aggregate readily, chromium is a fairly brittle material at room temperature, and may be expected to fragment readily and niobium will fall somewhere between the two extremes.

The values of aggregation and fragmentation rate parameters used with model 2 are listed in Table 5.2. Results for copper and niobium reflect the expected trends, having aggregation and fragmentation rate parameters of similar order. Copper is milled more quickly than niobium, with aggregation and fragmentation occurring more frequently. The rate parameters suggest that chromium mills two orders of magnitude faster than the other two powders. The size evolution of chromium is significantly different to that of copper and niobium, possibly due to the BCC structure of chromium making it brittle and giving it a significantly greater increase in work-hardening, which our model cannot take account of.

5.5 Summary of one-component modelling

The one-component models have proved successful. While there are problems associated with asymptotic solutions and gelation effects, either model 2 or model 3 offers reasonable agreement with experimental data in all the scenarios studied. This suggests that the aggregation rate $a_{r,s} = a(r + s)$ is the most

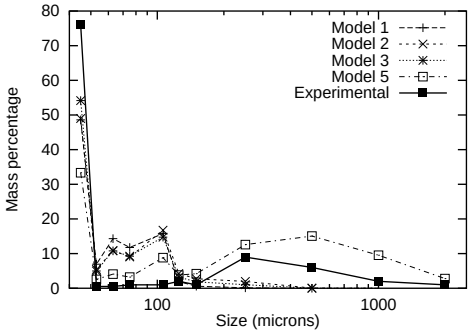

(a) 1 hours.

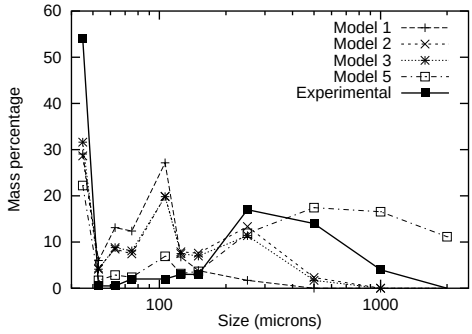

(b) 2 hours.

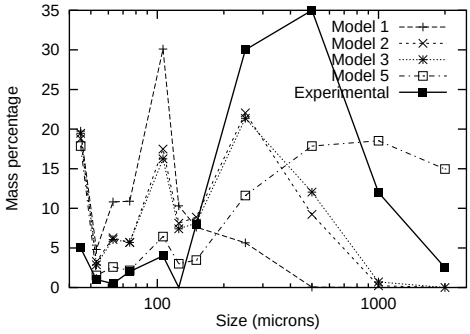

(c) 4 hours.

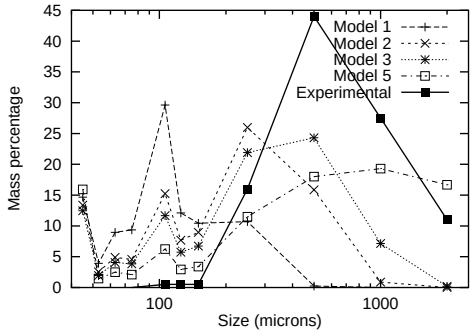

(d) 8 hours.

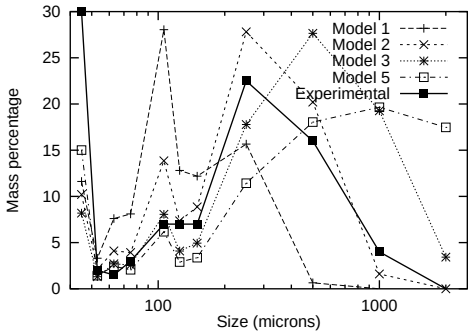

(e) 16 hours.

Figure 5.8: Mass distributions for copper using thinning disc approximation of particle shape.

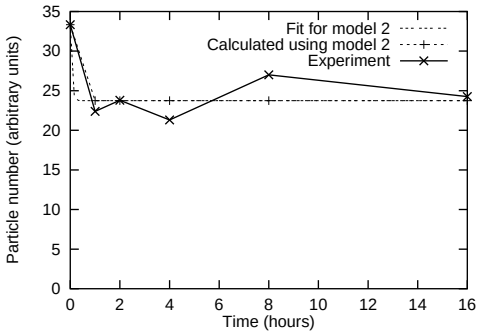

Figure 5.9: Experimental particle totals from Aikin and Courtney's chromium experiment [2] plotted alongside fitted and calculated particle totals from model 2 using the thinning disc approximation of particle shape.

realistic of those tested. Since the chance of a particle experiencing a collision is proportional to its volume, this indicates that, when involved in a collision, larger particles are less likely to aggregate than smaller particles.

It is difficult to determine which fragmentation rate is most appropriate. Model 3 has not been accurately applied to situations of strong fragmentation because the asymptotic methods used to obtain an expression for $M_{0,0}(t)$ assume that $b \ll 1$. It is also possible that different materials are accurately modelled by different fragmentation rates.

Model 2 has the most advantageous combination of properties, as the size dependent rates used are adequate for all the experiments examined and allow an exact solution for $M_{0,0}(t)$ to be obtained. Part II of this thesis presents models that predict mixing phenomena as well as changes in size distribution. These models generalise models 1 and 2 to consider clusters that contain two types of volume element. The two types of element represent different materials so the composition of each particle is known. Model 1 is studied as it is the most mathematically simple case and model 2 is studied as it has proved most useful in the one-component study. The methods of size conversion (§4.1) and

fitting (§4.2) developed for these one-component models are also generalised so that the two-component mixing models can be tested against experimental measurements.

Part II

Two Component Systems

Chapter 6

Modelling Theory

A generalisation of Smoluchowski's coagulation fragmentation model is proposed, where each cluster contains two different types of volume element. Composite mixing is modelled by using the different types of volume element to represent different materials. The discussion refers to elements of material A (type A elements) and elements of material (or type) B. A cluster containing r elements of material A and s elements of material B is denoted $C_{r,s}$. The concentration of such clusters is written $c_{r,s}$. Elements of material A and material B need not occupy the same amount of volume, so a cluster $C_{r,s}$ has volume $rV_A + sV_B$, where V_A is the size of a volume element of material A and V_B is similarly defined for material B.

The generalised Smoluchowski model allows mixing to occur between two different powders as a consequence of welding and fragmentation events. Mechanical alloying can be modelled by choosing initial conditions so that clusters contain only type A or type B elements. Mixing occurs when a type A cluster welds with a type B cluster. Subsequent fragmentation is unlikely to separate the two materials perfectly so, after adequate repetition, the two materials become evenly dispersed. Figure 6.1 illustrates how mixing occurs as a consequence of welding and fragmentation events.

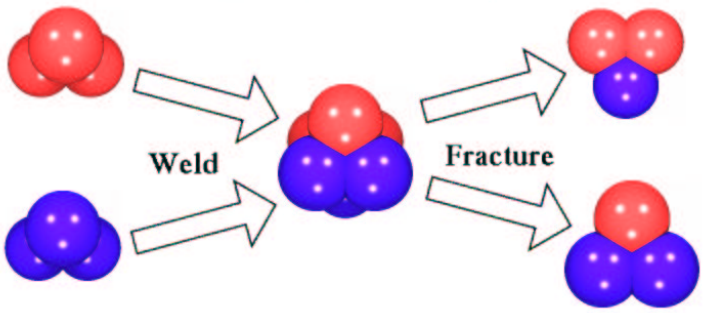

Figure 6.1: Cluster composition is altered as particles weld and fracture.

Of course, the size distribution of the powder particles will also be altered as mixing takes place. Fitting methods similar to those presented in §4.2 can be used with this two-component case to determine the model's parameters. The mixing information obtained form the two component model supplements the size predictions that have already been demonstrated. The variance in particle composition indicates the degree of mixing in the system, a measurement that has proved elusive in the past. The model is limited, though, by its inability to predict chemical interactions within a powder particle. Accuracy is lost if milling progresses beyond the early stages and small-scale processes such as chemical reactions become important. This is especially true when these processes radically alter the mechanical properties the material, affecting welding and fracture frequencies.

The following sections describe a modelling procedure that parallels the one-component model presented in Part I. The generalisation of Smoluchowski's equations is described in the next section. Then kernels are chosen for aggregation and fragmentation rates that depend on both the size and composition of the particles involved. With these dependencies specified, it is possible to obtain an analytic expression for the number of clusters present in the model at any time, t. The next chapter describes the fitting techniques used to de-

termine model parameters. Model predictions of particle size and composition found using these parameters are compared to experimental measurements of particle size taken from the literature. The success of the models is therefore assessed, and finally an improved model is proposed. The next section begins this analysis by introducing the generalised Smoluchowski model.

6.1 Generalising Smoluchowski's equations to two-component systems

The welding and fragmentation processes shown in Figure 6.1 may be written, respectively,

$$C_{j,k} + C_{r.s} \xrightarrow{a_{j,k,r,s}} C_{j+r,s+k}, \tag{6.1}$$

$$C_{j+r,s+k} \xrightarrow{b_{j,k,r,s}} C_{j,k} + C_{r.s}, \tag{6.2}$$

for general particle size and composition. These reaction equations are analogous to the one-component forms given in equations (1.2) and (1.3). Note, in particular, that the two-component reaction equations conserve volume and that the welding rate depends on both the size and composition of the welding particles while the fracture rate depends on the make up of the fragmented pieces.

As with one component systems, one cluster size, $C_{r,s}$, is examined closely to determine modes in which (r, s)-clusters are gained and lost. The same four mechanisms operate on clusters of size (r, s) as were listed for the one-component clusters C_r:

- gain by welding, $C_{j,k} + C_{r-j,s-k} \xrightarrow{a_{j,k,r-j,s-k}} C_{r,s}$,
- loss by fragmentation, $C_{r,s} \xrightarrow{b_{j,k,r-j,s-k}} C_{j,k} + C_{r-j,s-k}$
- loss by welding, $C_{j,k} + C_{r,s} \xrightarrow{a_{j,k,r,s}} C_{r+j,s+k}$,

- gain by fragmentation, $C_{r+j,s+k} \xrightarrow{b_{j,k,r,s}} C_{j,k} + C_{r,s}$.

Each reaction contributes to the change (over time) in the concentration of (r,s)-clusters, $\dot{c}_{r,s}$. First order reaction kinetics are applied, as before, to evaluate the magnitude of each contribution. The first two processes describe how an (r,s)-cluster interacts with clusters of smaller size, $C_{j,k}$ and $C_{r-j,s-k}$, where $j < r$ and $k < s$. To obtain the total gain by welding and total loss by fragmentation all possible values of j and k are considered, giving the following terms:

- gain by welding, $\frac{1}{2}\sum_{j=0}^{r}\sum_{k=0}^{s}{}' a_{j,k,r-j,s-k}\, c_{j,k}\, c_{r-j,s-k}$,
- loss by fragmentation, $\frac{1}{2}\sum_{j=0}^{r}\sum_{k=0}^{s}{}' b_{j,k,r-j,s-k}\, c_{r,s}$.

The primed double-summation denotes summation over all but the first and last terms; that is those where the indices are simultaneously maximal or minimal (in this case the excluded terms are those where $j = k = 0$ and $j = r$, $k = s$). The omitted terms correspond to reactions that would concern $(0,0)$-clusters, that is, clusters with no volume. The factor $1/2$ is included because each combination of clusters will be counted twice.

The remaining processes, loss by welding and gain by fragmentation, describe interactions between (r,s)-clusters and clusters of any size. The corresponding contributions to the change in concentration of (r,s)-clusters are therefore

- loss by welding, $\sum_{j=0}^{\infty}\sum_{k=0}^{\infty}{}' a_{j,k,r,s} c_{j,k} c_{r,s}$,
- gain by fragmentation, $\sum_{j=0}^{\infty}\sum_{k=0}^{\infty}{}' b_{j,k,r,s} c_{r+j,s+k}$.

Combining all these terms gives the generalised Smoluchowski system

$$\begin{aligned}\frac{\mathrm{d}c_{r,s}}{\mathrm{d}t} =& \frac{1}{2}\sum_{j=0}^{r}\sum_{k=0}^{s}{}' \left(a_{j,k,r-j,s-k}\, c_{j,k}\, c_{r-j,s-k} - b_{j,k,r-j,s-k}\, c_{r,s}\right) \\ &- \sum_{j=0}^{\infty}\sum_{k=0}^{\infty}{}' \left(a_{j,k,r,s}\, c_{j,k}\, c_{r,s} - b_{j,k,r,s}\, c_{r+j,s+k}\right).\end{aligned} \tag{6.3}$$

When the one-component system was studied, the cluster size distribution was characterised by moments, $M_p(t)$. Similar moments, $M_{p,q}(t)$, can be defined for the two component system,

$$M_{p,q}(t) = \sum_{r=0}^{\infty} {\sum_{s=0}^{\infty}}' r^p s^q c_{r,s}(t). \tag{6.4}$$

These moments are doubly useful, as they contain information about both cluster size and composition. Noteworthy cases include $M_{0,0}$, $M_{0,1}$, $M_{1,0}$ and $M_{1,1}$. $M_{0,0}$ represents the total concentration of clusters (of all sizes) in the system. A low value of $M_{0,0}$ indicates large average particle size, and *vice versa*. The quantity $M_{1,0}$ denotes the number of volume elements of material A in the system, while $M_{0,1}$ is the equivalent quantity for material B. Both $M_{1,0}$ and $M_{0,1}$ are conserved over time, as our model does not allow the material in the mill to react or convert from one form to the other. The quantity $M_{1,1}$ indicates the level of mixing within the mill. If all the clusters are elemental then the powder may be regarded as two separate one-component distributions:

$$c_{r,s} = \begin{cases} c_r^{(A)}, & s = 0, \\ c_s^{(B)}, & r = 0, \\ 0, & \text{both } r \text{ and } s \text{ non-zero.} \end{cases} \tag{6.5}$$

Hence $M_{1,1} = 0$ for this unmixed distribution.

The highest values of $M_{1,1}$ are attained when high values of the product rs coincide with high concentrations of particles. The factor rs is influenced by two effects: larger particles and well mixed particles have higher rs values. It is possible to remove some size dependence and obtain a better mixing measure by using the non-dimensional construct

$$\phi = \frac{M_{1,1} M_{0,0}}{M_{1,0} M_{0,1}}. \tag{6.6}$$

Note that $M_{0,0}$ will fall as the average particle size increases, while $M_{1,1}$ will rise. The denominator is constant throughout milling.

In the remainder of this chapter we study equation (6.3). The next section introduces some kernel forms, $a_{j,k,r,s}$ and $b_{j,k,r,s}$, that have particular physical significance. Then, using these particular kernel combinations, solutions are found for $M_{0,0}(t)$. The solutions are used to determine model parameters that match experimental data. The two-component modelling process is more fruitful than the one-component case because simple sieved size measurements allow predictions of both particle composition and the degree of mixing to be made. Mixing and composition are not easily measured experimentally.

6.2 Choosing kernel forms

This section identifies kernel forms which model the mechanical alloying process. As with one component systems, the likelihood of welding and fracture events is expected to depend primarily on the size and composition of the particles involved. The rate at which (r, s)-clusters weld with (j, k)-clusters depends on r, s, j and k, or equivalently the particle sizes, $(V_A r + V_B s)$ and $(V_A j + V_B k)$, and particle compositions, $(V_A r)/(V_B s)$ and $(V_A j)/(V_B k)$.

Particle size dependencies are treated as in Part I, while composition adds extra complexity. The model still can not account for changes in powder properties that affect welding and fracture processes as milling progresses. Such pertinent changes include work-hardening effects and chemical changes occurring within the powder particles. It is hoped that these effects are secondary. The studies in Part I show that one-component modelling is successful without accounting for work-hardening. The rate at which reactions occur and the consequent effects on powder properties will depend on the chemistry of the powders being milled. However, it is common for composites to form during the early stages of milling, as observed by Benjamin and Volin [9] (see Figure 1.2). Our models can predict the formation of composites and give some mea-

sure of the increasing intimacy of mixing within particles. It may be possible to predict when significant chemical changes will occur by using a measure such as ϕ (equation (6.6)) to measure the intimacy of mixing. For example the onset of reaction phenomena in the mill may be predicted and measures of the intimacy of mixing may be used to design highly reactive powders suitable for SHS reactions [42].

The simplest possible kernels, $a_{r,s,j,k} = a$ and $b_{r,s,j,k} = b$, are used by the first model. These kernels have no dependency on particle size or composition, and are analogous to model 1 in the one-component study (see §2.1). This simple case is a convenient first approximation, but model 1 was not the most accurate one-component model. This generalisation is not expected to be particularly accurate but will serve as an instructive example. The second choice of aggregation kernel is influenced by the findings of the one-component study. The most useful single component aggregation kernel was found to be $a_{r,s} = a(r+s)$ which is generalised to two-component systems, giving

$$a_{r,s,j,k} = \hat{a}(j+r) + \bar{a}(s+k). \tag{6.7}$$

This rate is both size and composition dependent. To understand the significance of the aggregation rate-parameters, $\hat{a}$ and $\bar{a}$, consider an initial cluster distribution where there are no material A volume elements:

$$c_{r,s}(0) = \begin{cases} c_s, & r = 0, \\ 0, & r > 0. \end{cases} \tag{6.8}$$

Using this distribution, the system reduces to a one-component system, with a welding rate $\bar{a}(s+k)$. Similarly, the distribution

$$c_{r,s}(0) = \begin{cases} c_r, & s = 0, \\ 0, & s > 0, \end{cases} \tag{6.9}$$

Model	$a_{r,s,j,k}$	$b_{r,s,j,k}$
1	a	b
2	$\hat{a}(r+j)+\bar{a}(s+k)$	b

Table 6.1: Aggregation and fragmentation rates used by models 1 and 2. In both cases a and b are constant rate-parameters to be determined.

produces a one component system with welding rate $\hat{a}(j+r)$. This demonstrates that, in the absence of intermixing, $\bar{a}$ is the welding rate-parameter for material B and $\hat{a}$ is the welding rate-parameter for material A.

By summing the two rates, welding events involving only material A or material B are properly modelled. Intermixing is also allowed. When a type A cluster, $C_{r,0}$, welds with a type B cluster, $C_{0,k}$, the corresponding rate would be $\hat{a}r+\bar{a}k$ (since $s=j=0$). If material A welds more easily than material B then $\hat{a}$ will be higher than $\bar{a}$. Welding events where r is large relative to k will occur more frequently than instances where k is larger than r. In general the two particles will not be pure. The welding rate will depend on the ease with which the materials weld with themselves, and on the aggregate quantities of material involved. More material A, in this case, increases the likelihood of welding, as would be expected.

Table 6.1 summarises the rates that will be used in models 1 and 2. So far, the only fragmentation rate considered, $b_{r,s,j,k}=b$, is independent of particle size and composition. The next section analyses these kernel combinations to find analytic expressions for $M_{0,0}(t)$. The solutions found are used in Chapter 7 to determine the model's parameters, a, $\hat{a}$, $\bar{a}$ and b.

6.3 Analysis of the model

As with the one-component model, it is possible to determine analytic expressions for $M_{0,0}(t)$ to fit against experimental data. The aggregation and fragmentation rate-parameters a and b (Model 1) or $\bar{a}$, $\hat{a}$ and b (Model 2) are determined by the fitting process. First, the general model is manipulated to a more convenient form, then kernel-specific analyses are conducted for each model.

6.3.1 Kernel independent analysis

The two component Smoluchowski equation, equation (6.3), can be written

$$\dot{c}_{r,s} = \frac{1}{2}\sum_{j=0}^{r}\sum_{k=0}^{s}{}' w_{j,k,r-j,s-k} - \sum_{j=0}^{\infty}\sum_{k=0}^{\infty}{}' w_{j,k,r,s} \tag{6.10}$$

where

$$w_{j,k,r,s} = a_{j,k,r,s}c_{j,k}c_{r,s} - b_{j,k,r,s}c_{j+r,k+s}. \tag{6.11}$$

The analysis of this equation is simplified by the introduction of a generating function

$$C(x,y,t) = \sum_{r=0}^{\infty}\sum_{s=0}^{\infty}{}' c_{r,s}(t)e^{-(rx+sy)}, \tag{6.12}$$

so that

$$\begin{aligned}\frac{\partial C(x,y,t)}{\partial t} = &\frac{1}{2}\sum_{r=0}^{\infty}\sum_{s=0}^{\infty}{}'\sum_{j=0}^{r}\sum_{k=0}^{s}{}' e^{-(rx+sy)}w_{j,k,r-j,s-k}c_{j,k}c_{r-j,s-k} \\ &-\sum_{r=0}^{\infty}\sum_{s=0}^{\infty}{}'\sum_{j=0}^{\infty}\sum_{k=0}^{\infty}{}' e^{-(rx+sy)}w_{j,k,r,s},\end{aligned} \tag{6.13}$$

This approach is an extension of that presented by Davies [14] in her analysis of one-component systems. The generating function is useful because taking the limit of equation (6.13) as $x \to 0$ and $y \to 0$ gives a differential equation for $M_{0,0}(t)$.

Equation (6.13) is simplified by manipulating the first of the two summation terms. Taking the first summation and re-ordering the summation pairs j-r and s-k, then applying transformations $r' = r - j$ and $s' = s - k$ gives

$$\frac{1}{2}\sum_{r=0}^{\infty}\sum_{s=0}^{\infty}{}'\sum_{j=0}^{\infty}\sum_{k=0}^{\infty}{}' e^{-((r+j)x+(s+k)y)} w_{j,k,r,s}. \tag{6.14}$$

The two summation terms are combined to give

$$\frac{\partial C(x,y,t)}{\partial t} = \frac{1}{2}\sum_{r=0}^{\infty}\sum_{s=0}^{\infty}{}'\sum_{j=0}^{\infty}\sum_{k=0}^{\infty}{}' \left(e^{-(jx+ky)} - 2\right) e^{-(rx+sy)} w_{j,k,r,s}. \tag{6.15}$$

Then substituting for $w_{j,k,r,s}$ allows the expression to be split into aggregation and fragmentation components:

$$\frac{\partial C(x,y,t)}{\partial t} = A(x,y,t) - B(x,y,t) \tag{6.16}$$

$$A(x,y,t) = \frac{1}{2}\sum_{r=0}^{\infty}\sum_{s=0}^{\infty}{}' c_{r,s} e^{-(rx+sy)} \sum_{j=0}^{\infty}\sum_{k=0}^{\infty}{}' a_{j,k,r,s} c_{j,k} \left(e^{-(jx+ky)} - 2\right) \tag{6.17}$$

$$B(x,y,t) = \frac{1}{2}\sum_{r=0}^{\infty}\sum_{s=0}^{\infty}{}' e^{-(rx+sy)} \sum_{j=0}^{\infty}\sum_{k=0}^{\infty}{}' b_{j,k,r,s} c_{r+j,s+k} \left(e^{-(jx+ky)} - 2\right) \tag{6.18}$$

$B(x,y,t)$ can be expressed in a more useful form by reversing the transformations and changing the summation orders again, giving

$$B(x,y,t) = \frac{1}{2}\sum_{r=0}^{\infty}\sum_{s=0}^{\infty}{}' c_{r,s} e^{-(rx+sy)} \sum_{j=0}^{r}\sum_{k=0}^{s}{}' b_{j,k,r-j,s-k} \left(1 - 2e^{(jx+ky)}\right). \tag{6.19}$$

Note that these manipulations are applied to a combined sum representing both summation terms in Equation (6.13). Finally, taking limits as $x \to 0$ and $y \to 0$ gives

$$\frac{\mathrm{d}M_{0,0}}{\mathrm{d}t} = \lim_{\substack{x\to 0\\ y\to 0}} \{A(x,y,t)\} - \lim_{\substack{x\to 0\\ y\to 0}} \{B(x,y,t)\}. \tag{6.20}$$

The terms involving $A(x,y,t)$ and $B(x,y,t)$ are further simplified for cases where $a_{j,k,r,s}$ and $b_{j,k,r,s}$ take the values given in Table 6.1.

6.3.2 Model 1

In model 1, the kernels used are $a_{j,k,r,s} = a$ and $b_{j,k,r,s} = b$. First, substituting this form for the aggregation kernel in equation (6.17)

$$A(x,y,t) = \frac{aC(x,y,t)}{2}\left(C(x,y,t) - 2M_{0,0}\right), \tag{6.21}$$

and

$$A(0,0,t) = -\frac{a{M_{0,0}}^2}{2}. \tag{6.22}$$

The fragmentation term $B(x,y,t)$ simplifies to

$$\begin{aligned} B(x,y,t) =& \frac{b}{2}\left(\frac{\partial^2 C}{\partial x \partial y} - \frac{\partial C}{\partial x} - \frac{\partial C}{\partial y} - C(x,y,t)\right) \\ &+ \frac{b}{(1-e^{-x})(1-e^{-y})}\left\{e^{-x}C(x,0,t) + e^{-y}C(0,y,t)\right. \\ &\left.+C(x,y,t)(1-e^{-x}-e^{-y}) + M_{0,0}(t)(e^{-(x+y)} - e^{-x} - e^{-y})\right\}. \end{aligned} \tag{6.23}$$

Taking limits we find,

$$B(0,0,t) = \lim_{\substack{x\to 0\\ y\to 0}} B(x,y,t) = -\frac{b}{2}\left(M_{1,1} + M_{1,0} + M_{0,1} - M_{0,0}\right). \tag{6.24}$$

So, from equation (6.20), $M_{0,0}$ for model 1 is given by

$$\frac{\mathrm{d}M_{0,0}(t)}{\mathrm{d}t} = -\frac{aM_{0,0}^2}{2} + \frac{b}{2}\left(M_{1,1} + M_{1,0} + M_{0,1} - M_{0,0}\right). \tag{6.25}$$

$M_{1,1}$ is not known, but can be found by differentiating equation (6.16) with respect to x and y, then taking the limit as $x \to 0$ and $y \to 0$,

$$\frac{\mathrm{d}M_{1,1}}{\mathrm{d}t} = \lim_{\substack{x\to 0\\ y\to 0}}\left(\frac{\partial^2 C}{\partial x \partial y}\right) = \lim_{\substack{x\to 0\\ y\to 0}}\left(\frac{\partial^2 A}{\partial x \partial y}\right) - \lim_{\substack{x\to 0\\ y\to 0}}\left(\frac{\partial^2 B}{\partial x \partial y}\right). \tag{6.26}$$

Asymptotics will be used to solve the system, assuming $b \ll a = \mathcal{O}(1)$, giving solutions of the form

$$\begin{aligned} M_{0,0}(t) =& M_{0,0}^{(0)}(t) + bM_{0,0}^{(1)}(t) + b^2 M_{0,0}^{(2)}(t) + \ldots, \\ M_{1,1}(t) =& M_{1,1}^{(0)}(t) + bM_{1,1}^{(1)}(t) + b^2 M_{1,1}^{(2)}(t)^2 + \ldots. \end{aligned} \tag{6.27}$$

By differentiating equation (6.21), then taking limits,

$$\frac{\mathrm{d}M_{1,1}}{\mathrm{d}t} = aM_{0,1}M_{1,0} + \mathcal{O}(b) \tag{6.28}$$

to leading order. Therefore, to leading order, solutions are

$$M_{0,0}^{(0)}(t) = \frac{2M_{0,0}(0)}{atM_{0,0}(0)+2}, \tag{6.29}$$

$$M_{1,1}^{(0)}(t) = aM_{0,1}M_{1,0}t + M_{1,1}(0). \tag{6.30}$$

To simplify the calculation of the first correction term, $M_{0,0}^{(1)}$, a new timescale,

$$\tau = M_{0,0}(0)at + 2 \tag{6.31}$$

(with $\tau > 2$), is introduced. Using this timescale, the form of the solution is

$$\begin{aligned} M_{0,0}(t) =& \hat{M}_{0,0}(\tau) = \hat{M}_{0,0}^{(0)}(\tau) + b\hat{M}_{0,0}^{(1)}(\tau) + b^2\hat{M}_{0,0}^{(2)}(\tau) + \ldots, \\ M_{1,1}(t) =& \hat{M}_{1,1}(\tau) = \hat{M}_{1,1}^{(0)}(\tau) + b\hat{M}_{1,1}^{(1)}(\tau) + b^2\hat{M}_{1,1}^{(2)}(\tau) + \ldots, \end{aligned} \tag{6.32}$$

and by inference,

$$M_{0,0}^{(0)}(t) = \hat{M}_{0,0}^{(0)}(\tau) = \frac{2M_{0,0}(0)}{\tau} \tag{6.33}$$

$$M_{1,1}^{(0)}(t) = \hat{M}_{1,1}^{(0)}(\tau) = \frac{M_{0,1}M_{1,0}(\tau-2)}{M_{0,0}(0)} + M_{1,1}(0). \tag{6.34}$$

The first correction term, $\hat{M}_{0,0}^{(1)}(\tau)$, is found by re-expressing Equation (6.25) in terms of τ, and equating terms of order b, giving

$$\begin{aligned} \frac{\mathrm{d}\hat{M}_{0,0}^{1}}{\mathrm{d}\tau} + \frac{2}{\tau}\hat{M}_{0,0}^{1} = \frac{1}{2aM_{0,0}(0)^2}\big[&M_{1,0}M_{0,1}(\tau-2) + M_{0,0}(0)(M_{1,1}(0) \\ &+M_{0,1}+M_{1,0}) - 2M_{0,0}(0)^2/\tau\big]. \end{aligned} \tag{6.35}$$

Then to $\mathcal{O}(b)$ we have

$$\begin{aligned} \hat{M}_{0,0} =& \frac{2M_{0,0}(0)}{\tau} + \frac{b}{24aM_00(0)^2\tau^2}\big[M_{0,1}M_{1,0}\{3(\tau^4-2^4) - 8(\tau^3-2^3)\} \\ &+ 4M_{0,0}(0)(M_{1,1}(0)+M_{0,1}+M_{1,0})(\tau^3-2^3) - 12M_{0,0}(0)^2(\tau^2-2^2)\big], \end{aligned} \tag{6.36}$$

with τ given by equation (6.31). This solution is suitable for use in the fitting procedure described in Chapter 7, which is similar to that described in §4.2.

6.3.3 Model 2

Model 2 uses the same fragmentation kernel as model 1, but introduces a new aggregation kernel, $a_{j,k,r,s} = \hat{a}(j+r) + \bar{a}(k+s)$. Using this kernel,

$$A(x,y,t) = \left(\hat{a}\frac{\partial C}{\partial x} + \bar{a}\frac{\partial C}{\partial y}\right)(M_{0,0} - C) - C(\hat{a}M_{1,0} + \bar{a}M_{0,1}). \tag{6.37}$$

so

$$A(0,0,t) = -M_{0,0}(\hat{a}M_{1,0} + \bar{a}M_{0,1}). \tag{6.38}$$

Hence

$$\frac{\mathrm{d}M_{0,0}}{\mathrm{d}t} = -M_{0,0}(\hat{a}M_{1,0} + \bar{a}M_{0,1}) + \frac{b}{2}\left(M_{1,1} + M_{1,0} + M_{0,1} - M_{0,0}\right). \tag{6.39}$$

As before, $M_{1,1}(t)$ is required to find a solution. The more complicated rate means that the differential equation for $M_{1,1}$ includes terms in $M_{2,0}$ and $M_{0,2}$. Differential equations for $M_{2,0}$ and $M_{0,2}$ can be found by differentiating equation (6.16) twice with respect to x to obtain $M_{2,0}$ and twice with respect to y to obtain $M_{0,2}$. This procedure gives the system of equations,

$$\frac{\mathrm{d}M_{2,0}}{\mathrm{d}t} = M_{2,0}(2\hat{a}M_{1,0}) + M_{1,1}(2\bar{a}M_{1,0}) + \mathcal{O}(b), \tag{6.40}$$

$$\frac{\mathrm{d}M_{1,1}}{\mathrm{d}t} = M_{2,0}(\hat{a}M_{0,1}) + M_{1,1}(\hat{a}M_{1,0} + \bar{a}M_{0,1}) + M_{0,2}(\bar{a}M_{1,0}) + \mathcal{O}(b), \tag{6.41}$$

$$\frac{\mathrm{d}M_{0,2}}{\mathrm{d}t} = M_{1,1}(2\hat{a}M_{0,1}) + M_{0,2}(2\bar{a}M_{0,1}) + \mathcal{O}(b), \tag{6.42}$$

which is decoupled from equation (6.39). For $b \ll \bar{a}, \hat{a} = \mathcal{O}(1)$, to leading order the solution to equation (6.39) is

$$M_{0,0} = M_{0,0}(0)e^{-\mu t}, \tag{6.43}$$

where

$$\mu = (\hat{a}M_{1,0} + \bar{a}M_{0,1}). \tag{6.44}$$

Equations (6.40)–(6.42) form a linear system

$$\frac{\mathrm{d}}{\mathrm{d}t}\begin{pmatrix} M_{2,0} \\ M_{1,1} \\ M_{0,2} \end{pmatrix} = \begin{pmatrix} 2\hat{a}M_{1,0} & 2\bar{a}M_{1,0} & 0 \\ \hat{a}M_{0,1} & \hat{a}M_{1,0} + \bar{a}M_{0,1} & \bar{a}M_{1,0} \\ 0 & 2\hat{a}M_{0,1} & 2\bar{a}M_{0,1} \end{pmatrix}\begin{pmatrix} M_{2,0} \\ M_{1,1} \\ M_{0,2}. \end{pmatrix}, \tag{6.45}$$

solved by

$$\begin{pmatrix} M_{2,0} \\ M_{1,1} \\ M_{0,2} \end{pmatrix} = K_1 \begin{pmatrix} \bar{a}/\hat{a} \\ -1 \\ \hat{a}/\bar{a} \end{pmatrix} + K_2 \begin{pmatrix} -\bar{a}M_{1,0} \\ \lambda/2 \\ \hat{a}M_{0,1} \end{pmatrix} e^{\mu t} + K_3 \begin{pmatrix} M_{1,0}/M_{0,1} \\ 1 \\ M_{0,1}/M_{1,0} \end{pmatrix} e^{2\mu t}, \quad (6.46)$$

where

$$\lambda = \hat{a}M_{1,0} - \bar{a}M_{0,1}. \quad (6.47)$$

Using general initial conditions, the constants of integration, K_1, K_2 and K_3 are given by

$$K_1 = \frac{\hat{a}\bar{a}(\bar{a}M_{2,0}(0)M_{0,1}^3 + \hat{a}M_{0,2}(0)M_{1,0}^3 - M_{1,1}M_{1,0}M_{0,1}\mu)}{\hat{a}^2M_{1,0}^2\bar{a}M_{0,1} + \hat{a}^3M_{1,0}^3 + \hat{a}M_{1,0}\bar{a}^2M_{0,1}^2 + M_{0,1}^3\bar{a}^3}, \quad (6.48)$$

$$K_2 = \frac{M_{1,1}(0)(\hat{a}M_{1,0} - \bar{a}M_{0,1}) - \hat{a}M_{2,0}(0)M_{0,1} + \bar{a}M_{1,0}M_{0,2}(0)}{\bar{a}^2M_{0,1}^2 + \hat{a}^2M_{1,0}^2}, \quad (6.49)$$

$$K_3 = \frac{M_{1,0}M_{0,1}(\bar{a}^3M_{0,1}M_{0,2}(0) + \hat{a}^3M_{1,0}M_{2,0}(0))}{\mu(\bar{a}^2M_{0,1}^2 + \hat{a}^2M_{1,0}^2)} + \frac{\bar{a}\hat{a}M_{1,1}(0)}{(\bar{a}^2M_{0,1}^2 + \hat{a}^2M_{1,0}^2)}. \quad (6.50)$$

The correction term for $M_{0,0}^{(1)}$ is found by solving

$$\frac{\mathrm{d}M_{0,0}^{(1)}}{\mathrm{d}t} + M_{0,0}^{(1)}(\hat{a}M_{1,0} + \bar{a}M_{0,1}) = \frac{1}{2}\left(-K_1 + K_2e^{\mu t}(\hat{a}M_{1,0} - \bar{a}M_{0,1})/2 + K_3e^{2\mu t} + M_{1,0} + M_{0,1} - M_{0,0}(0)e^{-\mu t}\right), \quad (6.51)$$

which yields

$$M_{0,0}^{(1)} = \frac{1}{12\mu}\left[6K_1(e^{-\mu t} - 1) + 3K_2(\hat{a}M_{1,0} - \bar{a}M_{0,1})\sinh(\mu t) + 2K_3(e^{2\mu t} - e^{-\mu t}) + 6(M_{1,0} + M_{0,1})(1 - e^{-\mu t}) - 6\mu M_{0,0}(0)te^{-\mu t}\right], \quad (6.52)$$

so

$$M_{0,0}(t) = M_{0,0}(0)e^{-\mu t} + \frac{b}{12\mu}\left[6K_1(e^{-\mu t} - 1) + 3K_2(\hat{a}M_{1,0} - \bar{a}M_{0,1})\sinh((\mu t)) + 2K_3(e^{2\mu t} - e^{-\mu t}) + 6(M_{1,0} + M_{0,1})(1 - e^{-\mu t}) - 6\mu M_{0,0}(0)te^{-\mu t}\right] \quad (6.53)$$

with μ given by equation (6.44).

Having found this solution and the equivalent solution for model 1 (equation (6.36)), it is possible to test the models by fitting them to data taken from the literature. The fitting procedure determines the model parameters, a, or $\hat{a}$ and $\bar{a}$, and b. The next chapter explains how this is achieved, describing methods that reconcile differences between experimental sieved size measurements and the cluster predictions made by the model. The fitting procedure is demonstrated and numerical solutions to the mixing system are presented.

Chapter 7

Experimental Comparison

A generalised Smoluchowski model was proposed in Chapter 6. The accompanying analysis gave approximations for $M_{0,0}(t)$ for the two kernel combinations listed in Table 6.1. This chapter discusses how parameters and initial conditions can be determined from experimental data. The model is able to predict changes in the size distribution and composition of a binary powder mixture using this information.

Fitting techniques are used to obtain parameters. The fitting method is adapted from the method used for one-component systems (described in Chapter 4). Once parameters are obtained the models are solved numerically, and the calculated size and composition distributions are compared to those measured experimentally. Data presented by Aikin and Courtney [1] has been used for this task, as they have carefully estimated the rate at which the powder has mixed using a detailed energy dispersive X-ray (EDX) analysis.

The next section describes how experimental size distributions from mixing experiments can be compared to two-component cluster size distributions. In many cases only the size distribution of the material is measured and mixing is not accurately quantified. The fitting method described can establish parameters for the models from size data alone, and mixing characteristics are

calculated using these parameters giving more in-depth data on phenomena that are difficult to measure.

7.1 Two-component cluster distributions and sieved size measurements and

Size distributions are measured experimentally by sieving the powder. The thinning disc and constant thickness disc approximations of particle shape have been used to convert sieve size measurements into volumetric cluster size distributions, as in the one-component case (§4.1). However, a two-component cluster distribution cannot be obtained from sieved size data without measuring the composition of a representative sample of individual particles, which is an extremely time consuming task.

This limitation does not affect the fitting techniques proposed here. The fitting matches the total number of particles in the model (irrespective of size and composition), $M_{0,0}$, to a similar quantity calculated from the experimental data. The moment $M_{0,0}$ is the sum of all the concentrations $c_{r,s}$

$$M_{0,0} = \sum_{r=0}^{\infty} \sum_{s=0}^{\infty}{}' c_{r,s}. \tag{7.1}$$

The sum can be re-ordered, so that clusters with different compositions but the same volumetric size are summed, giving a one-component cluster size distribution. The value of M_0 for this distribution can the be calculated, and is equivalent to the $M_{0,0}$ value of the two-component distribution.

Reducing the two-component distribution to a one-component size distribution is easily achieved if $V_A = V_B$. The volumetric size of a cluster is given by $V_A(r + s)$, and lines of equal cluster size are oriented as shown in Figure

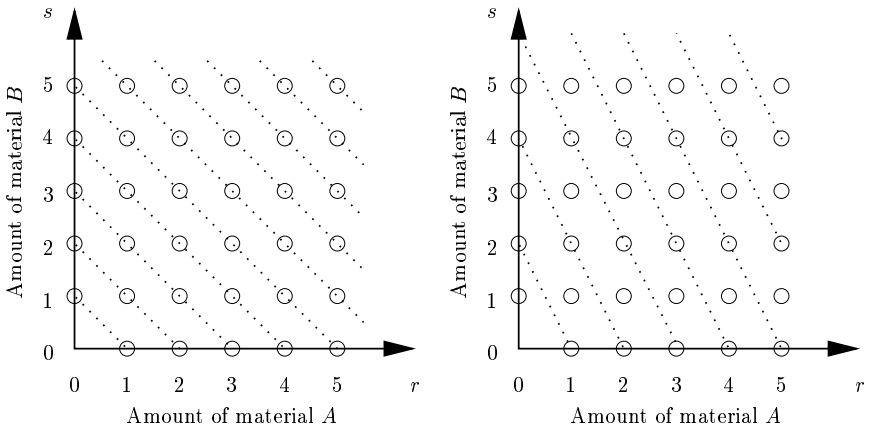

(a) $V_A = V_B$ (b) $V_A = 2V_B$

Figure 7.1: The size domain of a two-component cluster distribution $c_{r,s}$ is shown, with lines of equal volumetric cluster size marked. Two relationships between the volume of monomers of different materials (V_A and V_B) are considered.

7.1(a). The definition of $M_{0,0}$ can be re-expressed

$$M_{0,0} = \sum_{r=1}^{\infty} \sum_{s=0}^{r} c_{s,r-s}, \tag{7.2}$$

or,

$$M_{0,0} = M_0^{(1)} = \sum_{r=1}^{\infty} c_r^{(1)}, \tag{7.3}$$

where

$$c_r^{(1)} = \sum_{s=0}^{r} c_{s,r-s}. \tag{7.4}$$

The two-component distribution is collapsed to a one-component size distribution by removing information concerning composition. The sub-total $c_r^{(1)}$ is the total of all clusters lying on the r^{th} line from the origin in Figure 7.1(a). The fitting algorithm does not need to assign a value to each concentration, $c_{r,s}$, but instead approximates the value of $c_r^{(1)}$ for each r.

If $V_A \neq V_B$ then the conversion of the two-component distribution to a one-component distribution becomes more complicated. In general, where $V_A = \alpha V_B$ for any $\alpha > 0$, the problem is non-trivial. The case where $V_A = 2V_B$ is illustrated in Figure 7.1(b). The lines of equal cluster size are more steeply inclined, and it is more difficult to write a closed form definition of $c_r^{(1)}$. Although the conversion process does not require such a definition, the conversion is more straight forward if $V_A = V_B$ and this condition is assumed for the rest of this discussion. The more general case allows the model to be numerically solved with greater efficiency, so if the model were to be widely adopted then a conversion should be implemented that accounts for different monomer sizes.

Adopting the condition $V_A = V_B$ allows the two-component distribution to be easily collapsed to form a one-component size distribution. The method presented in §4.1 allows the experimental sieved size results to be converted to a one-component distribution and values of $M_{0,0}$ can be calculated by equation (7.3). The value of $M_{0,0}$ provided by this procedure gives sufficient information for our purposes at all times $t > 0$. However, the initial size distribution at $t = 0$ must be determined completely to provide an initial condition from which to start the model. The initial powders used by Aikin and Courtney will not contain mixed composition particles, however, so the initial cluster distribution, $c_{r,s}(0)$, can be constructed from two one-component distributions mixed in the correct proportions. These one-component distributions will lie along the r and s axes, as the initial clusters contain only one type of volume element.

Finally, since the system will be solved numerically a suitable truncation

must be determined. Equation (6.3) may be truncated to conserve mass, giving

$$\begin{aligned}\frac{\mathrm{d}c_{r,s}}{\mathrm{d}t} =& \frac{1}{2}\sum_{j=0}^{r}\sum_{k=0}^{s}{}' \left(a_{j,k,r-j,s-k}\, c_{j,k}\, c_{r-j,s-k} - b_{j,k,r-j,s-k}\, c_{r,s}\right) \\ & - \sum_{j=0}^{N-r}\sum_{k=0}^{M-s'} \left(a_{j,k,r,s}\, c_{j,k}\, c_{r,s} - b_{j,k,r,s}\, c_{r+j,s+k}\right).\end{aligned} \tag{7.5}$$

here N and M are the size of the system, $C_{N,M}$ being the largest cluster size considered. This form is analogous to equation (1.12). Values of N and M must be chosen so that the numerical calculation is computationally efficient, but also so that accuracy is maintained. Although the maximum particle size is easily measured in an experiment, the composition of such large particles is much harder to determine. The safest truncation is therefore to allow the largest observed particles to be formed entirely from one material or the other. However, particle size often increases substantially during milling, and under these circumstances the largest particles are most likely well mixed. If the largest particle found in the system is 85% material A and 15% material B then M can be set considerably lower than N reducing the number of clusters in the size domain considerably. This approach, based on assumed mixing, is used for the calculations presented in §7.3. However, for systems where welding is not the dominant event, or where mixing can not be guaranteed, a larger (r, s)-domain should be considered.

7.2 Experimental mixing measures

The values of $M_{0,0}$ and the initial conditions obtained from the experimental data provide sufficient information for the model to be matched to the experiment. A fitting procedure is used to determine the model parameters using Gnuplot, as before (see §4.2). The data used to verify the two-component models are taken from a paper published by Aikin and Courtney [1]. Aikin

Material	Molar volume (cm^3)
Cu	7.11
Cr	7.23
Nb	10.83

Table 7.1: Molar volumes for Cu, Cr, Nb at 298 Kelvin.

and Courtney use a vertical attritor to mechanically alloy two different powder mixtures, Cu–15vol%Nb and Cu–15vol%Cr. The particle size data published by Aikin and Courtney has particular value in this context because it is accompanied by measurements of particle composition. This data was obtained by studying a representative sample of powder particles using an EDX system, measuring the composition of each of the particles in turn. They classify particles as either elemental A, elemental B or composite according to certain composition thresholds. A particle is counted as elemental Cu if the EDX analysis returns a 95% purity reading or greater. The threshold for a pure Nb or Cr particle is set lower, at 90%. All other particles are classified as composite. It is suggested that the background signal generated by Cu material in the sample holder justifies the higher threshold value of 95% used to define a pure Cu particle.

The distributions calculated by our model can be compared to Aikin and Courtney's findings to determine whether the two-component models accurately model mixing phenomena. When making this comparison it is important to note that the EDX analyses measure the proportion of different atoms present in the material. Corresponding volumetric percentages can be calculated using the molar volumes presented in Table 7.1. Having set volumetric thresholds, the clusters concentrations calculated by the model can be subjected to Aikin and Courtney's classification procedure and the results can be compared to their experimental equivalents.

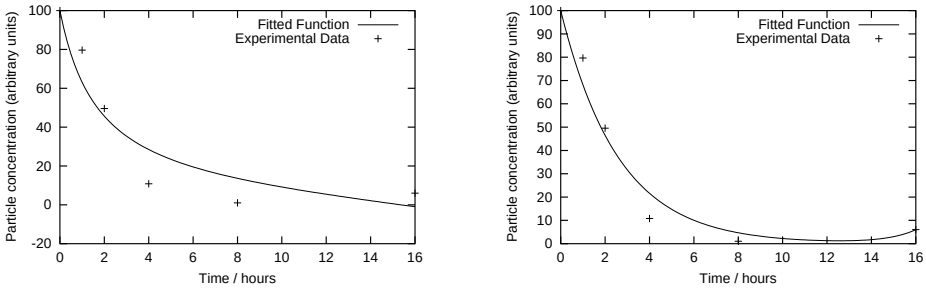

(a) Model 1.

(b) Model 2.

Figure 7.2: Obtaining model parameters by fitting total particle size in the model (fitted function) to data from Aikin and Courtney's Cu–15vol%Cr milling experiment (experimental data).

7.3 Experimental comparison

The data presented by Aikin and Courtney has been processed using the methods outlined above. Sieve size measurements are converted to derive suitable values for $M_{0,0}$ from the experimental data. These values are used to fit the model parameters, a and b (model 1) or $\hat{a}$, $\bar{a}$ and b (model 2) by programming equations (6.36) and (6.53) into Gnuplot. The lines of best fit shown in Figure 7.2 and Figure 7.3 are obtained in this way. Corresponding parameter values are shown in Table 7.2.

Unfortunately, the results of the fitting procedure are not good. The fracture rates produced are negative, except for model 2 with data from the Cu–15%Cr experiment. This implies that the balance between welding and fracture events in the proposed models is tipped too heavily in favour of fragmentation, or that the assumed distribution of fragments is inappropriate. It is reasonable that a strong fragmentation kernel is more suited to experiments where more brittle alloys are created, such as Cu–15vol%Cr.

Notwithstanding this disappointment, model 2 has been applied to Aikin

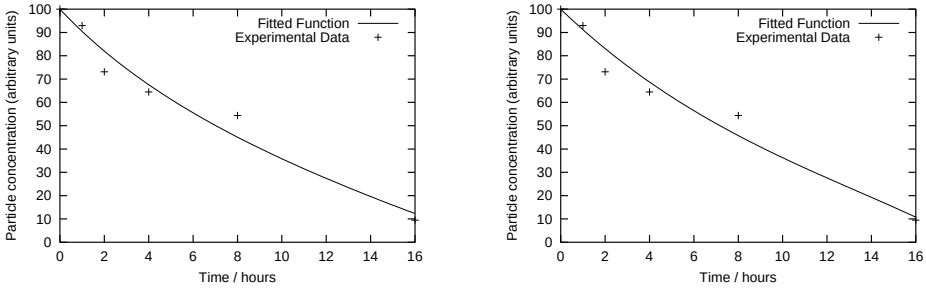

(a) Model 1.

(b) Model 2.

Figure 7.3: Obtaining model parameters (as above) for data from Aikin and Courtney's Cu–15vol%Nb milling experiment.

Experiment	a	b
Cu–15vol%Cr	1.147×10^{-2}	-1.031×10^{-2}
Cu–15vol%Nb	1.587×10^{-3}	-4.499×10^{-2}

(a) Model 1.

Experiment	$\hat{a}$	$\bar{a}$	b
Cu–15vol%Cr	4.407×10^{-3}	5.621×10^{-4}	3.721×10^{-6}
Cu–15vol%Nb	1.493×10^{-4}	5.130×10^{-3}	-4.208×10^{-3}

(b) Model 2.

Table 7.2: Parameter values obtained by fitting the models to Aikin and Courtney's milling experiments.

and Courtney's Cu–15vol%Cr data to determine how well the model mimics the experiment. Figure 7.4 shows the cluster size distributions calculated by the model. The cluster distribution can be summed along lines of equal volume and compared to experimental sieved size distributions. This comparison is made in Figure 7.6. The two-component model has predicted changes in the powder's size distribution with a reasonable degree of accuracy.

Figure 7.6 compares the rate of mixing in the model to that measured by Aikin and Courtney using EDX analysis. Mixing proceeds more slowly in the model than in the experiment. However, the calculations demonstrate the potential of this modelling approach. The predicted cluster distribution curves (Figure 7.4) match changes in particle size well, but are spread too widely. The distribution should form a more concentrated ridge. A revised model is proposed to increase the slow mixing rate and increase the number of clusters with an even mix of constituents. Models 1 and 2 assume simple constant fragmentation behaviour, where all the possible fragment combinations from a particular fragmented particle are equally likely. An improved kernel is presented in the following section that is derived from a more thorough statistical analysis of a fragmentation event.

7.4 An improved fragmentation kernel

Both of the two models already proposed use the simple fragmentation kernel $b_{j,k,r,s} = b$. This kernel is simple mathematically but makes the counterintuitive assumption that the rate of particle fragmentation is independent of both size and composition. Comparison with experiments (Figure 7.6) suggest that this assumption is invalid. A more accurate composition dependence for fragmentation is proposed. The current kernel assumes all fragment combinations are equally likely, whereas the new kernel assumes that fracture will split a

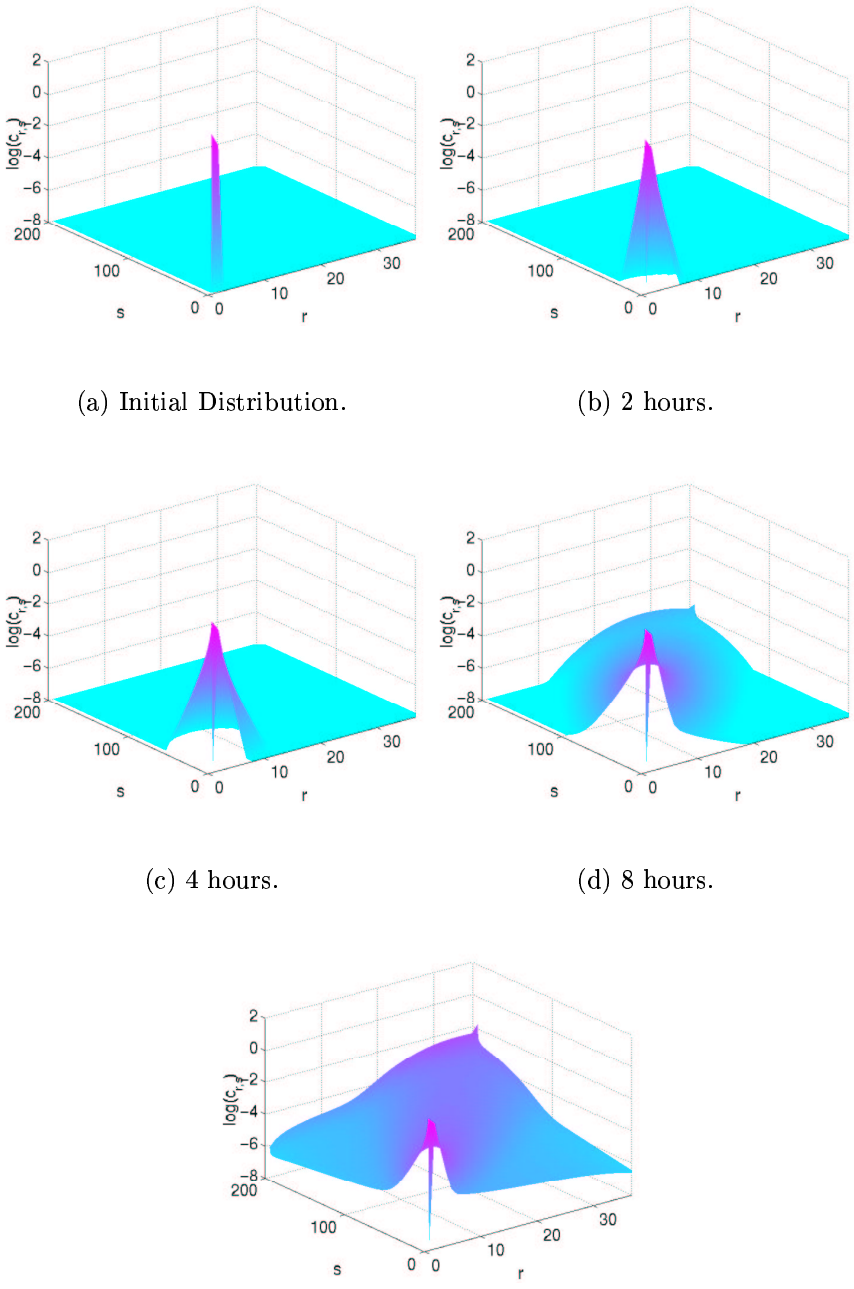

(a) Initial Distribution.

(b) 2 hours.

(c) 4 hours.

(d) 8 hours.

(e) 16 hours.

Figure 7.4: Cluster distributions calculated using model 2 and parameters fitted to Aikin and Courtney's Cu–15vol%Cr milling experiment.

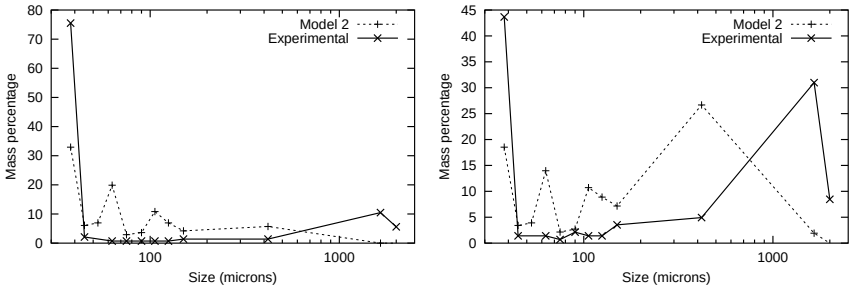

(a) Initial Distribution.

(b) 2 hours.

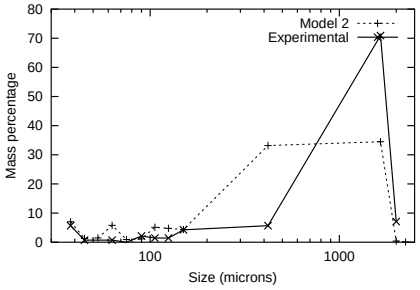

(c) 4 hours.

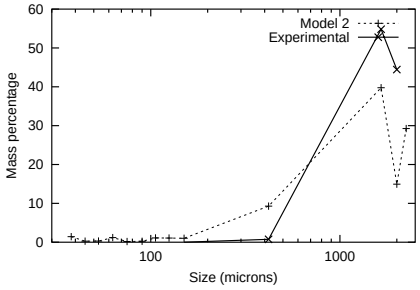

(d) 8 hours.

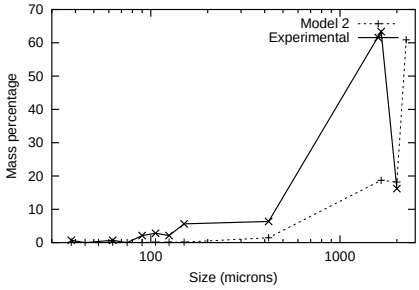

(e) 16 hours.

Figure 7.5: Sieved size distributions calculated by model 2 are compared with the results from Aikin and Courtney's Cu–15vol%Cr milling experiment.

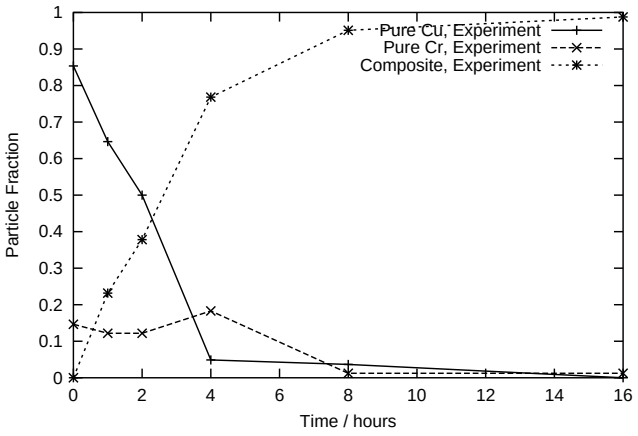

(a) Experiment.

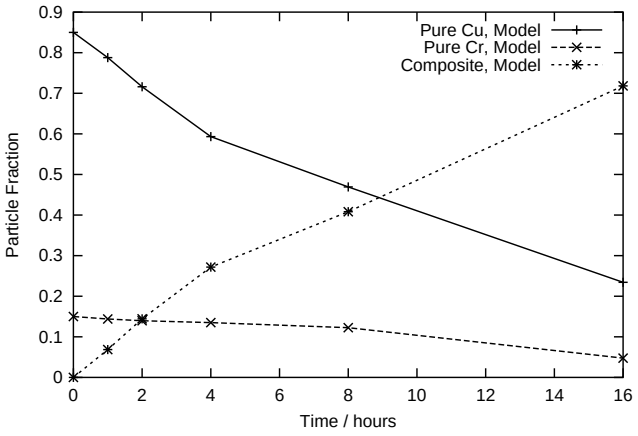

(b) Model.

Figure 7.6: Fractions of pure and composite particles predicted by the model are compared with experimental measurements made by Aikin and Courtney.

particle entirely at random, so that any part of the original particle is equally likely to appear in either fragment.

This new fragmentation rate does not account for factors related to the geometry of the particles. There will be areas in the particle rich in material A and areas rich in material B. One of the materials may fracture more easily than the other or the interface region might be particularly weak. However, these factors are ignored for the time being, as the approximation given is an improvement over the rate $b_{j,k,r,s} = b$. .

To derive the required kernel from the given assumption, the reaction

$$C_{j+r,k+s} \xrightarrow{b_{j,k,r,s}} C_{j,k} + C_{r,s} \tag{7.6}$$

is considered. It is assumed that fragmentation occurs such that the elements of the fragmented cluster are equally likely to end up in either fragment. When a cluster $C_{j+r,k+s}$ fractures, the probability of obtaining fragments $C_{j,k}$ and $C_{r,s}$ is

$$\frac{(r+s)!(r+j)!(s+k)!(j+k)!}{j!k!r!s!(j+k+r+s)!}, \tag{7.7}$$

so a new fragmentation rate is defined such that

$$b_{j,k,r,s} = b\frac{(r+s)!(r+j)!(s+k)!(j+k)!}{j!k!r!s!(j+k+r+s)!}. \tag{7.8}$$

This composition dependent fragmentation rate is used with the aggregation rate $a_{r,s,j,k} = \hat{a}(r+j) + \bar{a}(s+k)$ giving a new model, model 3.

This model has been analysed and a solution for $M_{0,0}(t)$ has been found. The solution is found by imposing the conditions

$$\begin{aligned} \hat{a} &= a + \tilde{a}, \\ \bar{a} &= a - \tilde{a}, \end{aligned} \tag{7.9}$$

and assuming $\tilde{a}, b \ll a = \mathcal{O}(1)$. These conditions restrict the applicability of the results and make it difficult to obtain suitable parameters. However, a significant subset of mechanical alloying experiments will satisfy these conditions,

so the model remains useful. Many mechanical alloying experiments are dominated by welding events and involve two materials that weld at roughly the same rate. The requirements placed on initial conditions during the derivation may limit the applicability of the model more severely; this is currently under investigation.

Using equation (6.37), the conditions given in equation (7.9) give a leading order problem,

$$\frac{1}{a}\frac{\partial C}{\partial t} = (M_{0,0} - C)\left(\frac{\partial C}{\partial x} + \frac{\partial C}{\partial y}\right) - C(M_{1,0} + M_{0,1}). \tag{7.10}$$

Setting $x = y = 0$ gives the equation

$$\dot{M}_{0,0} = -M_{0,0}\ a\ (M_{1,0} + M_{0,1}), \tag{7.11}$$

solved by

$$M_{0,0} = M_{0,0}(0)\ e^{-\nu t}, \tag{7.12}$$

where

$$\nu = a(M_{1,0} + M_{0,1}). \tag{7.13}$$

This is the leading order solution for $M_{0,0}$. However, in order to find the correction term it is necessary to solve the partial differential equation (7.10) and find a leading order solution for $c_{j,k}(t)$.

Equation (7.10) can be solved for all x and y by the method of characteristics, subject to initial conditions. Experimental measurements give the initial powder distribution, $c_{j,k}(0)$, and consequently

$$C(x, y, 0) = \sum_{j=0}^{\infty}{\sum_{k=0}^{\infty}}' c_{j,k}(0)\ e^{-(jx+ky)}. \tag{7.14}$$

These conditions are imposed on $s = 0$ and parameterised by σ and τ so that $x = \sigma$, $y = \tau$ and $C = \sum_{j=0}^{\infty}{\sum_{k=0}^{\infty}}' c_{j,k}(0)\ e^{-(j\sigma+k\tau)}$. Then the following

characteristic equations can be derived,

$$\frac{\mathrm{d}x}{\mathrm{d}s} = -a(M_{0,0} - C), \tag{7.15}$$

$$\frac{\mathrm{d}y}{\mathrm{d}s} = -a(M_{0,0} - C), \tag{7.16}$$

$$\frac{\mathrm{d}t}{\mathrm{d}s} = 1, \tag{7.17}$$

$$\frac{\mathrm{d}C}{\mathrm{d}s} = -\nu C. \tag{7.18}$$

These equations are solved, subject to the initial conditions given, by

$$t = s, \tag{7.19}$$

$$C = C(\sigma, \tau, 0)e^{-\nu s}, \tag{7.20}$$

$$x = \frac{M_{0,0}(0) - C(\sigma, \tau, 0)}{M_{1,0} + M_{0,1}} \left(e^{-\nu s} - 1\right) + \sigma, \tag{7.21}$$

$$y = \frac{M_{0,0}(0) - C(\sigma, \tau, 0)}{M_{1,0} + M_{0,1}} \left(e^{-\nu s} - 1\right) + \tau. \tag{7.22}$$

The three unknowns, σ, τ and s are eliminated between these four equations leaving a single relationship between x, y, t and C. First, s is eliminated in favour of t throughout. Noting that

$$\sigma = x - \frac{M_{0,0}(0)e^{-\nu t} - C}{(M_{1,0} + M_{0,1})e^{-\nu t}} \left(e^{-\nu t} - 1\right), \tag{7.23}$$

$$\tau = y - \frac{M_{0,0}(0)e^{-\nu t} - C}{(M_{1,0} + M_{0,1})e^{-\nu t}} \left(e^{-\nu t} - 1\right), \tag{7.24}$$

and substituting for σ and τ in equation (7.20) gives an implicit relationship for $C(x, y, t)$. However, this relationship involves $C(\sigma, \tau, 0)$ which, in general, is too complex to allow an explicit solution to be found. An explicit solution can be found if the initial conditions contain only monomer clusters, that is if $c_{j,k} = 0$ for all j and k except

$$\begin{aligned} c_{1,0} &= \rho_A, \\ c_{0,1} &= \rho_B. \end{aligned} \tag{7.25}$$

In this case, $C(\sigma,\tau,0) = \rho_A e^{-\sigma} + \rho_B e^{-\tau}$, and equation (7.20) yields

$$C(x,y,t) = \left(\rho_A e^{-\sigma} + \rho_B e^{-\tau}\right) e^{-\nu t} \tag{7.26}$$

or, substituting for σ and τ, while noting that $M_{0,0}(0) = \nu/a$,

$$C(x,y,t)e^{\nu t} \exp\left[\left(\frac{a}{\nu}Ce^{\nu t} - 1\right)\left(e^{-\nu t} - 1\right)\right] = \rho_A e^{-x} + \rho_B e^{-y} = e^{-z}. \tag{7.27}$$

Davies *et al.* [14, 15] have previously shown that

$$e^{-z} = C\exp(1 + \frac{1}{2}t - e^{t/2})\exp(-(e^{t/2} - 1)C) \tag{7.28}$$

implies

$$C = \sum_{k=1}^{\infty} e^{-kz}\frac{k^{k-1}}{k!}e^{-t/2}(1 - e^{-t/2})^{k-1}\exp(-k(1 - e^{-t/2})). \tag{7.29}$$

Applying the change of variables $\hat{t} = 2\nu t$, $\hat{C} = aC/\nu$ to equation (7.27) makes the expression directly comparable with equation (7.28), and it follows that

$$C = \sum_{k=1}^{\infty} e^{-kz}\frac{k^{k-1}}{k!}\left(\frac{a}{\mu}\right)^{k-1} e^{-\mu t}(1 - e^{-\mu t})^{k-1}\exp\left(-k(1 - e^{-\mu t})\right). \tag{7.30}$$

Then expanding $e^{-kz} = (\rho_A e^{-x} + \rho_B e^{-y})^{-k}$,

$$c_{j,k} = \frac{(r+s)^{r+s-1}{\rho_A}^r{\rho_B}^s}{r!\ s!}\left(\frac{a}{\mu}\right)^{r+s-1} e^{-\mu t}(1 - e^{-\mu t})^{r+s-1}\times \exp\left(-(r+s)(1 - e^{-\mu t})\right). \tag{7.31}$$

This is the leading order solution for $c_{j,k}$, or the exact solution where $\hat{a} = \bar{a}$ and $b = 0$. It is only valid for the initial conditions given by equation (7.25).

Returning to the calculation of the correction term for $M_{0,0}$, the full equation,

$$\dot{M}_{0,0} = -a(\rho_A + \rho_B)M_{0,0} - \tilde{a}(\rho_A - \rho_B)M_{0,0} - B(0,0,t), \tag{7.32}$$

is considered. The leading order solution to this problem has already been found, and is stated in equation (7.13). The first correction term, $M^{(1)}_{0,0}(t)$, can be found by solving

$$\frac{\mathrm{d}M^{(1)}_{0,0}}{\mathrm{d}t} = -\nu M^{(1)}_{0,0} - \frac{\tilde{a}}{a}\nu(\rho_A - \rho_B)e^{-\nu t} - B(0,0,t). \tag{7.33}$$

which is linear, and solved by the integrating factor $e^{\nu t}$. Hence

$$M_{0,0}^{(1)}(t)e^{\nu t} = \frac{\tilde{a}}{a}\nu(\rho_A - \rho_B)t - \int_0^t B(0,0,t')e^{\nu t'}\,\mathrm{d}t', \tag{7.34}$$

which requires

$$B(0,0,t)e^{\nu t} = -\frac{e^{\nu t}}{2}\sum_{r=0}^{\infty}{\sum_{s=0}^{\infty}}'\sum_{j=0}^{\infty}{\sum_{k=0}^{\infty}}' b_{j,k,r,s}c_{r+j,s+k}(t) \tag{7.35}$$

to be integrable for an explicit solution to be found. An approximation of equation (7.8) is sought to this end. First, a more convenient way to express the leading order solution for $c_{r,s}$ is obtained by defining

$$\begin{aligned} T &= (1-e^{-\mu t})\exp(-(1-e^{-\mu t})), && (7.36)\\ \tilde{\rho}_A &= \frac{2T\rho_A}{e(\rho_A+\rho_B)}, && (7.37)\\ \tilde{\rho}_B &= \frac{2T\rho_B}{e(\rho_A+\rho_B)}, && (7.38)\\ \rho &= \rho_A + \rho_B. && (7.39) \end{aligned}$$

Then, from equation (7.31),

$$c_{r,s} = \frac{\tilde{\rho}_A^r\,\tilde{\rho}_B^s\,\rho\,(r+s)^{r+s-1}\,T^{r+s}}{r!\,s!\,(e^{\mu t}-1)}. \tag{7.40}$$

so that equation (7.35) becomes

$$B(0,0,t) = \frac{b\rho}{2(e^{\nu t}-1)}\sum_{r=0}^{\infty}{\sum_{s=0}^{\infty}}'\sum_{j=0}^{\infty}{\sum_{k=0}^{\infty}}' \frac{(r+s)!\,(j+k)!}{r!\,s!\,j!\,k!\,(r+s+j+k)!}\times \tilde{\rho}_A^{r+j}\,\tilde{\rho}_B^{s+k}\,(r+s+j+k)^{r+s+j+k-1}\,T^{r+s+j+k}. \tag{7.41}$$

This more manageable expression is approximated using Stirling's formula, so that

$$\frac{(r+s)!}{r!\,s!} \sim 2^{r+s}\exp\left(\frac{-(r-s)^2}{8(r+s)}\right). \tag{7.42}$$

The more accurate approximation,

$$\frac{(r+s)!}{r!\,s!} \sim \frac{2^{r+s}}{\sqrt{\pi\phi}}\exp\left(\frac{-(r-s)^2}{8(r+s)}\right), \tag{7.43}$$

where $\phi = 2rs/(r+s)$ or $\phi = (r+s)/2$ could be used, but doing so complicates later calculations. Using the approximation given in equation (7.42) yields

$$B(0,0,t) = \frac{b\rho}{2(e^{\nu t}-1)} \sum_{r=0}^{\infty} \sum_{s=0}^{\infty}{}' \sum_{j=0}^{\infty} \sum_{k=0}^{\infty}{}' \frac{\tilde{\rho}_A^{r+j} \tilde{\rho}_B^{s+k}}{(j+k+r+s)} \times \exp\left(\frac{-(r-s)^2}{8(r+s)}\right) \exp\left(\frac{-(j-k)^2}{8(j+k)}\right). \tag{7.44}$$

The denominator, $(j+k+r+s)$ can be neglected as it is of similar order to the neglected terms from Stirling's formula. Taking the continuum limit gives

$$B(0,0,t) = \frac{b\rho}{2(e^{\nu t}-1)} \int_{r=0}^{\infty} \int_{s=0}^{\infty} \int_{j=0}^{\infty} \int_{k=0}^{\infty} \tilde{\rho}_A^{r+j} \tilde{\rho}_B^{s+k} \exp\left(\frac{-(r-s)^2}{8(r+s)}\right) \times \exp\left(\frac{-(j-k)^2}{8(j+k)}\right) \mathrm{d}k\, \mathrm{d}j\, \mathrm{d}s\, \mathrm{d}r. \tag{7.45}$$

Then changing variables so that $u = r+s$, $v = j+k$, $x = r-s$, $y = j-k$,

$$\begin{aligned} B(0,0,t) = & \frac{b\rho}{8(e^{\nu t}-1)} \int_{u=0}^{\infty} \int_{x=-u}^{u} \exp\left(\frac{-x^2}{8u}\right) \\ & \times \exp\left(\frac{1}{2}u(\log\tilde{\rho}_A + \log\tilde{\rho}_B) + \frac{1}{2}x(\log\tilde{\rho}_A - \log\tilde{\rho}_B)\right) \mathrm{d}x\, \mathrm{d}u \\ & \times \int_{v=0}^{\infty} \int_{y=-v}^{v} \exp\left(\frac{-y^2}{8v}\right) \\ & \times \exp\left(\frac{1}{2}v(\log\tilde{\rho}_A + \log\tilde{\rho}_B) + \frac{1}{2}y(\log\tilde{\rho}_A - \log\tilde{\rho}_B)\right) \mathrm{d}y\, \mathrm{d}v. \end{aligned} \tag{7.46}$$

The two integrals are identical, and can be evaluated using the Maple software package to show that

$$B(0,0,t) = b\rho I^2/2(e^{\nu t}-1) \tag{7.47}$$

where

$$I = \frac{4}{\beta}\left(\frac{2\alpha_1}{\alpha_1^2+4\beta} + \frac{2\alpha_2}{\alpha_2^2+4\beta} + \frac{1}{\sqrt{\beta}}\tan^{-1}\frac{\alpha_1}{2\sqrt{\beta}} + \frac{1}{\sqrt{\beta}}\tan^{-1}\frac{\alpha_1}{2\sqrt{\beta}}\right), \tag{7.48}$$

and $\beta = (L_A + L_B) - (L_A - L_B)^2$, $\sigma_1 = 1 + 2L_A - 2L_B$, $\sigma_2 = 1 - 2L_A + 2L_B$, $L_A = -\log(2T\rho_A/e(\rho_A + \rho_B))$, $L_B = -\log(2T\rho_B/e(\rho_A + \rho_B))$.

At small times the $\log(T)$ term dominates and $L_A \sim L_B \sim -\log(T)$, $\beta \sim -2\log(T)$, $\alpha_1 \sim 1 + 2\log(\rho_B/\rho_A)$, $\alpha_2 \sim 1 + 2\log(\rho_A/\rho_B)$. It follows that $I \sim 3/2(\log T)^2$ and therefore

$$B(0,0,t) \sim \frac{9b\rho}{8(e^{\nu t} - 1)[\log(T(t))]^4}. \tag{7.49}$$

A naive small-t expansion of $T(t)$ as $\log(\mu t)$, is too crude, since it generates a singularity at $t = 1/\nu$. Using Aikin and Courtney's data, this singularity occurs at 4 hours, so the data points at 8 and 16 hours can not be used for fitting purposes and using the point at 4 hours introduces significant inaccuracy. A more accurate approximation of $T(t)$ must be found that additionally allows the integral in equation (7.34) to be evaluated.

The integral has the form

$$J = \int_0^t \frac{9b\rho}{8(1 - e^{-\nu t'})[\log(T(t'))]^4}\,\mathrm{d}t' \tag{7.50}$$

which can be evaluated by applying the substitution $e^x = 1 - e^{-t'}$, giving

$$J = \int_0^{\log(1-e^{-t})} \frac{\mathrm{d}x}{(x - e^x)^4(1 - e^x)}. \tag{7.51}$$

The denominator, $f(x) = (x - e^x)^4(1 - e^x)$, is approximated so that the integral can be calculated explicitly. Noting that x is negative for all $t \geq 0$ and that $f(x) \to -x$ as $x \to 0$, $f(x) \to x^4$ as $x \to -\infty$, the approximation $\tilde{f}(x) = x^4 - x$ is constructed. The relative error incurred by using this approximation is shown in Figure 7.7. Using this approximation, it follows that

$$J = \frac{3b\rho\nu}{8}\left[\log\left(1 - \frac{1}{\log(1 - e^{-\nu t})}\right)\right], \tag{7.52}$$

and consequently, the expression for the number of clusters in the model is

$$M_{0,0}(t) = \rho e^{-\nu t} + \tilde{a}({\rho_A}^2 - {\rho_B}^2)te^{-\nu t} - \frac{3b\rho\nu}{8}\left[\log\left(1 - \frac{1}{\log(1 - e^{-\nu t})}\right)\right]. \tag{7.53}$$

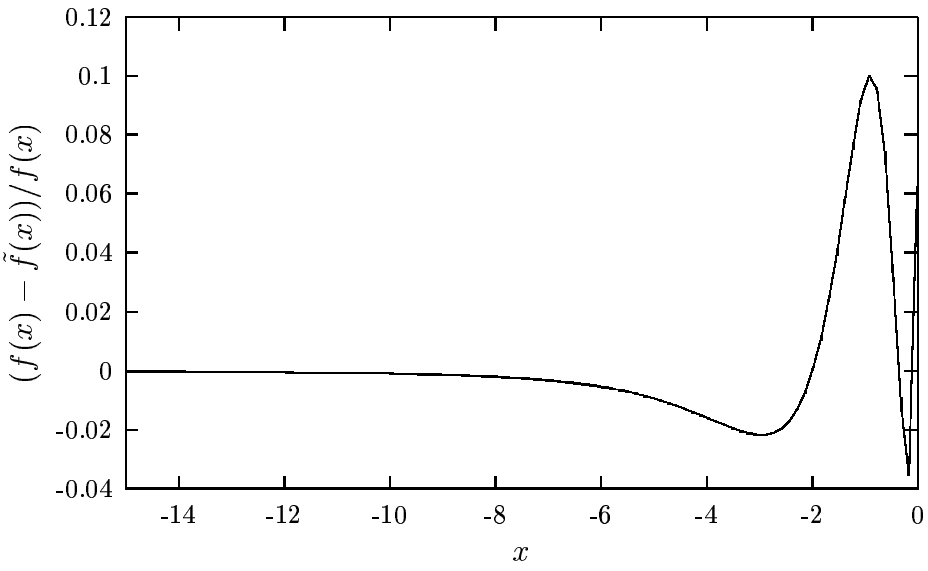

Figure 7.7: The relative error incurred when approximating $f(x) = (x - e^x)^4(1 - e^x)$ by $\tilde{f}(x) = x^4 - x$.

This expression for $M_{0,0}(t)$ has been used to obtain parameters for model 3 that correspond to Aikin and Courtney's Cu–15%Nb experiment. The fitted parameters have been used to obtain a corresponding numerical solution for $c_{r,s}(t)$. However, values of $M_{0,0}$ derived from the numerical solution diverge from those used for the fitting, indicating some inaccuracy in the process. It is possible that the approximation used for Stirling's formula is responsible for the inaccuracy. The exact cause of the discrepancy is a topic for further investigation.

Chapter 8

Conclusions

8.1 Summary

This thesis has modelled aspects of the mechanical alloying process using Smoluchowski's coagulation-fragmentation equations, a specific type of population balance model. The difficulties associated with applying this model have been addressed and resolved.

Part I of this thesis looks at one-component systems, where a powder of constant composition is milled. Changes in powder particle size distribution can be predicted for a wide range of milling conditions and powder materials. Different kernel forms have been investigated to determine which forms model the process most accurately. When using kernels of the form $a_{r,s} = a(r+s)$ and $b_{r,s} = b$ the model is both accurate and robust, with no asymptotics required to complete the fitting procedure and no gelation effects. These kernels suit most milling experiments well, indicating that the rate of particle welding is proportional to the size of both the particles involved. Larger particles are more likely to be involved in a collision as they occupy a larger volume. Accounting for this factor alone gives the rates $a_{r,s} = a(rs)$ and $b_{r,s} = b(r+s)$. The accuracy of the rates used in model 2 suggests that, when involved in

a collision, larger particles are less likely to weld or fragment than smaller particles.

With the fracture rate $b_{r,s} = b$, as used in model 2, fracture occurs in such a way that all combinations of fragment size are equally likely. Chipping events yielding a small fragment and a large fragment are as likely as events that split a cluster into two equal parts. Since large particles are more likely to be involved in a collision than smaller particles by a factor $(r + s)$ (the size of the fragmenting particle), the success of this constant rate suggests that, when involved in a collision, large particles are less likely to fragment than small particles. This conclusion is not universal, though, as model 3 is sometimes more accurate than model 2. It is difficult to assess the overall accuracy of model 3, which uses a fragmentation rate $b_{r,s} = b(r + s)$, because asymptotic methods are used to obtain a solution for $M_0(t)$. In cases where model 3 is more accurate than model 2, different size particles are equally likely to fracture when they experience a collision.

Many difficulties have been overcome to apply Smoluchowski's models to mechanical alloying. The different methods used to measure particle-size in the model and experiments have been reconciled and a fitting procedure has been developed to determine model parameters. Using the fitting method avoids the need to explicitly specify the dependence of welding and fracture rates on milling conditions. The fitted rate parameters are influenced by many properties of the experimental setup including the mill geometry, the mechanical properties of the powder, and properties of the milling media and mill chamber material. Properties that alter over time as a consequence of work hardening or changes in temperature are implicitly averaged over the time period considered. The values obtained by fitting the parameters show that rates alter with milling conditions in an intuitive way. For example a greater emphasis is placed on fracture events when more brittle materials are milled and both

welding and fracture rates become greater if the milling intensity is increased.

The models presented in Part I are similar to those developed by Aikin and Courtney. Our models examine the size dependence of welding and fracture events more closely, and use a refined method to determine parameter values. In addition we have applied them to more milling scenarios and found that they may be applied to hard and soft metals and different milling apparatus.

Part II introduces a generalisation of Smoluchowski's model that uses two-component clusters to model the mixing which occurs during mechanical alloying. The model is applied to experimental data using a similar method to that developed in Part I. The most simple and most successful kernels from Part I have been generalised to two-components, demonstrating the potential of this type of model. Changes in particle size distribution are predicted by the two-component model in a similar way to the one-component model. In addition, the two-component models predict composite formation, but mixing proceeds at a slower rate than that observed in experiments. A more accurate composition-dependent fragmentation kernel has been proposed to resolve this problem. The full application of this kernel has not yet been completed, but the application seems possible. Hopefully more accurate results will achieved.

The models, in their current form are valuable to materials scientists. The one-component model is a powerful interpolation and extrapolation tool, allowing more rapid development of powders with particular size distribution characteristics. The basis of the modelling is sound, and accurate kernel forms have been determined. With more work it may be possible to estimate the change in welding and fracture rates associated with the use of process control agents or adjustments in milling parameters. It would certainly be possible to determine how the rates are affected by adjustments to milling parameters within a particular scenario.

The two-component mixing models offer more detailed information con-

cerning the size and composition distribution of the powder than similar models proposed by Aikin and Courtney [1]. Some refinement of the kernel forms is required before the models will accurately reflect the mixing in Aikin and Courtney's experiments. However, the groundwork has been laid for the development of such models. The future work proposed in the following section would add significant value to what has already been achieved.

8.2 Future work

Analysing the composition-dependent two-component kernel given in equation (7.8) is an important piece of future work. There are also many other avenues open to investigation. Mixing indicators from the model could be examined to establish whether it is possible to predict reaction phenomena in the mill. The widespread application of the one-component model 2 may suggest empirical relationships between the rate-parameters a and b and milling parameters such as mill speed, mill size and the charge ratio. Similarly, the different rates observed when milling different powders could be connected with powder properties. Lastly, refinements of the kernel forms may be possible, for example, time-dependence may be introduced to account for work hardening and reaction effects.

Including work hardening effects will produce the most significant improvement in the model's accuracy at early times. Mechanisms are available that will generate work hardening behaviour in the model, but the work hardening process itself is not well understood. The introduction discussed how work hardening is caused by dislocations §1.1.3, but for extreme deformations the behaviour of the material is complex and difficult to describe in a model. Dislocations can be included in the model, either by counting them directly or using energy considerations. However both methods rely on an approximate

description of how dislocations multiply and move within the material.

For example, one mechanism for counting dislocations directly uses a cluster $C_{r,d}$ having size r containing d dislocations. Aggregation and fragmentation events conserve the number of dislocations in the material, so

$$C_{r,d} + C_{s,e} \rightleftharpoons C_{r+s,d+e}. \tag{8.1}$$

Although some dislocations may be gained or lost during welding and fragmentation, these effects are ignored in a first approximation. Aggregation and fragmentation rates depend on the size of the particles involved and the number of dislocations present. It is easy to calculate the dislocation density from these quantities, which will relate to the hardness of the material.

The model allows work hardening to occur by increasing the number of dislocations in the system using a non-reversible reaction,

$$C_{r,d} \xrightarrow{h_{r,d}} C_{r,d+1}, \tag{8.2}$$

where $h_{r,d}$ is the hardening rate. This rate depends on the size of the particle and the dislocation density, so differential effects can be accommodated like rapid hardening of small particles and a reduced hardening of the hardest particles. Unfortunately it is not clear exactly what form the hardening rate, $h_{r,d}$, and the dislocation dependent welding and fragmentation rates, $a_{r,d,s,e}$ and $b_{r,d,s,e}$, should take. Some features of these functions can be identified, for example the fragmentation rate, $b_{r,d,s,e}$, will increase with the number of dislocations in the fragmenting particle, $d + e$, because harder particles with more dislocations are more prone to fracture. Also, hardening will not continue indefinitely so the hardening rate, $h_{r,d}$, will tend to zero for a finite value of d.

It is hoped that work hardening theories can be simplified and incorporated in the model without adding too much complexity. While the introduction of a dislocation component increases the computational requirements when solving the model numerically it also opens the possibility for analysis using

similar techniques to those employed for the model with two different material components. Using a suitable approximation of work hardening would provide the greatest improvement to the existing models for short times where reaction phenomena are not significant.

Bibliography

[1] B. J. M. Aikin and T. H. Courtney. The kinetics of composite particle formation during mechanical alloying. *Met. Trans. A*, 24A:647–657, 1993.

[2] B. J. M. Aikin and T. H. Courtney. Modelling of particle size evolution during mechanical alloying. *Met. Trans. A*, 24A:2465–2471, 1993.

[3] B. J. M. Aikin, T. H. Courtney, and D. R. Maurice. Reaction rates during mechanical alloying. *Mat. Sci. and Eng.*, A147:229–237, 1991.

[4] A. S. Argon and G. East. A statistical theory for easy glide. *Trans. Jpn. Inst. Met.*, 9:756–767, 1967.

[5] L. G. Austin, R. R. Kimpel, and P. T. Luckie. *Process Engineering of Size Reduction: Ball Milling.* Society of Mining Engineers of the American Institire of Mining, Metallurgical and Petroleum Engineer, Inc. New York, 1984.

[6] A. Y. Badmos and H. K. D. H. Bhadeshia. The evolution of solutions: A thermodynamic analysis of mechanical alloying. *Metall. Mater. Trans. A*, 28A:2189–2194, 1997.

[7] J. S. Benjamin. Dispersion strengthened superalloys by mechanical alloying. *Met. Trans.*, 1:43–51, 1970.

[8] J. S. Benjamin. Mechanical alloying. *Sci. Am.*, 234(5):40–48, 1976.

[9] J. S. Benjamin and T. E. Voilin. The mechanism of mechanical alloying. *Met. Trans. A*, 5:1929–1934, 1974.

[10] R. W. Cahn, P. Haasen, and E. J. Kramer. Flow stress and work hardening. In *Materials Science and Technology*, volume 6, chapter 2. VCH Publishers Inc., New York (USA), 1993.

[11] F. Cardellini, G. Mazzone, A. Montone, and M. Vittori Antisari. Solid state reactions between Ni and Al powders induced by plastic deformation. *Acta Metall. Mater.*, 42(7):2445–2451, 1994.

[12] Á. Csanády, A. Csordás-Pintér, L. Varga, L. Tóth, and G. Vincze. Solid state reactions in Al–Ni composites made by mechanofusion. *J. Phys.*, 6:925–940, 1996.

[13] M. P. Dallimore and P. G. McCormick. Dynamics of planetary ball milling: a comparison of computer simulated processing parameters with CuO/Ni displacement reaction milling kinetics. *Mater. Trans., JIM*, 37(5):1091–1098, 1996.

[14] S. C. Davies. *Mathematical Modelling of Coagulation and Gelation.* PhD thesis, University of Nottingham, 1998.

[15] S. C. Davies, J. R. King, and J. A. D. Wattis. Self-similar behaviour in the coagulation equations. *J. Eng. Math.*, 32:57–88, 1999.

[16] S. C. Davies, J. R. King, and J. A. D. Wattis. The Smoluchowski coagulation equations with continuous injection. *J. Phys. A; Math. & Gen.*, 32:7745–7763, 1999.

[17] R. M. Davis, B. McDermott, and C. C. Koch. Mechanical alloying of brittle materials. *Met. Trans. A*, 19A:2867–2874, 1988.

[18] R. L. Drake. Kernels and initial spectra. In G. M. Hidy and J. R. Brock, editors, *Topics in current aerosol research*, chapter 4. Pergamon Press, New York, 1972.

[19] S. Dymek, M. Dollar, S. J. Hwang, and P. Nash. Deformation mechanisms and ductility of mechanical alloyed NiAl. *Mat. Sci. and Eng. A*, A152:160–165, 1992.

[20] M. J. Fleetwood. Mechanical alloying — the development of strong alloys *Overview. Mat. Sci. & Tech.*, 2:1176–1182, 1986.

[21] R. A. Flinn and P. K. Trojan. *Engineering Materials and their Applications.* Houghton Mifflin Company, fourth edition, 1990.

[22] E. Gaffet, M. Abdellaoui, and N. Malhouroux-Gaffet. Formation of nanostructural materials induced by mechanical processings (*Overview). Mater. Trans., JIM*, 36:198–209, 1995.

[23] C. Gente, M. Oegring, and R. Bormann. Formation of themodynamically unstable solid solutions in the Cu–Co system by mechanical alloying. *Phys. Rev. B*, 48(18):13244–13252, 1993.

[24] T. M. Godfrey, P. S. Goodwin, and C. M. Ward-Close. Production of titanium particulate metal matrix composite by mecahnical milling. *Mat. Sci. & Tech.*, 16:1–6, 2000.

[25] T. M. Godfrey, A. Wiseby, P. S. Goodwin, K. Bagnall, and C. M. Ward-Close. Microstructure and tensile properties of mechanically alloyed Ti–6Al–4V with boron additions. *Mat. Sci. and Eng. A*, A282:240–250, 2000.

[26] P. Grahle and E. Arzt. Microstructural development in dispersion strengthened NiAl produced by mechanical alloying and secondary recrystallization. *Acta Mater.*, 45(1):201–211, 1997.

[27] J. Guerrero-Paz and D. Jaramillo-Vigueras. Particle size evolution in Cu-15at%Al mechanically alloyed. *Nanostruct. Mater.*, 10(7):1209–1222, 1998.

[28] M. Gupta and E. J. Lavernia. Effect of preparation methods on the incorporation/distribution of ceramic particulates in metal based composite powders. *Mater. Trans., JIM*, 36(3):451–457, 1995.

[29] H. Hashimoto, G. G. Lee, and R. Watanabe. Simulation of ball motion for analysis of coating phenomema during tumbler-ball milling of Cu powder. *Mater. Trans., JIM*, 35(1):40–45, 1994.

[30] J. W. Hilgers, R. J. Spahn, and T. H. Courtney. Variation of the coagulation equation with applications in material sciences. *Math. Modelling*, 6:463–471, 1985.

[31] P. B. Hirsch. *Work Hardening*, chapter 5. Cambridge University Press, Cambridge, 1975.

[32] H. Huang, M. P. Dallimore, J. Pan, and P. G. McCormick. An investigation of the effect of powder on the impact characteristics between a ball and a plate using free falling experiments. *Mat. Sci. and Eng. A*, 241:38–47, 1998.

[33] G. Huard, R. Angers, M. R. Krishnadev, R. Tremblay, and D. Dubé. SiC_p/Mg composites made by low-energy mechanical processing. *Can. Metall. Q.*, 38(3):193–200, 1999.

[34] J. Z. Jiang. Mössbauer investigations of mechanical alloying in the fe–cu system. *Appl. Phys. Lett.*, 63(20):2768–2770, 1993.

[35] A. S. Keifets and I. J. Lin. Energetics approach to kinetics of batch ball milling. *Inter. J. Miner. Process.*, 54:81–97, 1998.

[36] P. O. Kettunen. Statistical theory as applied to cyclic hardening. *Acta Mater.*, 48:2231–2238, 2000.

[37] B. B. Khina and F. H. Froes. Modelling of mechanical alloying: Advance & challenges. *JOM — J. Min. Met. Mat. Soc.*, 48(7):36–38, 1996.

[38] U. F. Kocks. A statistical theory of flow stress and work-hardening. *Phil. Mag.*, 13:541–566, 1966.

[39] U. F. Kocks. Statistical treatment of penetrable obstacles. *Canadian Journal of Physics*, 45:736–755, 1967.

[40] U. F. Kocks, T. Hasegawa, and R. O. Scattergood. On the origin of cell walls and of lattice misorientations during deformation. *Scr. Metall.*, 14:449–454, 1980.

[41] K. L. Kuttler, J. W. Hilgers, and T. H. Courtney. The solution of an evolution equation describing certain types of mechanical and chemical interaction. *Appl. Anal.*, 19:75–88, 1985.

[42] J. Lagerbom and T. Tiainen. Effect of partial mechanical alloying on the self-propagating high-temperature synthesis of Ni_3Si. *J. Mater. Sci.*, 34:1477–1482, 1999.

[43] L. Lü and M. O. Lai. *Mechanical Alloying.* Kluwer Academic Press, Massachusetts, 1st edition, 1998.

[44] L. Lü, M. O. Lai, and S. H. Yap. Microstructure and mechanical properties of Al-4.5wt%Cu/15wt%SiC composite. *Mat. Sci. & Tech.*, 13:192–202, 1997.

[45] L. Lü, M. O. Lai, and S. Zhang. Modeling of the mechanical alloying process. *J. Mater. Process. Technol.*, 52:539–546, 1995.

[46] E. Ma and M. Atzmon. Phase transformations induced by mechanical alloying in binary systems. *Mater. Chem. Phys.*, 39:249–267, 1995.

[47] M. Magini and A Iasonna. Energy transfer in mechanical alloying *(Overview). Mater. Trans., JIM*, 36:123–133, 1995.

[48] D. R. Maurice and T. H. Courtney. Modeling of mechanical alloying: Part I. Deformation, coalescence, and fragmentation mechanisms. *Metall. Mater. Trans. A*, 25A:147–158, 1994.

[49] D. R. Maurice and T. H. Courtney. Modeling of mechanical alloying: Part II. Development of computational modeling programs. *Metall. Mater. Trans. A*, 26A:2431–2435, 1995.

[50] D. R. Maurice and T. H. Courtney. Modeling of mechanical alloying: Part III. Applications of computational programs. *Metall. Mater. Trans. A*, 26A:2437–2444, 1995.

[51] D. R. Maurice and T. H. Courtney. Process modelling of mechanical alloying *(Overview). Mater. Trans., JIM*, 36(2):110–122, 1995.

[52] D. R. Maurice and T. H. Courtney. Milling dynamics: Part II. Dynamics of a SPEX mill and a one-dimensional mill. *Metall. Mater. Trans. A*, 27A:1973–1979, 1996.

[53] D. R. Maurice and T. H. Courtney. Milling dynamics: Part III. Integration of local and global modeling of mechanical alloying devices. *Metall. Mater. Trans. A*, 27A:1981–1986, 1996.

[54] P. G. McCormick, H. Huang, M. P. Dallimore, J. Ding, and J. Pan. The dynamics of mechanical alloying. In *Proceedings of the 2nd International Conference on Structural Applications of Mechanical Alloying*, pages 45–50, Vancouver, British Columbia, Canada, 1993.

[55] M. M. Moshksar and S. M. Zebarjad. Morphology and size distribution of aluminium powder during milling processing, Transaction B. *Iranian Journal of Science & Technology*, 23(3):239–250, 1999.

[56] P. Nash, S-H. Wu, S-C. Ur, and M. Dollar. Design of dispersion strengthened NiAl. *Mater. Trans., JIM*, 36(2):351–356, 1995.

[57] Erik Nes. Modelling of work hardening and stress saturation in FCC metals. *Prog. Mater. Sci.*, 41:129–193, 1998.

[58] S. K. Pabi, D. Das, T. K. Mahapatra, and I. Manna. Mathematical modelling of the mechanical alloying kinetics. *Acta Mater.*, 46(10):3501–3510, 1998.

[59] V. A. Podoprigora, B. V. Dudka, S. N. Kolupaeva, and L. E. Popov. Modelling of small-sized particles subjected to strain in an attritor. *Ind. Lab. (Diagnostic of Materials)*, 63(6):358–362, 1997.

[60] K. B. Povarova, V. B. Proskurin, V. P. Levin, A. G. Nikolaev, N. K. Kazanskaya, and A. I. Firov. Effect of mechanical alloying on the mode of intermetallide phase formation in Ni–Al system on reactive sintereing. *Izv. Ross. Akad. Nauk, Met.*, No. 4:67–75, 1994.

[61] C. J. Rocha, E. G. de Araújo, R. A. Nogueira, and F. Ambrozio Filho. Effect of wax addition on monel synthesis by high energy milling. *Mater. Sci. Forum*, 299–300:457–462, 1999.

[62] R. W. Rydin, D. Maurice, and T. H. Courtney. Milling dynamics: Part I. Attritor dynamics: Results of a cinematographic study. *Met. Trans. A*, 24A:175–185, 1993.

[63] Hubert Saint-Raymond, Frédéric Gruy, and Michel Cournil. Turbulent aggregation of alumina in water and n-heptane. *J. Colloid Interf. Sci.*, 202:238–250, 1998.

[64] R. B. Schwarz. Microscopic model for mechanical alloying. *Mater. Sci. Forum*, 269–272:665–647, 1998.

[65] S. Suriñach. Calorimetric analyses of mechanically alloyed Ni_3Al based powders *(Overview). Mater. Trans., JIM*, 36(2):341–350, 1995.

[66] L. Takacs. Combustion phenomena induced by ball milling. *Mater. Sci. Forum*, 269–272:513–522, 1998.

[67] M. von Smoluchowski. Drei vorträge über diffusion brownshe molecular bewegung und koagolation von kolbidteilchen. *Physick Z*, 17:557–585, 1916.

[68] C. J. N. Wagner and M.S. Boldrich. The structure of amorphous and nano-crystalline metals and alloys. *Mat. Sci. and Eng. A*, A133:26–32, 1991.

[69] R. Watanabe, H. Hashimoto, and Gil Guen Lee. Computer simulation of milling ball motion in mechanical alloying *(Overview). Mater. Trans., JIM*, 36:102–109, 1995.

[70] T. Williams and C. Kelley. *GNUPLOT. An Interactive Plotting Program.* `http:\\www.gnuplot.org`, 1986.

[71] H. Zoz, D.Ernst, H. Weiss, M. Magini, C. Powell, C. Suryanarayana, and F. H. Froes. Mechanical alloying of Ti-24Al-11Nb (at%) using the Simoloyer. *Metall*, 50(9/96):575–579, 1996.

[72] H. Zoz, R. Reichardt, and H.Ren. Energy balance during mechanical alloyiong, measurement and calculation method supported by the MALTOZ software. *Private Communication*, 1999.